DC-RTS Noise: Observation and Analysis

by

Benjamin William Hendrickson

A dissertation submitted in partial fulfillment of the
requirement for the degree of

Doctor of Philosophy
in
Applied Physics

Dissertation Committee:
Erik Bodegom, Chair
Ralf Widenhorn
Raj Solanki
Dean Atkinson

Portland State University
2019

ABSTRACT

Dark current random telegraph signal (DC-RTS) is a physical phenomenon that effects the performance of solid state image sensors. Identified by meta-stable stochastic switching between two or more dark current levels, DC-RTS is an emerging concern for device scientists and manufacturers as a limiting noise source. Observed and studied in both charge coupled devices (CCDs) and complementary metal-oxide-semiconductor (CMOS) image sensors, the metastable defects inside the device structure that give rise to this switching phenomenon are known to be derived from radiation damage. An examination of the relationship between high energy photon damage and these RTS defects is presented and the results discussed. Evidence is presented which supports a second order generation mechanism for this particular class of RTS defect.

While troublesome to the image sensor community this kind of meta-stable switching, characteristic to RTS, is known to other scientific fields as an important dynamic that provides a description of those systems. Measurements of single molecule chemical reactions, for instance, produce the same general signal shape as those produced by RTS pixels. This commonality has motivated the development of a tool that can extract the key parameters of these signals, the amplitude and state lifetime. The amplitude is defined as the magnitude between two switching states while the state lifetimes are simply the mean time the system spends in the respective states. These parameters provide information on the features of these metastable systems.

It has been shown in previous RTS studies that a straightforward way to extract these parameters is to remove the Gaussian noise from the signals, leaving only the RTS transitions. This dissertation will present three methodologies that utilize noiseless reconstruction of signals for parameter extraction: convolutional filtering, wavelet denoising, and deep learning reconstruction. The capabilities of these techniques are examined quantitatively in a controlled experiment and qualitatively on data collected from a CCD image sensor, and the results compared against each other.

DEDICATION

For Mom and Dad who always encouraged me to wrestle with hard questions.

For Kirsten. This wouldn't have happened without you. Thanks for dreaming big

with me. On to the next!

ACKNOWLEDGMENTS

I would like to thank Dr. Bodegom for making a difficult thing hilarious.

I would like to thank Dr. Widenhorn for his not letting me get away with laziness.

I would like to thank Dr. Morley Blouke for inspiring me to love the work.

I would like to thank Dr. Richard Crilly of OHSU for helping me carry out all of the irradiation necessary for the study.

I would like to thank Denis Heidtmann and Paul DeStefano for their work building the instrumentation that made parts of this dissertation possible.

I would like to thank Dr. Nicholas Day for distracting me whenever I needed it. Thanks buddy. You kept my sanity in check.

TABLE OF CONTENTS

LIST OF TABLES

LIST OF FIGURES

Chapter 3 Figures

CHAPTER ONE - INTRODUCTION

1.1. Image Sensors: Basic Structure and Operation

Image sensors have a singular purpose: to convert photons to electrons in order to create a digital approximation of the image laid before them. While a variety of sensor designs have been tested and implemented, the vast majority employed for commercial and scientific use are silicon-based charge coupled devices (CCDs) and complementary metal oxide semiconductor (CMOS) sensors. These devices share a number of key similarities, such as: doped silicon to form PN-junctions, oxide layers to separate pixels readout circuitry, and amplifiers that convert the small voltage from sometime just a few electrons to a larger one that can be measured more easily. The following section provides a brief overview on the design and operation of both the CCD and CMOS image sensor, which will lay the groundwork of understanding how these pieces of silicon are able to create digital images.

1.1.1. CMOS Image Sensors

CMOS image sensors have undergone substantial changes in design and concept since their inception in the late 1960's. Early designs relied on processes that were simply too imprecise to reliably manufacture well-functioning imaging devices. The CCD, which was invented shortly thereafter, had much less noise than imagers built with the MOS device structure and was therefore quickly adopted as the preferred solid-state imager architecture. By the 1980's the CMOS process for device manufacturing became much improved, and was thought to be a means producing image sensors using a standard procedure, and avoiding costly one-off designs associated with CCDs. Ironically, modern

CMOS sensors are created with a litany of unique processes that completely negate their original promise of simplified manufacture, and yet are now the design of choice for commercial and many scientific applications. A much smaller power usage than CCDs along with flexibility in design for specific applications have pushed them to become the dominant image sensor architecture of the 21st century.
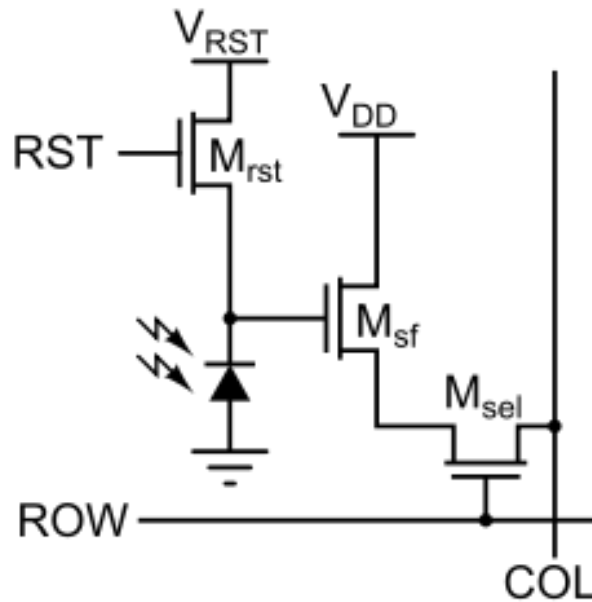
Figure 1: Equivalent circuit for a 3T CMOS Pixel

CMOS image sensors, as stated above, do not have a standard structure and may have a variety of different components to improve performance. The following description is strictly for a 3-transistor (3T) pixel structure, though sensors have been designed with as many as 10 transistors per pixel [1]. In the general 3T operation, as shown in figure 1, the reset transistor switch (RST) is closed, allowing a voltage V_{RST} to be applied across the photodiode. Note that the photodiode is held under reverse bias. Once RST is opened again

2

integration, or photon collection, begins. Integration is essentially a matter of collecting electrons that are produced either by the internal photoelectric effect, or by thermal electron promotion, both to be discussed in section 1.2. After integration the voltage across the photodiode is measured by means of the source follower amplifier (M_{sf}). That amplified signal is then read out through row/column circuitry and converted to a digital number further down the signal chain.
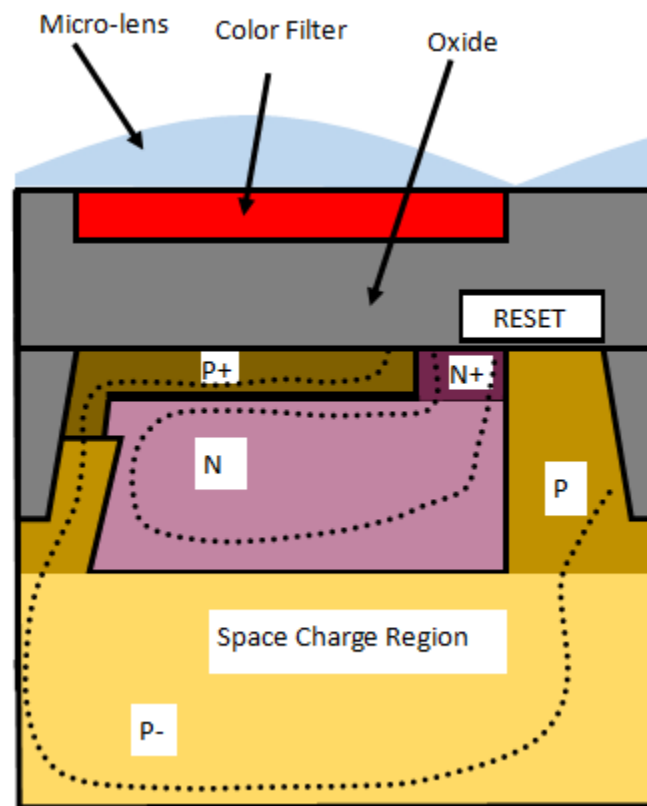
Figure 2: The structure of a typical basic CMOS pixel

In the simplest case, a CMOS pixel needs only a pn-junction to act as a photodiode, and readout circuitry to inform the computer how many electrons were created during integration. In practice, a few more elements and design considerations are necessary to

3

create quality images. First, the microlens grid, which sits atop the pixel array to concentrate light into the photosensitive area of the pixel. This prevents cross talk, a spatial noise source, and increases the quantum efficiency of a sensor, the measure of signal efficiency from the number of incident photons. The next optical layer is a color filter, which depending on the application may or may not be included. Following the color filter is the oxide layer which is used to insulate the transistors and readout circuitry. Finally, the photon collection region is made as a simple pn-junction, which when held in reverse bias creates a space charge region for collection of electrons. Note that doping concentration varies in different parts of the pixel. This is to 'pin' the photodiode, or keep the space charge region from touching the oxide. This is a common temporal noise mitigation technique since the semiconductor-oxide interface is amorphous in nature, and therefore prone to defects which generate leakage, or dark current (to be discussed in the next section).

1.1.2. CCD Image Sensors

CCDs, as stated above, were the first successful solid-state image sensor architecture. Invented at Bell Labs in 1969 [2], the CCD is still used today for some scientific applications because they can achieve a very high signal to noise ratio. This is possible because CCDs have fewer metal, or polysilicon traces than CMOS devices leading to higher fill factor and because of their ability to be completely pinned unlike CMOS sensors.
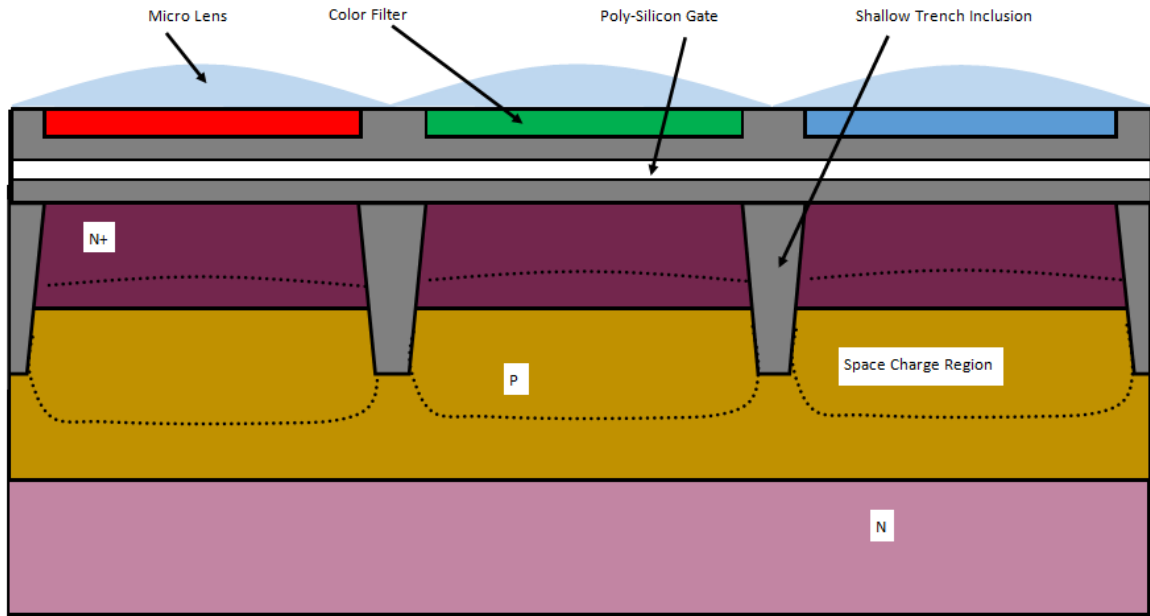
Figure 3: The structure of a typical CCD sensor

A simple CCD sensor will have many of the same components as a CMOS image sensor. They are, in principle, a grid of pn-junctions held in reverse bias to act as photodiodes. Just like CMOS sensors they will likely have microlenses, color filters, oxide layers for separating traces and pixels, and doping concentrations such that the photodiodes are 'pinned' from the oxides. The key difference between a CCD and a CMOS sensor is the lack of an in-pixel amplifier. In this structure the charge collected by each pixel is moved row by row, until it reaches a shift register that measures the charge one column at a time. The advantage of this sort of clocking is the single amplifier, which will have no variance in gain pixel-to-pixel. The main disadvantage is the time it takes to read out an array in this fashion, which is typically much longer than what is achievable with a global shutter CMOS sensor.
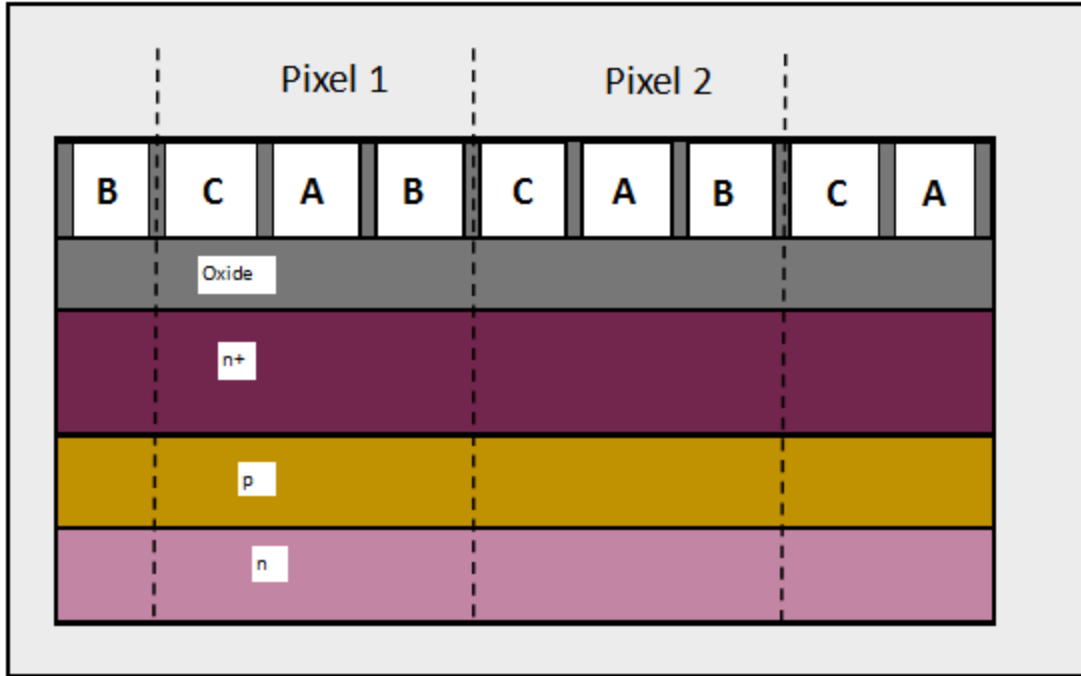
Figure 4: Charge transfer sequence

Figure 4 shows the means by which charge is moved row by row through the array. By clocking the voltages on the traces, the charges are pulled along via the coulomb force. A typical clocking scheme may run as: $(A \rightarrow AB \rightarrow B \rightarrow BC \rightarrow C \rightarrow CA \rightarrow A \dots)$, and so on.

1.2. Photocurrent and Dark Current

There are two central sources of electron generation inside a solid state pixel: photocurrent and dark current. Photocurrent is generated under normal operation via the internal photoelectric effect as a linear response to the number of photons that enter the photodiode region. Given that light is projected upon the face of the sensor, each pixel will have a unique number of photons fall onto it. Assuming that the number of electrons generated per photon is roughly the same, a digital approximation of that image can be

formed in a paint-by-numbers fashion where each pixel is a discrete cell. Photocurrent is responsible for producing the signal of a pixel.

Dark current, conversely, is a noise effect in image sensors. Rather than a designed response from the number of incident photons, dark current is a random process that stems from thermal promotion of electrons to the conduction band [3]. More of a device specific term than anything else, dark current is the same as a leakage current in any reverse biased diodes [4]. In each case a voltage is held across a pn-junction such that a space charge region exists. Given a device held at some temperature above zero, electrons will be promoted and collected until the potential well of the diode is filled, or saturated the same as if it were exposed to a bright light source.

1.2.1. Physics of Photocurrent

The photo-electrical properties of solids are governed by a quantity known as the band gap. Very simply, the band-gap is a measure of the amount of energy needed to promote an electron from their atomically bound valence band of states to the conduction band of states where they are free to move about a medium.

The most common material used to manufacture solid state image sensors is silicon. Not only is it plentiful on our planet, making it relatively inexpensive to mine and process, but it can be 'tuned' using neighboring elements on the periodic table to tweak electrical properties. Furthermore, in its pure crystalline form, silicon has an ideal band-gap for many optical applications: 1.12 electron volts (eV). As stated above image sensors work by using photons to promote electrons to a conduction state. In order to perform that function a photon must contain enough energy to push the electron across the energy band-gap. The

7

energetic range of optical photons, that is those we perceive with our eyes, is between $1.7eV$ and $3.2eV$. So, silicon with its $1.12eV$ band gap is suitable for electron promotion from optical photons, and even photons in the near infrared regime. This mechanism, promoting electrons to conduction by absorption of energetic photons, is the simplest process by which current is generated in semiconductor devices.

1.2.2. Physics of Dark Current

While photocurrent provides the signal for an image sensor, that is the information to be reproduced, other sources of electron promotion create unwanted variances in the values ultimately used for digital reconstruction. The main source of variance, or noise, is thermal promotion of electrons to the conduction band known as dark current. There are a variety of dark current sources including: defects from metallic impurities and interface amorphous structures, diffusion current, and field injection [5].

The likelihood of an electron occupying a specific energy state in a material is governed by the Fermi function, which is derived from Fermi-Dirac statistics. It is written as such:

$$f(E) = \frac{1}{\left(e^{\frac{E-E_F}{kT}}\right) + 1}$$

The Fermi function, very simply, states that the likelihood of finding an energy state (E) occupied by an electron in a material depends on the Fermi level (E_F), Boltzmann's constant (k), and the temperature (T). The Fermi level is the theoretical state in a medium that has a 50% likelihood of being occupied. For intrinsic or pure semiconductors at

8

$T = 0K$, this level lies exactly between the valence and conduction bands, which means for silicon the Fermi level is $0.56eV$ above the valence band. It should be noted that the Fermi level has a small temperature dependence, but can be ignored within the scope of this dissertation. The Fermi function appears as a perfect step shape for $T = 0K$, though the edges on the step soften as the temperature increases.
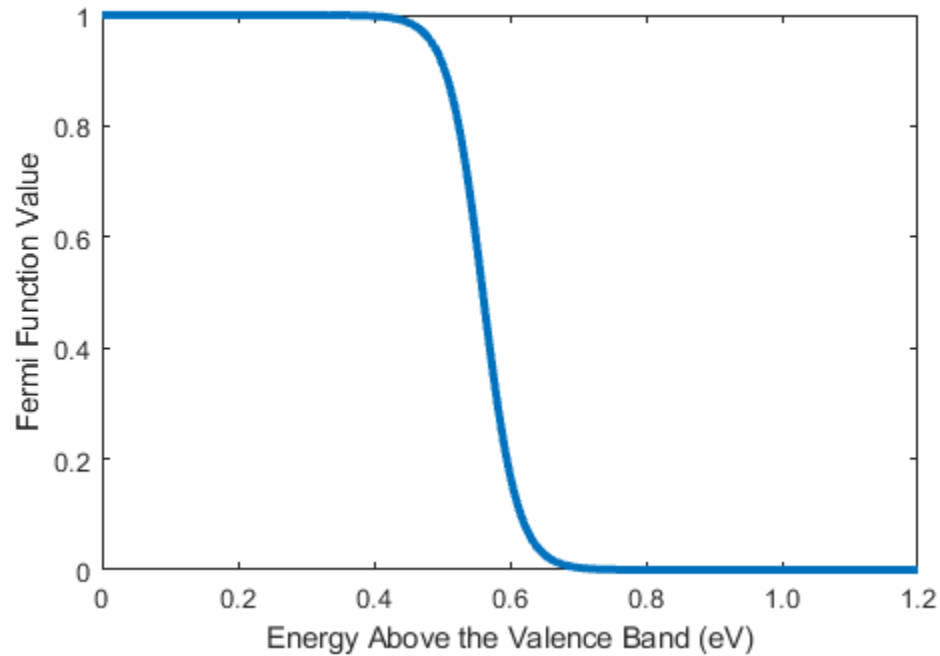
Figure 5: The Fermi function for intrinsic silicon at $295K$

As shown by figure 5, the probability of finding an occupied electron state above the $1.12eV$ intrinsic silicon band gap approaches zero. Simply put, at room temperature there is not enough thermal energy available to promote electrons to conduction in all but the rarest events.

So, given the rarity of thermal band-to-band transitions there must be another mechanism producing dark current. That mechanism is Shockley-Read-Hall (SRH) generation/recombination (G/R).

SHR-G/R describes how defects in a semiconductor lattice can create energetic traps inside the forbidden region of the band-gap. These trap-states act like stepping stones. If the energy level of the trap is near mid-gap, an electron may be thermally promoted to the trap state, then promoted again to the conduction band. The rate at which these trap states promote electrons is written as:

$$U = \frac{v_{th}\sigma N_t(np - n_i^2)}{n + p + 2n_i \cosh\left(\frac{E_t - E_i}{kT}\right)}$$

where U is the generation/recombination rate, v_{th} is the thermal velocity of the electrons, N_t is the trap state density, n is the electron concentration, p is the hole concentration, n_i is the intrinsic carrier density, E_t is the trap state energy, E_i is the intrinsic Fermi level, k is Boltzmann's constant, and T is the temperature.

It should be noted that the trap states themselves are inherently just as likely to promoted valence electrons to conduction states as they are to demote semi-free electrons back to valence states. However, because the normal mode of image sensor operation means the photodiodes are held in reverse bias a space charge region is formed, that is, $np \ll n_i^2$. Because of this inequality the trap states are limited to their generation role.

1.3. Bistability & Random Telegraph Signal

Modern scientific and commercial sensors are factory-made with very few defects from the process itself. Defects though, which create SRH G/R centers, can be formed after the manufacturing process itself by way of irradiation. A high energy photon or particle which is incident upon a sensor, can lead to a structural change in some part of a pixel. In general, the effect from this kind of damage is a simple increase in dark current. More rarely, a special kind of defect can form, one that seems to switch on and off. This kind of dynamic is called bistability, and in device physics is referred to as Random Telegraph Signal.

1.3.1. Bistability

Bistability is any process that is metastable in two states. Mostly observed in the quantum mechanical regime, this kind of dynamic is somewhat unintuitive. In short, balls never start rolling downhill then suddenly begin rolling up again. Typically these kinds of systems are modeled as a double-well like figure 6 below. Here there are two states, *A* and *B* separated by an energy barrier. The wells need not be symmetric, that is they may not be the same depth. The height of the barrier determines how often the states switch from one to another.
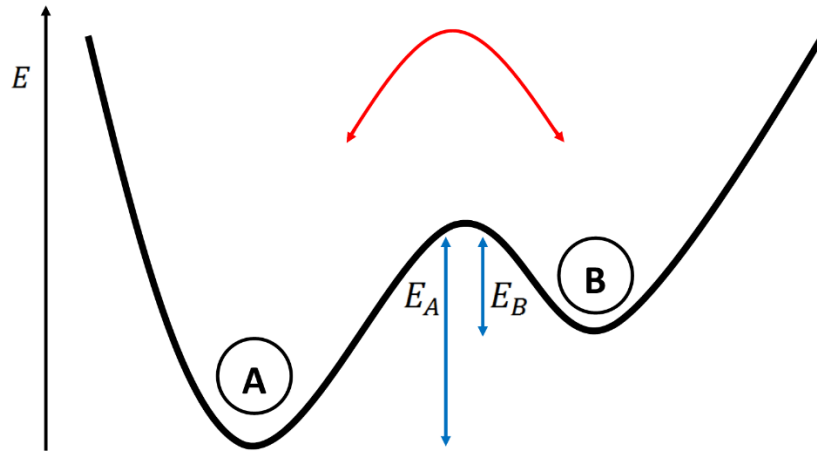
Figure 6: Energy well diagram of a bistable system

While this dissertation will focus mostly on bistable defect in image sensors, it should be noted that bistability has been observed in a myriad of physical systems. A list of bistable system examples is included and discussed below in chapter 3.

1.3.2. Random Telegraph Signal

Random Telegraph Signal (RTS) is a bistable phenomenon observed in semiconductor devices (though the term RTS has been used for bistable dynamics in other fields as well). The bistability manifests itself in time domain signals where the signal makes stochastic jumps between two states as shown in figure 7. The key parameters for an RTS signal are the state lifetimes (the average time spent on either the high or low state) and the amplitude (the difference in signal level between the two states). Note, for all examples of RTS signals in this dissertation the signal is presented in arbitrary units (AU) or digital numbers (DN), while the unit for time is presented in samples or frames.

RTS is an emerging concern for scientists and image sensor manufacturers. Many of the noise sources associated with image sensors (fixed pattern noise, read noise, kTC noise, dark current, etc…) have been mitigated to a satisfactory degree. This has left RTS noise as the limiting noise factor for many camera systems [6].
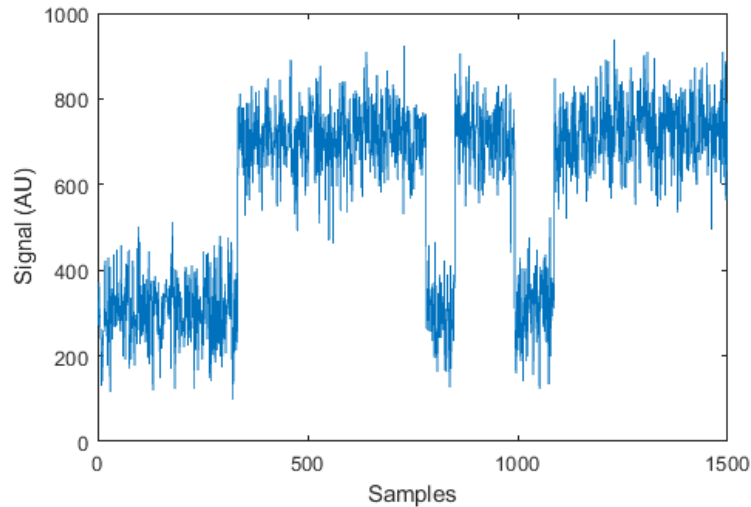
Figure 7: A typical RTS signal

Physically, RTS noise arises from a change in conductivity somewhere in the pixel circuitry. Conductivity is expressed as $\sigma = \mu n q$ where σ is conductivity, μ is mobility, n is the number of charge carriers and q is the fundamental charge. There are two kinds of RTS that have been observed and studied in image sensors, each originating from a different part of the pixel. Source follower RTS (SF-RTS) originates in the source follower amplifier found in all active pixel CMOS sensors. As electrons move under the gate of this transistor, they will occasionally become trapped in the oxide layer. When this occurs the gate-source voltage (V_{GS}) is lowered, which lowers the mobility (μ) across the gate and the conductivity (σ) along with it.

13

The second variety of RTS noise in image sensors is called dark current RTS (DC-RTS) noise. DC-RTS noise originates directly in the space charge region of the photodiode. The change in conductivity (σ) in this case occurs because of a change in the number of charge carriers (n). DC-RTS is caused by metastable SRH-G/R centers, though the physical mechanism that turns them 'on' and 'off' remains unsolved. It is possible that this variety stems from a class of defects, not a single geometry. DC-RTS has been shown to originate from defects in the bulk of the pn-junction caused by particle damage and defects on the Si/SiO_2 interface by energetic photons. It is differentiated from SF-RTS by its integration time (t_{int}) dependent amplitude which can be quite large. DC-RTS signals also tend to have much longer state lifetimes than SF-RTS signals. While SF-RTS state lifetimes tend to be on the order of milliseconds, DC-RTS lifetimes are unbounded; lifetimes of over 8 hours have been observed.

1.4. Signal Reconstruction

Bistable signals are inherently discontinuous and the transitions occur stochastically. As such, these kinds of signals provide a unique challenge in extracting its key parameters: state lifetimes and amplitude. Fourier analysis, for example, produces no characteristic frequencies. The most popular technique for analyzing these signals has come down to noiseless reconstruction.
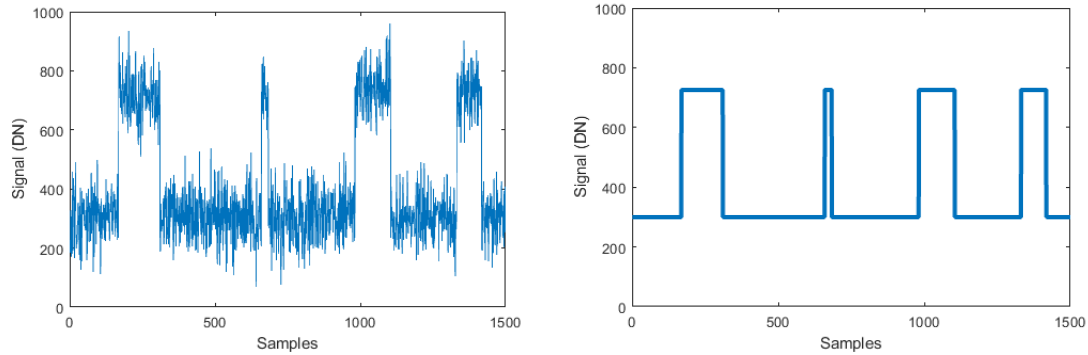
Figure 8: An RTS signal before and after reconstruction

The advantage of denoising or reconstructing signals is, of course, extracting the key parameters becomes a trivial task once the Gaussian noise is removed. The difficulty in designing an algorithm that can detect and reconstruct bistable signals is due to the unconstrained range of both key parameters. State lifetimes can be either very short, or very long. Likewise, amplitudes can be much larger than the Gaussian noise, or can be buried deep within it. The following three chapters all contain a description of some technique used for RTS signal analysis.

The experiment described in chapter 2 utilized a technique built on the wavelet transform. This transformation splits a signal into two daughter signals, one of which acts as a running average and the other which acts similar to a running derivative. Chapter 2 contains a detailed explanation of how the transform is used to 'denoise' an input signal. Furthermore, an experiment is outlined where image sensors were irradiated with high energy photons, and RTS parameters collected.

Chapter 3 shows how new deep learning techniques can be used to reconstruct non-linear signals, like those with RTS transitions. Therein, the basic building blocks of deep learning models are defined, and the architectures of two models are explained. It is shown that contrived or simulated data can be useful when training these kinds of models. The reconstruction algorithm is tested on both simulated and collected data.

Chapter 4 offers a comparison between the techniques laid out in the previous chapters as well as the most commonly used RTS analytical tool. That tool is built on convolutional filtering where a step-shaped filter is slid across a signal of interest. The result of the filtering suppresses Gaussian noise, while leaving spikes where RTS transitions occur. This makes it simple to create a noise free reconstruction of the signal. In chapter 4 it's shown that non-linear techniques may be best suited to reconstruct non-linear signals.

1.5. References

[2] Cheng-Hsiao Lai, Ya-Chin King and Shi-Yu Huang, "A 1.2-V 0.25-/spl mu/m clock output pixel architecture with wide dynamic range and self-offset cancellation," in *IEEE Sensors Journal*, vol. 6, no. 2, pp. 398-405, April 2006.

[2] *Charge transfer imaging devices,* US4085456A, 1971

[3] J. Carrère, S. Place, J. Oddou, D. Benoit and F. Roy, "CMOS image sensor: Process impact on dark current," 2014 IEEE International Reliability Physics Symposium, Waikoloa, HI, 2014, pp. 3C.1.1-3C.1.6.

[4] N. V. Loukianova *et al.*, "Leakage current modeling of test structures for characterization of dark current in CMOS image sensors," in *IEEE Transactions on Electron Devices*, vol. 50, no. 1, pp. 77-83, Jan. 2003.

[5] D. McGrath, S. Tobin, V. Goiffon, P. Magnan, and A Le Roch. "Dark Current Limiting Mechanisms in CMOS Image Sensors,"in *Image Sensors and Imaging Systems*, pp. 354-1-354-8.

[6] V. Goiffon, "Radiation Effects on CMOS Active Pixel Image Sensors," in Ionizing Radiation Effects in Electronics: From Memories to Imagers (M. Bagatin and S. Gerardin, eds.), CRC Press, 2015.

CHAPTER TWO – WAVELET ANALYSIS OF RTS NOISE IN CMOS IMAGE SENSORS IRRADIATED WITH HIGH ENERGY PHOTONS

Coauthored with Ralf Widenhorn, Morley Blouke, Denis Heidtmann, and Erik Bodegom

Abstract--This paper explores the phenomenon of dark current random telegraph signal (DC-RTS) noise in commercial off-the-shelf CMOS image sensors. Five sensors were irradiated with high energy photons to a variety of doses and analyzed with a wavelets-based signal reconstruction algorithm. The algorithm is explained in detail, and the radiation effects on individual pixels are discussed. Finally, the production rate of RTS pixels as a function of dose is explored, providing information on the underlying defect structure responsible for this noise source.

Keywords—CMOS image sensor, dark current random telegraph signal (DC-RTS), wavelet transform, denoising, gamma irradiation, 2nd order defect generation

2.1. Introduction

RANDOM Telegraph Signal (RTS) noise is characterized by discrete transitions in the signal current of a MOSFET device (see Figure 1). Studied since the 1960s [1], the steady shrinking of pixel pitch has driven RTS noise to become a major noise source in modern CMOS image sensors. These transitions occur due to alterations in the conductivity σ, which is expressed as $\sigma = \mu n q$ where μ is the mobility across the channel, n is the number of charge carriers, and q is the fundamental charge. RTS is known to have two primary causes, a change in μ brought on by the trapping/emission of a charge carrier in the gate oxide, and a change in n which arises from a metastable Shockley-Read-Hall (SRH) generation and recombination (G/R) center [2],[3]. The type of RTS that arises from a

change in μ is known as source follower RTS, while the type that arises from metastable G/R centers are known as dark current RTS.
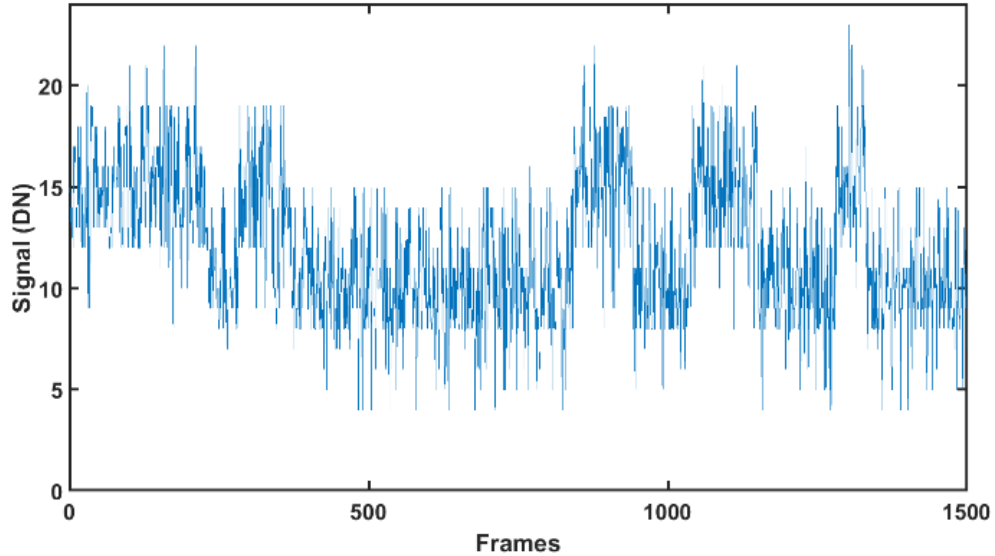
Figure 1: A prototypical bi-stable RTS-Noise Signal

With regards to a CMOS image sensor, the change in mobility can occur in the source follower transistor, which acts as an amplifier for the charge induced by exposure to photons or dark current. As such, this flavor of RTS is called source follower RTS, or SF-RTS. If a charge becomes trapped in the gate oxide, the gate-source voltage V_{gs} is lowered, which decreases the mobility across the channel. Once the trapped charge is emitted, V_{gs} returns to its normal operating value and the signal again reads true, exempting of course other noise sources.

The second type of RTS noise, dark current RTS (DC-RTS), is described by changes in the number of charge carriers. [4] .The physical mechanism behind this change in n is

19

still inconclusive, but is likely to occur from the turning on and off of SRH G/R centers in the depleted region of a photodiode or on the Si/SiO$_2$ interface touching the photodiode. Reported activation energies around the mid-gap level ($\sim 0.56eV$) supports metastable SRH G/R as the mechanism behind this second type of RTS [5],[6]. There is some variance in these measurements, so it is conceivable that a metastable bond rotation would change a trap state energy to be closer or further away from the center of the band gap, creating the conditions necessary to produce the observed signal. Or, perhaps a charge trap located on the boundary of the space charge region would move the depletion edge depending if it was in the capture or emission state. Regardless, this noise source is differentiated from SF-RTS by its very long state lifetimes [7], and the fact that the RTS amplitude is a function of integration time.

DC-RTS has been studied for over a decade [4]-[10], and the current state of the art technique for characterization was developed by V. Goiffon et. al. 2009 [10]. This method convolves a step shaped filter with signals of interest to detect RTS and extract both the various levels and state lifetimes. Here, we report a study of RTS and how the phenomenon depends on radiation from high energy photons including evidence for 2nd order defect generation. Rather than convolution, we explore if a method based on wavelet denoising, or shrinkage can be utilized. The method presented here is similar in computational runtime to the convolutional method. Wavelets are ubiquitous in image and signal processing [11]-[15] today, but have been little used in RTS studies. The following sections provide a brief outline of the mathematics behind wavelet denoising, and a detailed explanation of the wavelets denoising process that was used in this study.

2.2. Experimental Investigation of DC-RTS Noise

As stated previously, DC-RTS is a noise source characterized by a discrete change in the dark current of a pixel, identified by integration time dependence on RTS amplitude and time constants which are characteristically much longer than source follower RTS (SF-RTS). What remains elusive is the mechanism behind this noise source.

In order to study characteristics of DC-RTS amplitudes and time constants, five commercial-off-the-shelf Omnivision OV5647 CMOS five megapixel image sensors were irradiated at the Oregon Health & Science University (OHSU) Radiation Medicine department. These sensors were used, among others, in the iPhone 4 and in the Raspberry Pi Camera Module v1. We used the Raspberry Module. They have a 4T pixel structure, a $1.4\mu m$ pixel pitch, full well capacity of $4.3k$ electrons [16] and a 10-bit analog digital converter (ADC) giving an e^-/DN conversion of approximately 4.2 electrons per digital number. Linearity of the device was confirmed by Belloir et. al. [17], and our own group. The chips were dosed, with floating leads, with a distribution of bremsstrahlung radiation created by a linear electron accelerator with a tungsten target. Floating leads leave the device more susceptible to electrostatic potential variations. Dosimetry was carried out under the supervision of Dr. Richard Crilly of OHSU. The peak energy of the radiation spectrum was near $1.5\ MeV$ and the maximum energy was $6\ MeV$. Ionizing radiation is a well-documented underlying cause of RTS behavior that creates defects on the Si/SiO_2 interface, including the shallow trench isolation [18]. Frames for all imagers were taken in dark conditions with six second integration times and 20s between frames. Data collection occurred within the month following irradiation at a temperature of $23°C \pm 0.5°C$.

21

2.3. Haar Wavelet Analysis

2.3.1. The Discrete Wavelet Transform

Central to the following RTS noise characterization is the discrete wavelet transform. While there are a variety of suitable wavelets that can be used to perform the transform, here, we will utilize the Haar wavelet. To understand how the discrete wavelet transform works with the Haar wavelet consider a one dimensional vector $\mathbf{f}$ made of N sampled elements, $(f_1, f_2, f_3, \dots f_N)$ such that:

$$\mathbf{f} = (f_1, f_2, f_3, \dots f_N) \tag{1}$$

To perform the wavelet transform we take the raw signal $\mathbf{f}$ and use it to create two daughter vectors $\mathbf{a}$ and $\mathbf{d}$, each of which are half the length of signal $\mathbf{f}$ [19]. The $\mathbf{a}$ series is the trend or average series, and its coefficients are derived from the original signal as a running average such that:

$$a_m = \frac{f_{2m-1} + f_{2m}}{\sqrt{2}} \qquad\qquad 1 < m \leq N/2 \tag{2}$$

The $\mathbf{d}$ series is called the details vector and its coefficients track the changes in the original signal similar in function to a derivative:

$$d_m = \frac{f_{2m-1} - f_{2m}}{\sqrt{2}} \qquad\qquad 1 < m \leq N/2 \tag{3}$$

22

Since a transform is performed, it is necessary there be an inverse transform as well. For the Haar wavelet transform, the original signal can be recovered as follows:

$$\mathbf{f} = (\frac{a_1+d_1}{\sqrt{2}}, \frac{a_1-d_1}{\sqrt{2}}, \ldots \frac{\frac{a_N+d_N}{2}}{\sqrt{2}}, \frac{\frac{a_N-d_N}{2}}{\sqrt{2}}) \qquad (4)$$

It should be noted here that the $\sqrt{2}$ in the denominator of all coefficients is derived from conservation of energy throughout the transform.

A key feature of the wavelet transform is multi-resolution analysis (MRA). It is MRA that allows the wavelet transform to act like a microscope for digital signals, picking out key features at any scale of interest [20]. For example, if one is interested in features that occur on longer time scales it may be beneficial to perform the Haar wavelet transform several times, first to the original signal, then to its trend daughter signal, and so on. Each transform produces a trend and details series half the size of the signal from which they were derived, and therefore each coefficient in subsequent levels represents 2^k values from the raw signal, where k is the number of levels.

Now, with all the pieces laid out, we can construct a series of Haar details operators $\mathbf{W}$ and Haar trend operators $\mathbf{V}$ which are scalar multiplied with the original signal to create the sets of coefficients. For the first level (highest resolution) analysis:

$$\mathbf{W}_1^1 = \left(\frac{1}{\sqrt{2}}\right)(1, -1, 0, 0, 0, 0, \ldots)$$

23

$$\mathbf{W}_2^1 = \left(\frac{1}{\sqrt{2}}\right)(0,0,1,-1,0,0,\dots)$$

The first level details coefficients are then generated as follows:

$$d_1 = \frac{f_1 - f_2}{\sqrt{2}} = \mathbf{f} \cdot \mathbf{W}_1^1$$

$$d_m = \mathbf{f} \cdot \mathbf{W}_m^1$$

Note that the superscript on the operator represents the level of resolution. Therefore, the details operator to find the mth element of the kth level transform is represented as $\mathbf{W}_m^k$.

The trend operators are likewise constructed:

$$\mathbf{V}_1^1 = \left(\frac{1}{\sqrt{2}}\right)(1,1,0,0,0,0,\dots)$$

$$\mathbf{V}_2^1 = \left(\frac{1}{\sqrt{2}}\right)(0,0,1,1,0,0,\dots)$$

Similar to the details coefficients:

$$a_1 = \frac{f_1 + f_2}{\sqrt{2}} = \mathbf{f} \cdot \mathbf{V}_1^1$$

$$a_m = \mathbf{f} \cdot \mathbf{V}_m^1$$

2.3.2. Wavelet Denoising

The key step in the RTS analysis algorithm is denoising the original signal using the coefficients generated by the discrete wavelet transform (DWT). This method is particularly useful for detecting and characterizing RTS pixels because it suppresses white noise while leaving larger sudden changes untouched. One can think of it as a high-pass or low-pass filter that is dependent on change in magnitude rather than frequency.

As a first step the DWT is performed and the details vector coefficients are examined. If a particular coefficient falls below a specified threshold, it is set to zero. If a coefficient is larger than the threshold, it is either untouched (hard thresholding), or is subtracted by the threshold value (soft thresholding).

This threshold itself can be derived by a variety of techniques. The threshold chosen here is the VisuShrink, or Universal Threshold T defined as [21]:

$$T = \hat{\sigma}\sqrt{2\log(n)} \qquad (5)$$

where n is the number of elements in the discrete signal and $\hat{\sigma}$ is an estimate of the noise equal to the median of the absolute values in the details vector, $median\{\mathbf{d}\}$ divided by $u_{0.75} = 0.6745$, the 0.75 quantile of a normal distribution [22].

Though there are a variety of thresholds to choose from, the Universal Threshold is an ideal choice since it usually underfits the data [21], or in this case, minimizes the number of false RTS events.
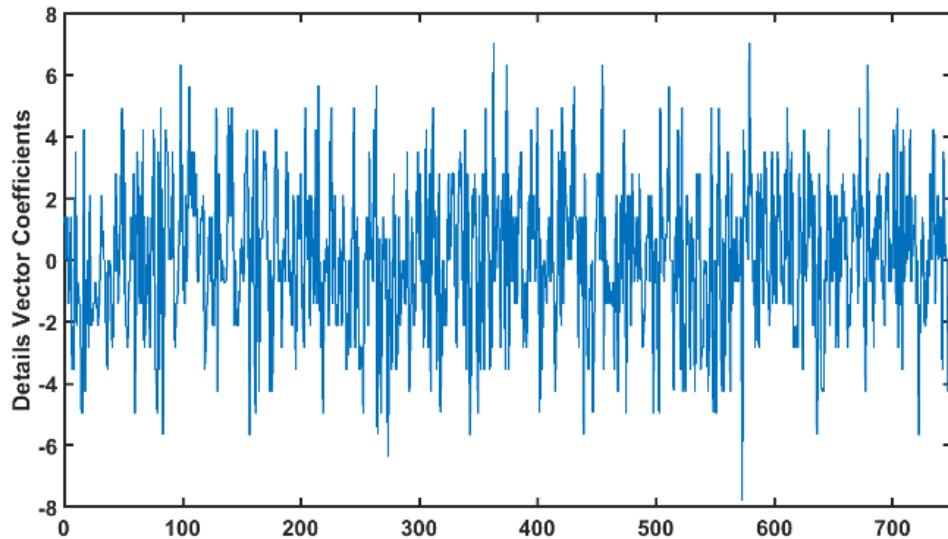
Figure 2: A typical details vector before thresholding. It contains half the number of elements as the signal undergoing the transform
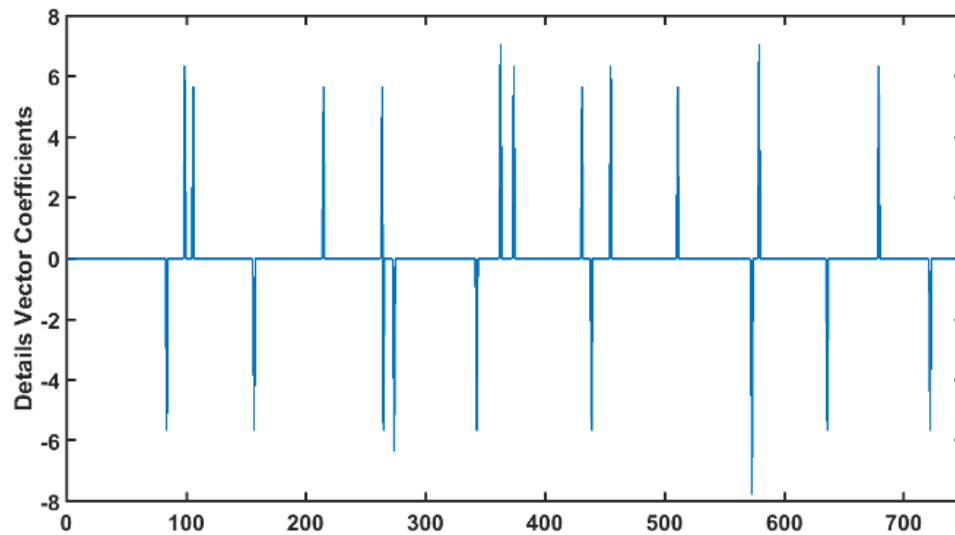
Figure 3: A typical details vector after hard thresholding

Recall that the details vector of the wavelet transform is generated by the changes in the original signal. As seen in figures 2 and 3, thresholding a details vector can greatly simplify, or reduce the noise power in the original signal, making the task of analyzing only the RTS noise far more manageable.

2.4. Signal Reconstruction

In order to analyze RTS amplitude and time constant distributions in radiation damaged sensors a noise free (RTS exempt) approximation signal is constructed based on the raw output from a particular pixel over several hours. The following process is designed to be highly discriminatory when validating a pixel for exhibiting RTS behavior. This is done to prevent false positive RTS detection from characteristics like high white noise, pink noise, or single events like cosmic ray impacts from polluting the statistics pool. The

reconstruction presented here is limited to two-level RTS since only a very small fraction (< 1% confirmed by visual inspection) of signals showed multi-level RTS, we felt unable to analyze them properly.

2.4.1. Window Comparison
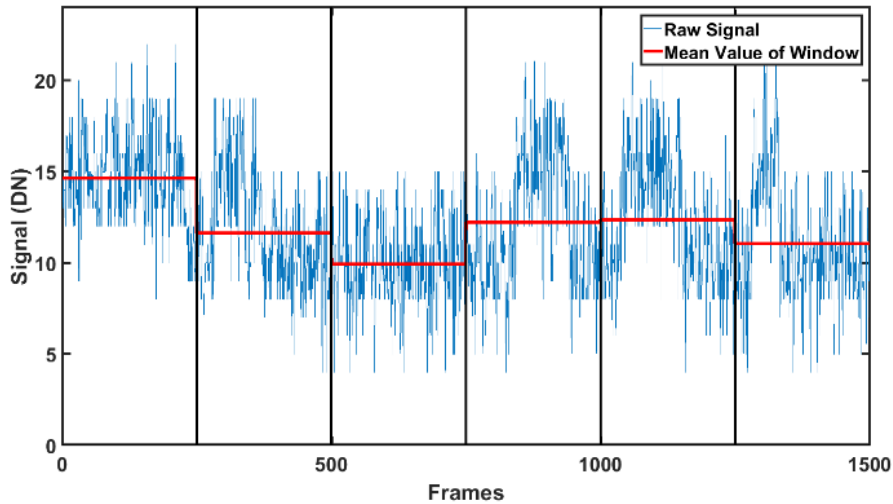
Figure 4: Stage 1, the raw signal **f** is split into windows of size 250 frames. The mean values of a window is compared to the mean of the previous two windows

The first step in the construction process is simply to break up the raw pixel signal into sections and compare the mean values of adjoined sections and their neighbor, seen in figure 4. This crude but effective RTS-Noise detector uses the standard deviation, σ_r of a signal as the metric for RTS candidacy. If the mean value of a particular section is greater or less than the mean value of the previous section by at least σ_r the pixel is passed along for analysis. We have chosen here to use six windows representing 250 frames after

28

discovering through trial and error that too small a window leads to an increase in false positive detections while too large a window leads to an increase in false negatives. This first simple step is important to the process not only because it does very well picking out RTS pixel candidates, but also because it saves precious run time by ensuring the computational heavy lifting is only performed on signals of interest. If a pixel fails the window comparison, the program simply moves on to the next.

2.4.2. DWT Denoising

A pixel that passes the window comparison test is then run through the DWT denoising process described above. The following analysis utilized a 7-level denoising routine after trial and error revealed that too few levels produces results with false positives, and too many would miss transitions..
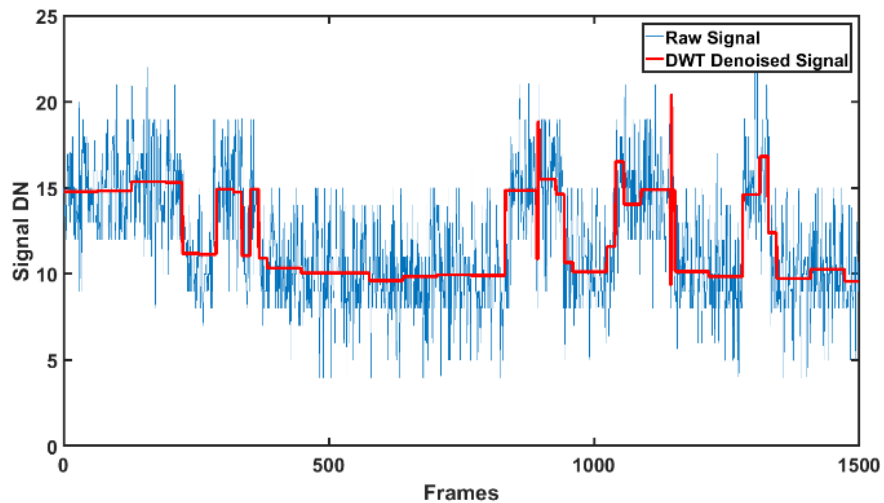
Figure 5: Stage 2, the signal f is run through the DWT denoising process, detailed above, and returned as the denoised signal **f′**. Though the white noise is severly depressed, transient spikes remain

29

2.4.3. Temporal Screen

The denoising process cleans the signal, however issues remain. First, the magnitude of the RTS transition amplitudes in the approximation often fall short of their true value, leaving a systematic error in our reporting. Second, very brief transitions appear in this denoised version, these are ringing artifacts. Since these features often fall outside of the Nyquist limit, they must be disregarded as transients in the characterization. In order to screen these brief transitions from the approximation signal temporal thresholding phase is employed in the program. This is accomplished by simple comparison and is possible because of the nature of the DWT denoising process. As seen in Figure 5, DWT denoising can leave long runs of sequential frames with exactly the same value. This means that in order to verify that a particular transition is not transient, all that is needed is to compare frame k with frame $k - 1$. If there is some difference in their values it is understood that a transition has taken place. Then, we compare the value of frame k with the value of the next l frames where l is the width of our temporal screen. If in fact the value of k is the same as the next l frames, the value is kept. If it fails this condition the value of frame k is set to the value of frame $k - 1$. The outcome of this process is seen in figure 6. The width of this screen can vary and can be subject to debate. On the one hand, the goal should be to construct a signal that is as closely correlated to the original as possible. On the other, many RTS signals display amplitudes that barely exceed the white noise, which can cast doubt on their very existence. In order to further increase the confidence of a transition we have chosen to set l equal to 10.
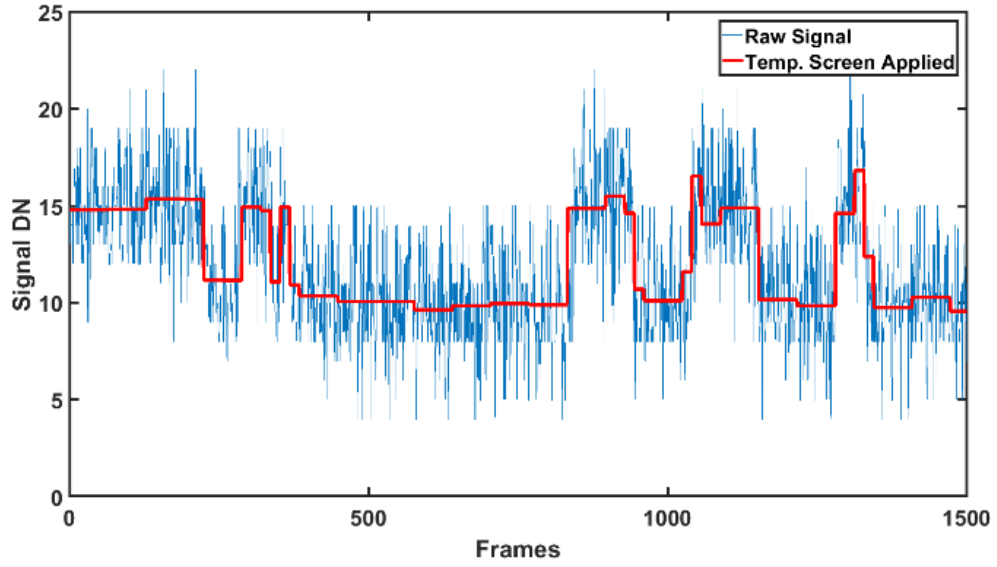
Figure 6: Stage 3, the denoised signal $\mathbf{f}'$ is passed through the temporal screen and returned as the denoised and screened signal $\mathbf{f}''$. Transient spikes have been removed

2.4.4. A Second Thresholding

At this point the signal shows almost no remnant of the white noise. With the transients removed and the majority of the heavy lifting taken care of by the DWT denoising, all that remains is to again threshold the changes in the screened signal. Recognizing that most of the changes, are zero, and only the largest changes are RTS transitions, shown in figure 7, the goal is to remove the smaller variations left over from the DWT denoising process. This time, rather than the dyadic DWT, we simply create a new series of size $N - 1$ by subtracting each value from the preceding one starting with element two. Here N is, again the number of elements in the signal and $\mathbf{f}'$ is the members of the new screened signal. $\mathbf{s}$ is used in place of $\mathbf{d}$ to emphasize the non-dyadic quality of this last details vector.

$$\mathbf{s} = (s_1, s_2, s_3, \dots s_{N-1}) \qquad (6)$$

$$s_m = f'_m - f'_{m-1} \qquad\qquad (7)$$
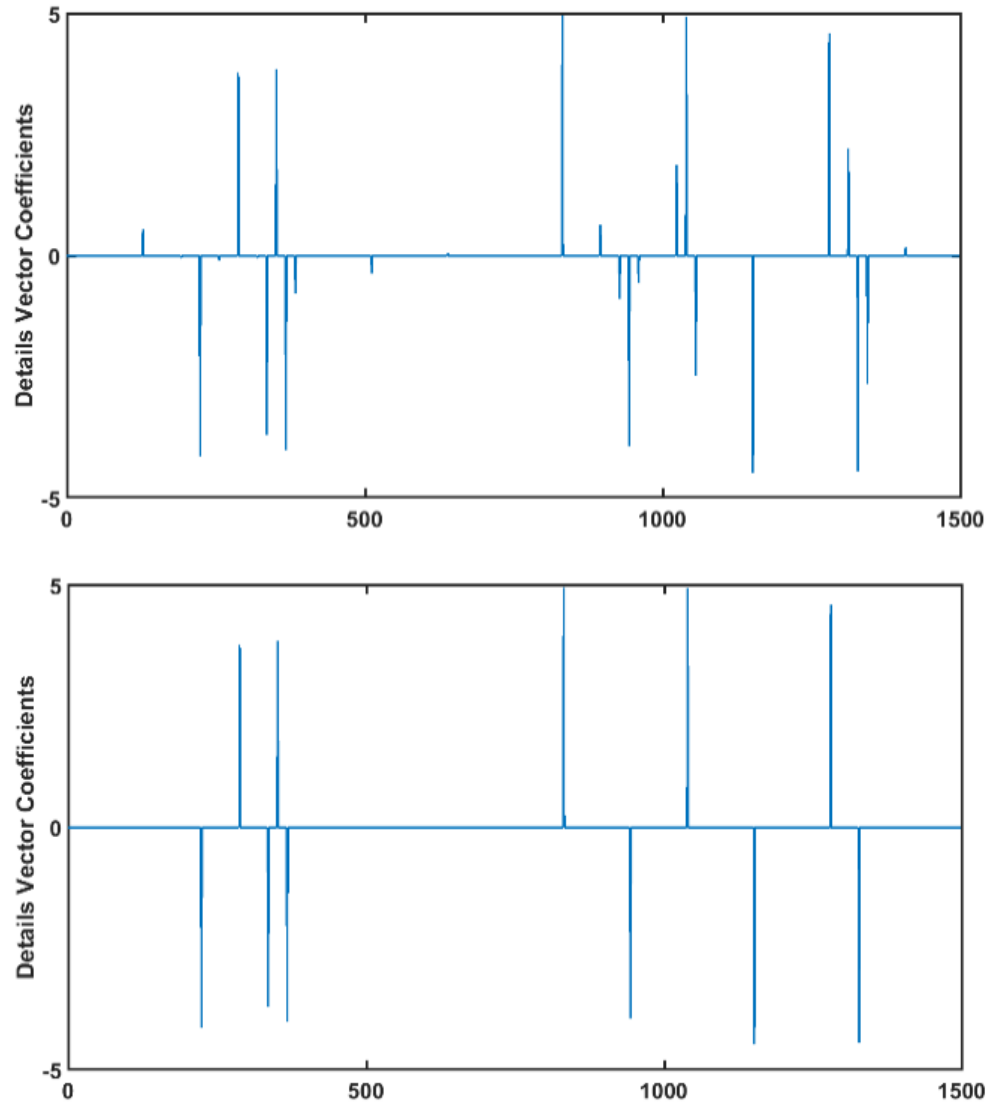
Figure 7: Stage 4, a typical details vector before and after denoising. All but a few of the

elements are set to zero

Again, the threshold is applied to this series just as before, but now the threshold is chosen differently. Since there are now so few large changes representing RTS transitions, and some smaller ones left over from the DWT process, we set the threshold $T_s = s_{MAX} * u_{0.75}$ [22]. All elements smaller than the threshold are again set to zero, while those larger are untouched.

2.4.5. Final Reconstruction
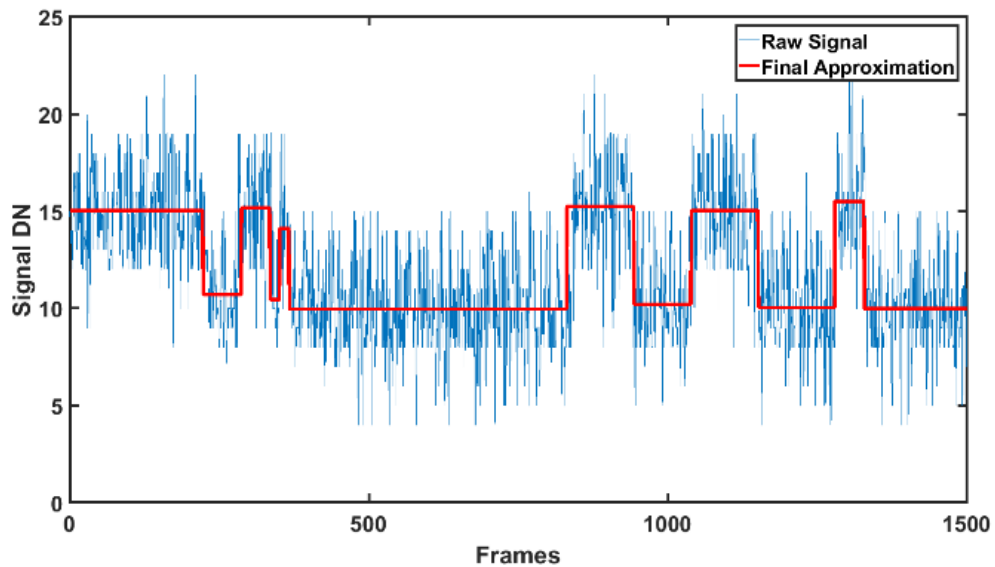
Figure 8: Stage 5, The final approximation is constructed. From here RTS transition amplitudes and time constants can be collected for statistical analysis

For the final reconstruction, the locations of the remaining non-zero elements are taken from the second threshold series, **s** and the mean values of the original signal between those locations are used to fill in the approximation shown in figure 8. By using the mean value

of the raw signal between transitions, it is ensured that the final amplitudes are very close to the actual values. From this form it is simple to collect time constants and transition amplitudes from tens of thousands of RTS pixels and study them from a statistical perspective.[1]

2.5. Results

The semilogarithmic plot of the distribution of maximum RTS transition amplitudes in Figure 9 reveals that, as expected, a larger dose leads to more RTS pixels. The amplitudes observed in this analysis can reach large magnitudes, up to $350e^-/s,$ though magnitudes of over $10000e^-/s$ have been reported [18]. It is notable that the slopes of the curves share a similar shape in all of the semi-log histogram curves, indicating that a higher dose increases the probability of creating a metastability, but the amplitude probability is set. The distributions are fit according to the decaying exponential equation $y = k \cdot \lambda \cdot \exp{(-\lambda \cdot x)}$. Here k is a constant related to the total number of RTS detections and λ is the inverse of the mean amplitude of the set.

---

[1] The quality of signal approximation was verified using a simulated data set.
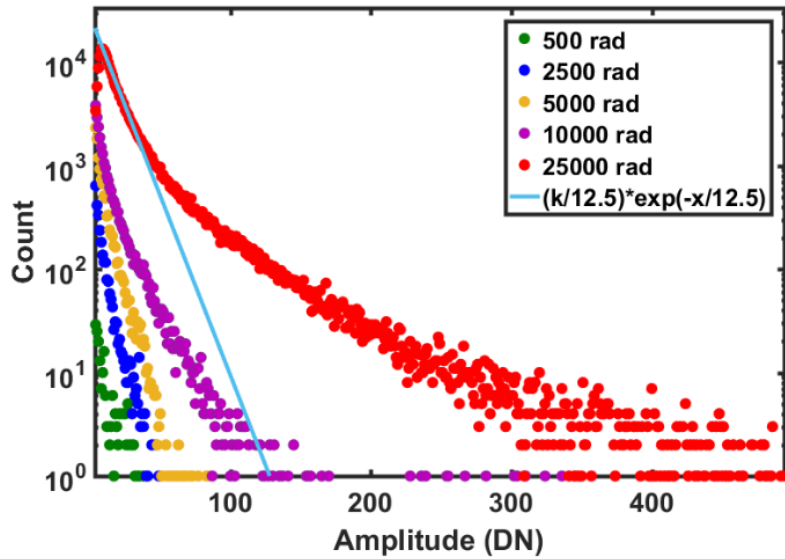
Figure 9: The distribution of RTS transition maximum amplitudes

Similar to the maximum amplitude plot, the state lifetime histograms of Figures 10 & 11 display an exponential distribution, though far more flat, here with a peak at approximately 250 frames, or around 85 minutes. It is likely that the shortest transition times are artificially suppressed by choosing to denoise the signals down several levels. A signal that is denoised four levels would yield a high-resolution analysis at the cost of approximation accuracy from false positives. A curiosity from the plots is the apparent flattening of the distribution peak seen in the 'low state' time constants, i.e., the lower of the two level dark current signal levels. This may indicate that the physical configurations that produce the 'low state' for DC-RTS pixels are, on average, more stable than the 'high state' configuration.
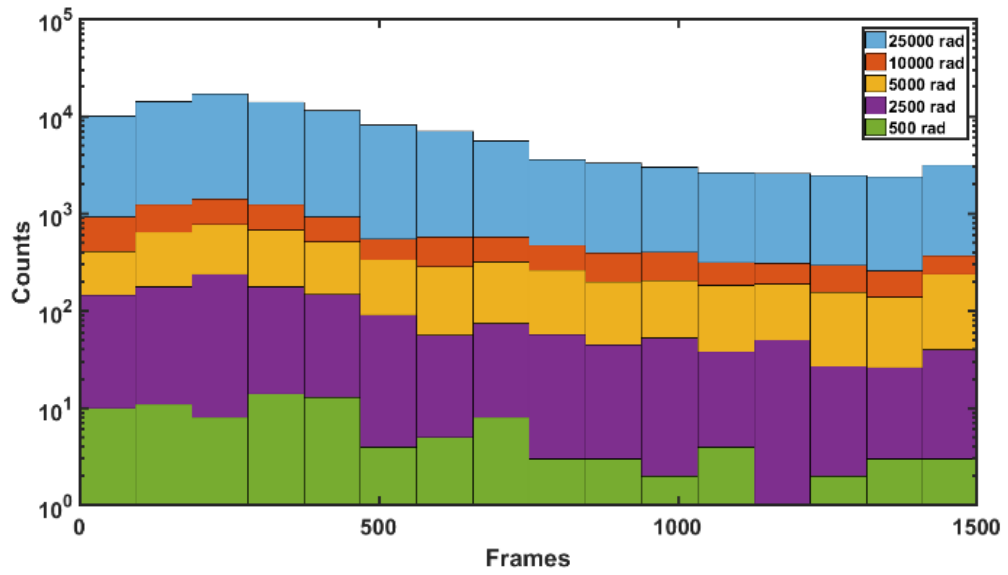
Figure 10: The distribution of 'high' state time constants
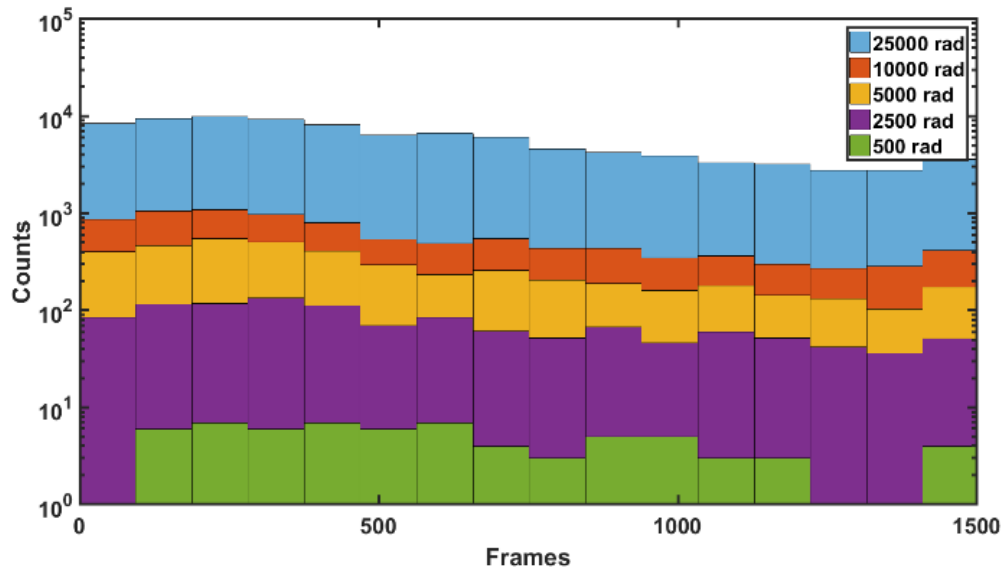
Figure 11: The distribution of 'low' state time constants
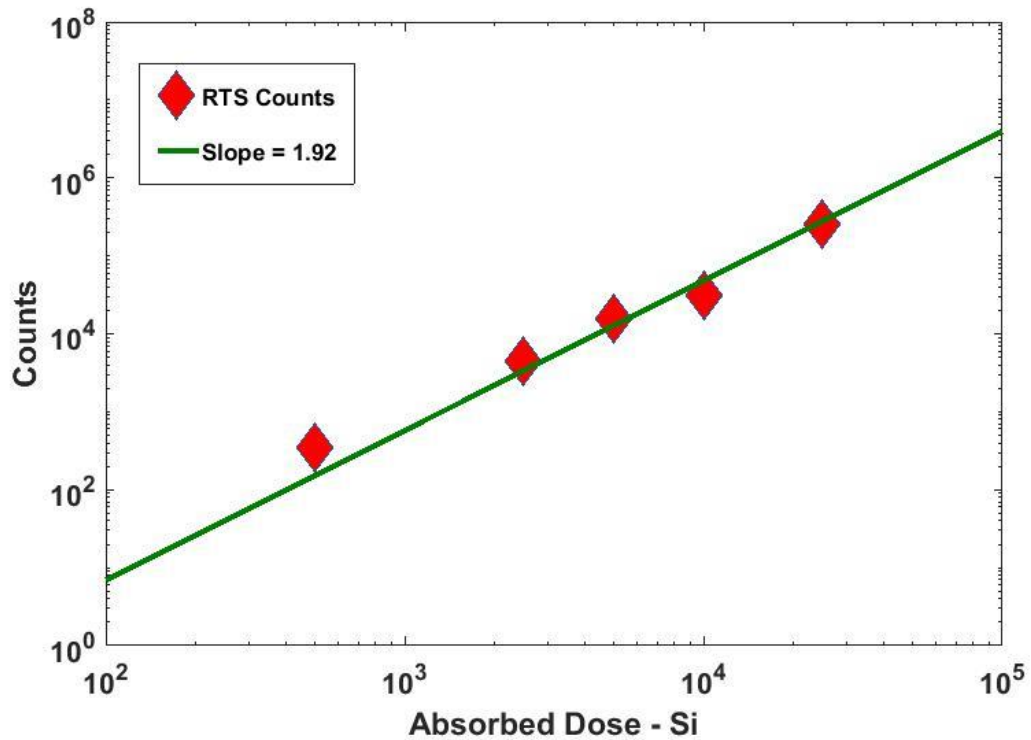
Figure 12: The number of RTS pixels as a function of absorbed radiation dose (Rad(Si))

As seen in figure 12, the number of RTS pixels does not follow a linear correlation with radiation dose, but rather increases almost quadratic with the dose. This result indicates that the process creating RTS centers by γ-radiation is of second-order. There is some precedence for this type of defect generation mechanism. It has been reported that very high doses of γ-radiation is responsible for the formation of defect centers known as H (97K) and $I^{0/-}$ (200 K), designated as such by their peaks on a thermally stimulated current (TSC) spectrum [23]. The I center band energy has been measured at $0.5eV \pm 0.05eV$ below the conduction band, very close to the RTS defect energies reported in [4],[5]. There is some discussion as to whether or not H is simply the donor state of I,

making them the same defect. Regardless, both states grow in population at a nearly quadratic rate with dose and share nearly the same slope on a log-log plot, as the data reported in Figure 12 [23]. While far from conclusive in identifying the defect responsible for DC-RTS on the interface of pixels, 2nd order generation narrows down the field of candidates and provides a potential path toward that identification.

2.6. Conclusion

We report the results of a study into DC-RTS noise in commercial image sensors irradiated with high energy photons. The study utilized a wavelet denoising method that suppresses Gaussian noise while preserving RTS level transitions. That method was explained in detail. We found that while increased dose increases the chances of creating an RTS center, the amplitude probability distribution is independent of dose. Finally, we report that the number of RTS pixels does not increase linearly with dose, but instead the dependence is nearly quadratic. This indicates that the defect responsible for DC-RTS from high energy photons arises from a second order generation mechanism, which provides guidance for further studies in this area.

2.7 References

[1] P. L. Leonard and S. V. Jaskolski, "An investigation into the origin and nature of "Popcorn noise"," in *Proceedings of the IEEE*, vol. 57, no. 10, pp. 1786-1788, Oct. 1969.

[2] W. Shockley and W. T. Read, "Statistics of the Recombination of Holes and Electrons," *Phys. Rev.* vol. 87, no. 835, Sep. 1952

[3] R. N. Hall, "Electron-Hole Recombination in Germanium," *Phys. Rev.* vol. 87, no. 387, Jul. 1952

[4] V. Goiffon, P. Magnan, P. Martin-Gonthier, C. Virmontois, and M. Gaillardin, "New source of random telegraph signal in CMOS image sensors," presented at the International Image Sensor Workshop, Hokkaido, Japan, 2011.

[5] C. Virmontois *et al.*, "Total Ionizing Dose Versus Displacement Damage Dose Induced Dark Current Random Telegraph Signals in CMOS Image Sensors," in *IEEE Trans. on Nucl. Sci.*, vol. 58, no. 6, pp. 3085-3094, Dec. 2011.

[6] J. Bogaerts, B. Dierickx and R. Mertens, "Random telegraph signals in a radiation-hardened CMOS active pixel sensor," in *IEEE Trans. on Nucl. Sci.*, vol. 49, no. 1, pp. 249-257, Feb. 2002.

[6] G. R. Hopkinson, "Cobalt60 and proton radiation effects on large format, 2-D, CCD arrays for an earth imaging application," *IEEE Trans. Nucl. Sci.*, vol. 39, pp. 2018–2025, Dec. 1992.

[7] I. H. Hopkins and G. R. Hopkinson, "Random Telegraph Signals from Proton-Irradiated CCDs," *IEEE Trans. Nucl. Sci.*, vol. 40, pp. 1567–1574, Dec. 1993.

[7] I. H. Hopkins and G. R. Hopkinson, "Further Measurements of Random Telegraph Signals in Proton-Irradiated CCDs," *IEEE Trans. Nucl. Sci.*, vol. 42, pp. 2074–2081, Dec. 1995.

[10] V. Goiffon, G. R. Hopkinson, P. Magnan, F. Bernard, G. Rolland, and O. Saint-Pe, "Multilevel RTS in Proton Irradiated CMOS Image Sensors Manufactured in a Deep Submicron Technology," *IEEE Trans. Nucl. Sci.*, vol. 56, pp. 2132–2141, Aug. 2009.

[11] G. Chen, W. Xie and Y. Zhao, "Wavelet-based denoising: A brief review," *2013 Fourth International Conference on Intelligent Control and Information Processing (ICICIP)*, Beijing, 2013, pp. 570-574.

[12] Ç. P. Dautov and M. S. Özerdem, "Wavelet transform and signal denoising using Wavelet method," *2018 26th Signal Processing and Communications Applications Conference (SIU)*, Izmir, 2018, pp. 1-4.

[13] P. S. Addison, J. Walker and R. C. Guido, "Time--frequency analysis of biosignals," in *IEEE Engineering in Medicine and Biology Magazine*, vol. 28, no. 5, pp. 14-29, September-October 2009.

[14] Yu-Feng Li, "Image denoising based on undecimated discrete wavelet transform," *2007 International Conference on Wavelet Analysis and Pattern Recognition*, Beijing, 2007, pp. 527-531.

[15] A. Ouahabi, "A review of wavelet denoising in medical imaging," *2013 8th International Workshop on Systems, Signal Processing and their Applications (WoSSPA)*, Algiers, 2013, pp. 19-26.

[16] *OV5647 5-megapixel product brief,* Omnivision, Santa Clara, CA, Nov. 2010.

[17] J. M. Belloir, V. Goiffon, C. Virmontois, P. Paillet, M. Raine, P. Magnan, and O. Gilard, "Dark Current Spectroscopy on Alpha Irradiated Pinned Photodiode CMOS Image Sensors," *IEEE Trans. Nucl. Sci.*, vol. 63, pp. 2183– 2192, Aug. 2016.

[18] E. Martin, T. Nuns, C. Virmontois, J.-P. David, and O. Gilard, "Proton and g -Rays Irradiation-Induced Dark Current Random Telegraph Signal in a 0.18-mm CMOS Image Sensor," *IEEE Trans. Nucl. Sci.*, vol. 60, pp. 2503–2510, Aug. 2013.

[19] J. S. Walker, *A Primer on Wavelets and their Scientific Applications*. 2nd ed. Boca Raton [Fla.]: Chapman & Hall/CRC, 2008.

[20] M. Gilli, *Computational Economic Systems: Models, Methods & Econometrics.* Springer Science & Business Media, Mar. 2013.

[21] G.P. Nason "Choice of the Threshold Parameter in Wavelet Function Estimation." In: Antoniadis A., Oppenheim G. (eds) *Wavelets and Statistics. Lecture Notes in Statistics,* vol 103. Springer, New York, NY, 1995

[22] J. Groß*, Linear Regression*. Springer-Verlag Berlin Heidelberg, July 2003.

[23] I. Pintilie, E. Fretwurst, G. Lindström, J. Stahl, "Second-order generation of point defects in gamma-irradiated float-zone silicon, an explanation for 'type inversion'," *Applied Physics Letters*, vol. 82, pp. 2169-2171, Mar. 2003.

CHAPTER THREE – DETECTION AND RECONSTRUCTION OF NOISY BISTABLE
STOCHASTIC TIME DOMAIN SIGNALS USING MACHINE LEARNING

Coauthored with Ralf Widenhorn, Paul R. DeStefano and Erik Bodegom

Abstract– Bistable stochastic systems are characterized by random discrete jumps in
what otherwise would be a constant signal, usually measured as current or voltage. Here, a
method of bistable stochastic signal detection and white-noise-free reconstruction is
presented. This method is built on machine learning techniques for classification and
denoising of one-dimensional time-series. The model is trained on a simulated dataset in
order to provide certainty in the fidelity of corresponding 'clean' and 'noisy' signals, and
tested on a different set of simulated signals. In addition, experimental data collected from
a digital image sensor are used to provide a qualitative description of the model's efficacy.

*Keywords—*machine learning, bistable stochastic signals, random telegraph signal,
convolutional neural network, denoising autoencoder, signal reconstruction

3.1. Introduction

3.1.1. Bistable Stochastic Signals

Bistable stochastic signals or stochastic switching signals are the result of nonlinear
dynamic processes that occur across many domains of physical science. This category of
phenomena is frequently modeled as a double potential well with an energy barrier of some
height in the center. The system remains in one of the states for some time until an event,
or random energetic fluctuations, prompts the system over the barrier to the other state.
The system returns to the previous state in the same way.

This phenomenon has been observed and studied extensively in biomolecular dynamics [1-5] where the kinetics of single molecule chemical reactions [6], and the mechanics of ion transport in biological membranes are modeled as two-state systems [7-9]. Single molecule reaction observations provide more precise measurements than those taken from a large collection. Ion transport is an important basic cellular process that provides insight into disease mechanisms. Enabling easier extraction of key parameters from these signals may enable researchers to develop more cost effective techniques to advance their fields. Many quantum mechanical systems are defined and analyzed as two-state stochastic dynamic processes including studies into electron shelving [10], strongly coupled atom/resonator systems [11], and detection of spin resonance for a single electron [12]. These studies shed light into the dynamics between quantum mechanical systems and interacting fields, and allow nondestructive measurement of quantum spin states. Semiconductor devices are susceptible to metastable defects often caused by radiation exposure. Since these defects stochastically switch on and off, they produce bistable current signals known as random telegraph signals [13-17]. Analyzing the amplitudes and state lifetimes of these signals provides insight into the class and locations of these defects.

Bistability is common, but has important implications. It has been shown that the superposition of bistable sources produces $1/f$ noise, a phenomenon that has been observed in everything from electronic devices to quasars [18]. The amplitudes and state lifetimes have different meanings for each system, but each provides information on a fundamental process in nature. In this paper we will describe a generic method for

characterizing bistable signals and we will apply the technique to a large data set from a digital image sensor.

3.1.2. Basic Mathematics of Noisy Bistable Stochastic Signals

Bistability is defined by stochastic transitions between one of two states, defined here as state 0 and state 1, the low and high states respectively. Represented mathematically, the state s at some given time t is either $s(t) = 0$ or $s(t) = 1$. Here, we will assume that any bistable signal has two independent noise contributors, the state transitions and Gaussian or white noise from other sources e.g., measurement. Since these noises are assumed independent from one another in our model, their respective variances add together to determine the total noise of the signal such that:

$$\sigma_{SIG}^2 = \sigma_{Gaussian}^2 + \sigma_{BST}^2$$

The magnitude of the signal at some time t is written as:

$$x(t) = x_0 + \epsilon(t) + A * s(t)$$

where x_0 is the signal value of the bottom state, $\epsilon(t)$ is the dark current Gaussian noise contribution at time t, $s(t)$ is the system state at time t, and A is the state separation, or

bistable amplitude. While the characteristic state lifetimes of a bistable signal may depend on a variety of factors, they are typically modeled as decaying exponentials, with the likelihood of the system flipping from one state to the other increasing with time. The model presented here is built on that assumption in order to account for the stochastic nature of these signals.

3.1.3. Machine Learning Classification

The goal in building a classification model is to take a set of data made of many categories and accurately separate it into its different types. This classification model was trained to differentiate noisy bistable signals from non-bistable signals. A signal is represented as a vector and passed through various layers of operators or functions to produce, in this case, a single output (zero for bistable signals or one for non-bistable signals). This is similar to the way that image classification is performed, and similar to machine learning classification methods previously used for one-dimensional digital signals [19-23]. A typical convolutional classification model [24] will include: convolutional, pooling, dropout, and fully connected layers, here, each is addressed in turn.

3.1.3.1. Convolutional Layers

Convolutional layers apply filters to extract prominent features that are representative of distinctive characteristics, such as state transitions. As the signal is passed forward through the network, each neuron (or, filter or kernel) is convolved with the signal creating a feature map that is the same size as the input [25]. Finally, an activation function is applied to each filter. This function ensures that each convolution is, in the end, a non-

46

linear operation. The activation function used here is the rectified linear unit (ReLU) function [26] which returns a zero for negative inputs and the input value itself for positive inputs [27], or with x the input:

$$f(x)_{ReLU} = \max\{0, x\}$$

Convolutional layers that are stacked after the initial layer will operate upon the feature maps produced from the previous layers. The shapes of the filters, or weights of the neurons, are continuously changed during the training process by backpropagation, to be discussed later.

3.1.3.2. Pooling Layers

Pooling layers reduce the dimensionality of the vector by down-sampling the feature maps. Pooling layers typically appear directly following a convolutional layer. While there are a variety of pooling techniques, our classification scheme uses "max-pooling." Essentially, max-pooling is a form of compression that inspects a section of a feature map, say elements 7, 8, and 9, finds the largest value amongst the three, and tosses the other two values out. Pooling not only eases the computational stress of training a model by reducing the number of parameters, but also provides spatial invariance of important features [28].

3.1.3.3. Dropout Layers

Dropout layers turn off a percentage of neurons, or filters during training. This prevents filters from becoming dependent on the presence of neighboring filters to optimize the

model. This interdependence leads to overfitting. An overfit model will perform very well on the data it is trained on, but will perform poorly on data in general [29].

3.1.3.4. Fully Connected Layers

The final layer in a classification model is a fully connected layer. Each neuron in this layer, as the name suggests, is connected to every output from the previous layer. This layer forms a vector where each element represents a confidence score corresponding to a distinct class. This model has a final layer of size one, where the one neuron represents the confidence of a signal containing bistability.

3.1.4.   Classifier Training

When the model is first initialized for training the coefficients of each filter, or the shape of each filter, are randomized. Then, one by one, members of the training set are passed through the network, and assigned a confidence of bistable versus non-bistable. Because this is supervised training the confidence score is checked against the given label for the signal, 0 for bistable and 1 for non-bistable signals. The error of the confidence score is calculated by using the binary cross-entropy loss function, defined below, and improved by updating the filter and activation weights by means of backpropagation [30].

3.1.4.1. Binary Cross Entropy

The loss function used for classification is binary cross entropy, E. Here, t is the target label, 0 for bistable, 1 for non-bistable. y is the probability of the signal being non-bistable according to the model. Notice that if the target and probability are close to one another the error is close to zero [31].

$$E = -(t \log(y) + (1 - t)\log(1 - \text{y}))$$

3.1.5. Denoising Autoencoder

Once the signal is run through the classification model, and if it is determined to have bistability, the signal has its white noise component suppressed by means of a denoising autoencoder (DAE). The autoencoder shares some features of the classifier, e.g., convolutional layers, pooling layers, etc. Rather than attempting to identify the kind of signal (bistable vs. non-bistable) it takes the noisy signal as an input and attempts to return the denoised one. In this case, the autoencoder takes a bistable signal with Gaussian noise, and returns a signal with suppressed noise.

To train our DAE, a noise-free bistable signal, x, is simulated. Then, Gaussian noise is added over the top to produce the noisy signal $\tilde{x}$. This signal is then encoded by running it through convolutional and pooling layers to extract pertinent features and compress it. The now encoded signal, or rather feature map, is then decoded by again running it through convolutional layers, but now using up-sampling rather than pooling. The up-sampling returns the signal to its original size by adding elements with value equal to zero. Adding these zeros forces the autoencoder to learn the important features of the non-zero values in order to 'fill in the gaps'. Finally, the signal is passed through a fully connected layer that produces a denoised reconstruction of the input signal $\hat{x}$ as seen in figure 1. Just like with the classifier, the result is measured against the ground truth, or in this case the original

clean signal x [32], by again using a loss function. For the autoencoder the loss function is a simple mean squares error comparison between each element of the clean signal x and the denoised $\hat{x}$ [33-36].
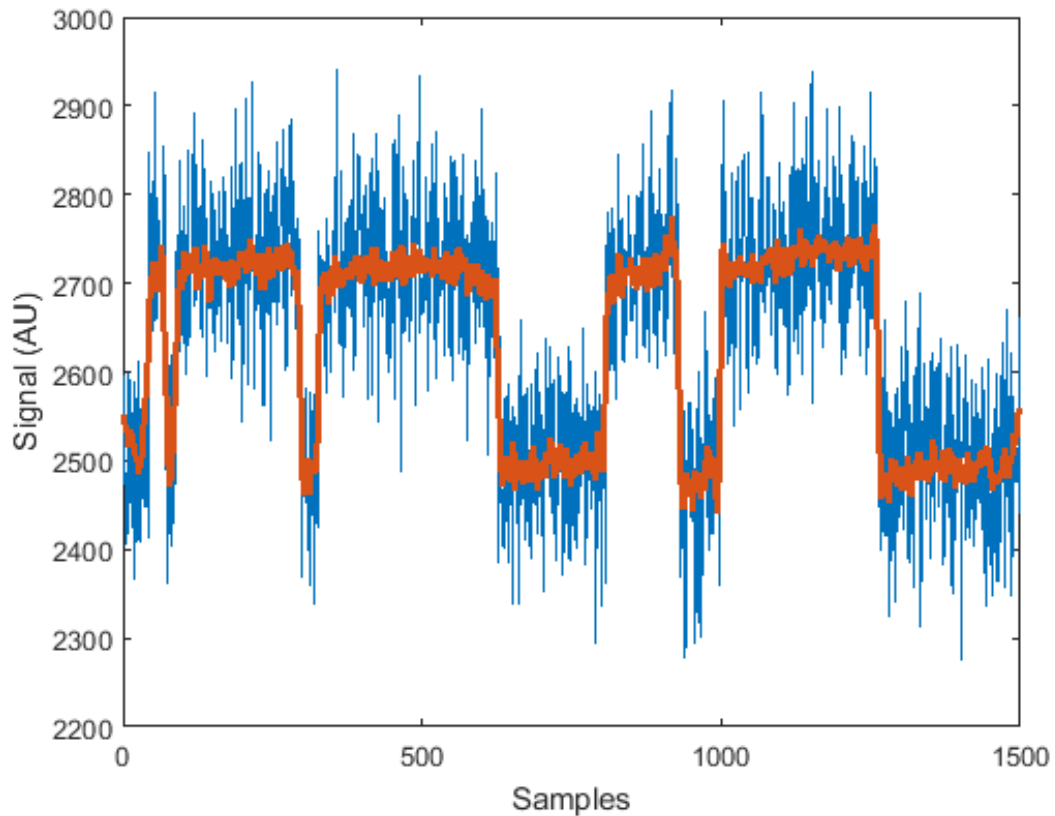
Figure 1: A stochastic bistable signal before (blue) and after (orange) passing through DAE. A significant increase in signal to noise is obvious

3.2. Model Topology and Algorithm Methodology

This bistable signal detection and reconstruction schema was developed in Python and MATLAB using the concepts outlined in the previous section. All machine learning

modeling was performed in Python, while the data preparation and reconstruction finalization was performed in MATLAB. This section outlines the specific choices made with respect to model architecture, and signal processing to carry out the goal of accurate detection and reconstruction.

3.2.1. Classifier Summary

The classification modeling network, shown in figure 2, was developed in Python using Keras [37] as a wrapper over TensorFlow [38]. The layers are structured as such: $Conv(32) \rightarrow Pool(3) \rightarrow Drop(0.5) \rightarrow Conv(64) \rightarrow Pool(3) \rightarrow Drop(0.5) \rightarrow$ $Conv(128) \rightarrow MaxPool() \rightarrow Drop(0.5) \rightarrow Fully\ Connected(1)$. The convolutional layers have 32, 64, and 128 filters respectively with the size of each filter set to 12. Each uses the ReLU activation function. The first two pooling layers take the maximum value, while the last takes an average. The dropout rate is set to 50%. The final layer uses the sigmoid activation function. Training was carried out over five epochs. Figure 2 shows the number and size of the feature maps resulting from the convolution and pooling operations, as well as the final fully connected layer which contains the bistability confidence score.
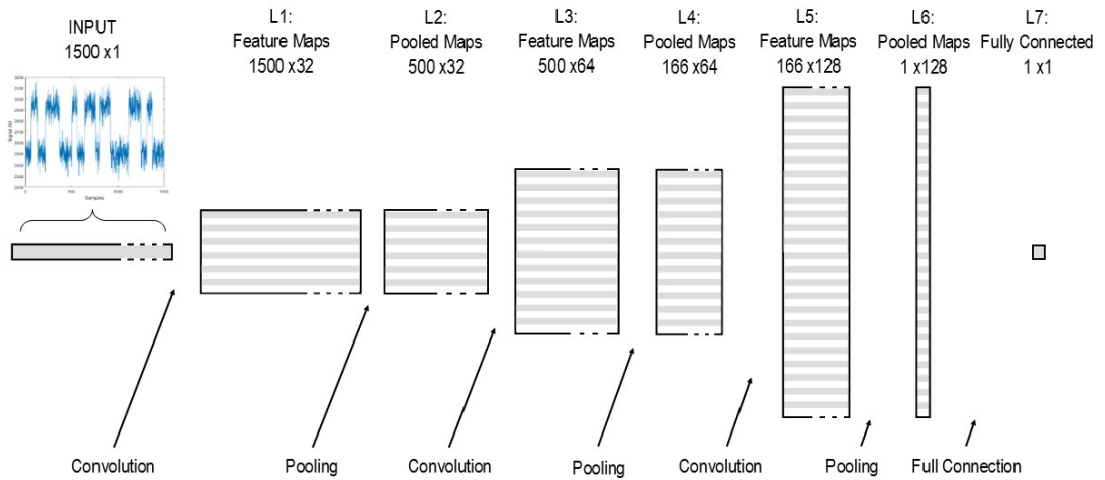
Figure 2: Topology of the bistability classification model. Each signal is passed through 32 convolutional filters to create 32 feature maps. The ReLU activation function is then applied. Those activated feature maps are then pooled down to size 500, passed through the next convolutional layer and activation function to creates a block of 64 feature maps of size 500. The process is repeated once more to create 128 feature maps of size 166 which undergo maxpooling where each feature map is reduced to a single value, its maximum. Those single value maps are then fully connected to the final layer, a single value, which represents the bistability confidence score.

3.2.2. Autoencoder Summary

The denoising autoencoder model, shown in figure 3, was likewise built in Python using Keras as a wrapper over TensorFlow. Its layers are structured as such: Conv(64)→Pool(3)→Conv(32)→Pool(3)→Conv(32)→Upsample(3)→Conv(64)→Upsample(3)→ Fully Connected (1500). The convolutional layers have 64, 32, and 64 filters

respectively while the size of each filter is again set to 12. Each uses the rectified linear unit activation function. The final fully connected layer uses a linear activation function. Training was carried out over five epochs. The squeezing and expansion of the denoising autoencoder, as well as the denoising effect can be seen in figure 3.
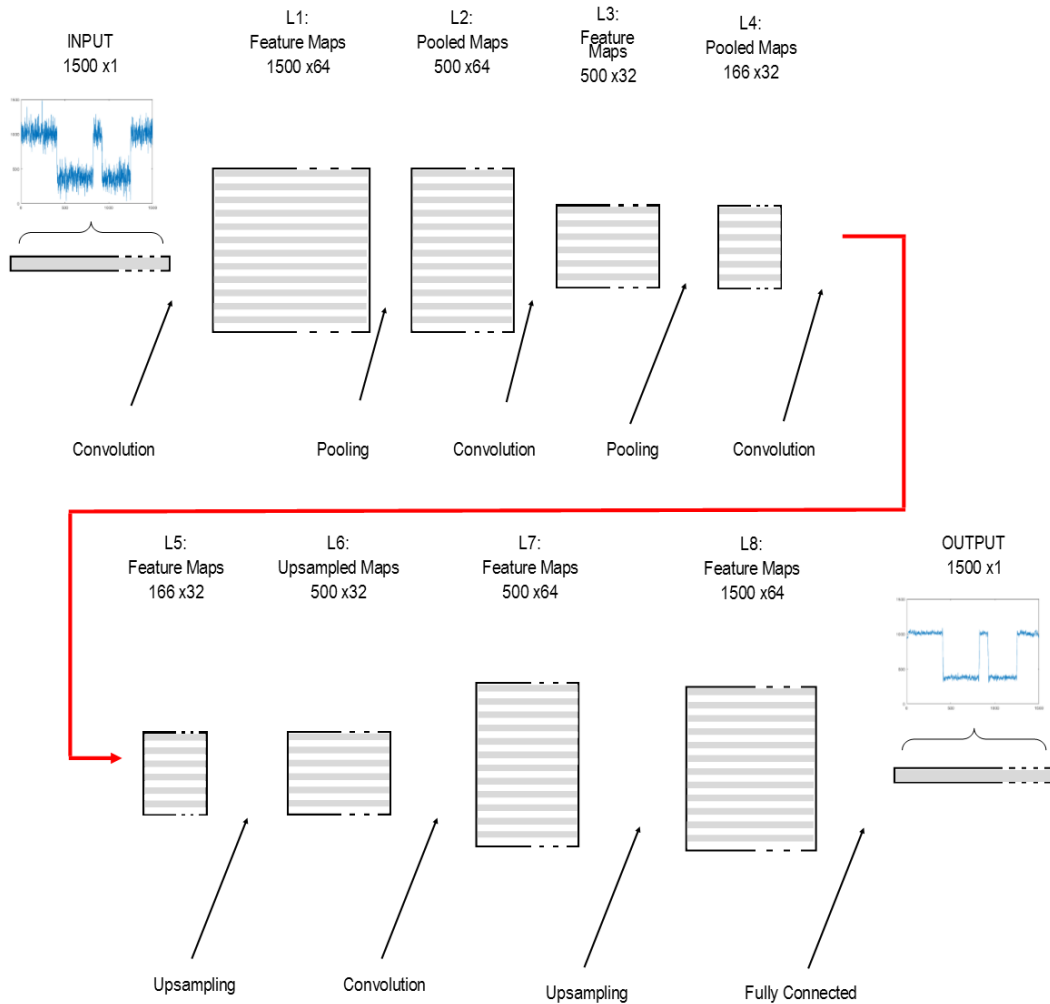
Figure 3: Topology of the denoising autoencoder. Each signal is passed through the convolutional layers similar to the classifier. After the 3rd convolution the feature maps are upsampled rather than pooled to expand them back to their original size. By

upsampling, the model is forced to learn important features of the data in question, which

leads to a denoised version of the input signal.

3.2.3. Training Considerations

One of the more problematic aspects of stochastic bistability is that there are no well-defined limits on amplitude or state lifetime. If either of these key characteristics is sufficiently small it is difficult to distinguish whether or not a signal has bistable state transitions, let alone attempt to reconstruct it without Gaussian noise. It then becomes necessary to create a training set with realistic bistable signals that feature a wide variety of amplitudes and state lifetimes. Simulated signals and noise augmentation have been used previously for training networks related to variety of applications [39-43]. The training set created here has amplitudes from 1 to 450 arbitrary units (AU), spaced evenly by intervals of 1.5 AU, and state lifetimes spaced evenly from 1 to 300 samples, as shown in figure 4. Transitions between bistable states are determined by a decaying exponential probability so that they remain stochastic, but average out to the appropriate state lifetime. Lifetimes for the high and low states were set equal to each other for all bistable signals.
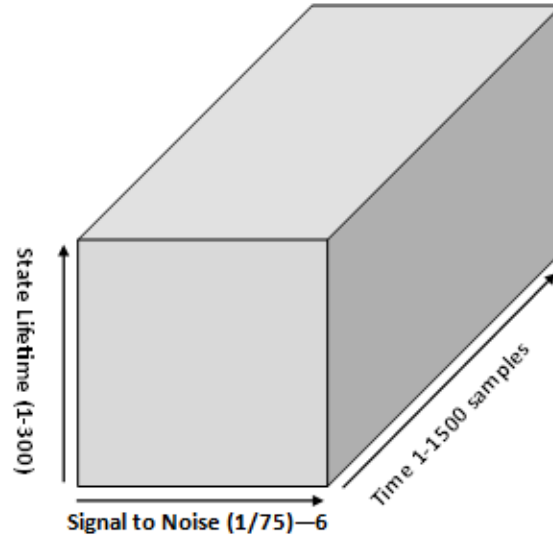
Figure 4: The structure of the training set

Each signal then has Gaussian noise added, with a standard deviation of 75 AU as shown in figure 5. A new quantity is defined for an approximation of the signal to noise ratio which is simply

$$SNR_{BST} = A/\sigma_{Gaussian}$$

where A is the amplitude between states and $\sigma_{Guassian}$ is the Gaussian noise. The range of SNR_{BST} for the training dataset spans from $\frac{1}{75}$ to 6. To train the classifier to separate bistable from non-bistable signals an additional collection of non-bistable signals, Gaussian noise only, were produced. . In total 180,000 signals were created, 90,000 with only Gaussian noise and 90,000 with Gaussian noise and bistable transitions.
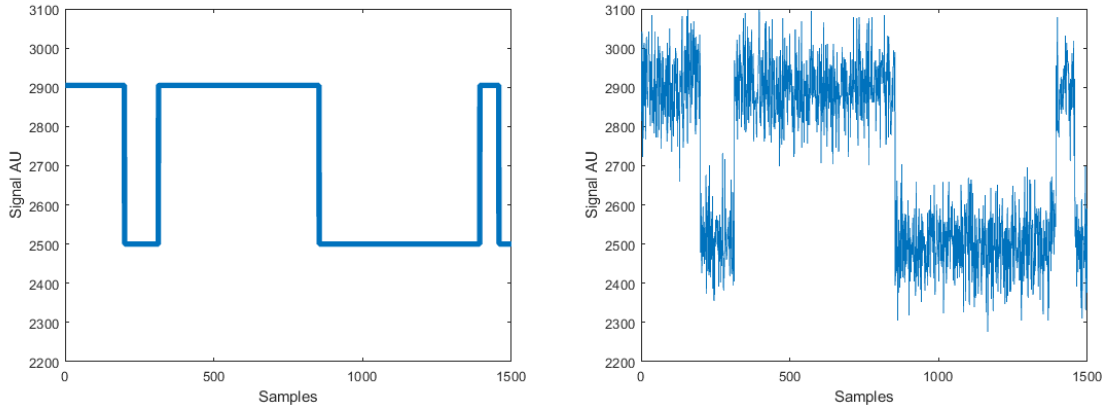
Figure 5: A simulated bistable signal before and after adding Gaussian noise with

$$SNR_{BST} = 5.33.$$

Finally, before training the machine learning models the signals must be scaled, so the shape of the signal, not the magnitude determines the weights of the filters. It was determined that each signal should lie between zero and one, so each signal x is subtracted by a value just below the minimum to create x_s

$$x_s = x - s \; ; \; s = 0.99 * \min{(x)}$$

x_s is then divided by a value just above its maximum to create x_{sd}

$$x_{sd} = \frac{x_s}{d} \; ; \; d = 1.01 * \max{(x_s)}$$

Since the model is trained on scaled signals, any real data processed by it must undergo the same scaling. In order to ensure the mean signal values remain unchanged this scaling must be reversible, so a key is maintained that records s and d for each signal x.

3.2.4. *Gaussian fit level finding*

Recall the total noise of a bistable signal is defined as: $\sigma^2_{SIG} = \sigma^2_{Gaussian} + \sigma^2_{BST}$ which shows the Gaussian noise and bistable transition noise are uncorrelated to one another. Therefore, a histogram of a bistable signal, before and after the autoencoder denoising, will be composed of the sum of Gaussian peaks, one for each state. The reconstruction of a bistable signal is completed by taking a histogram of the autoencoder result, and fitting [44] it as a sum of two Gaussians as shown in figure 6. The new clean signal, figure 7, is created by snapping each element of the autoencoder to whichever peak value from the fitted histogram (see figure 6) is closest to that element. From here the state separation amplitudes and state lifetimes are simply collected.
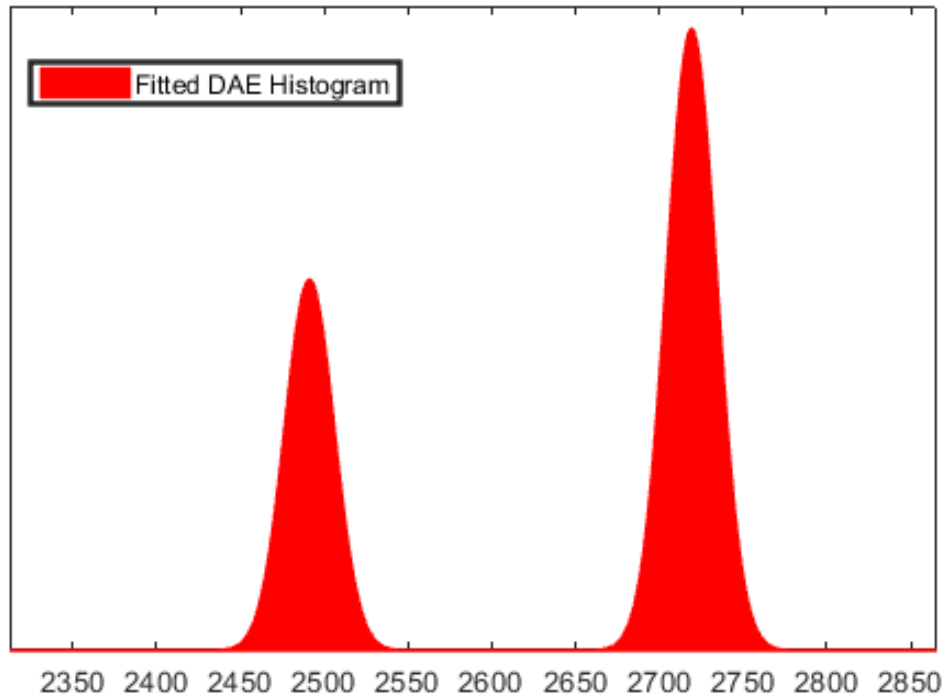
Figure 6: The fitted histogram of the autoencoder results. The final reconstruction uses the values where peaks occur
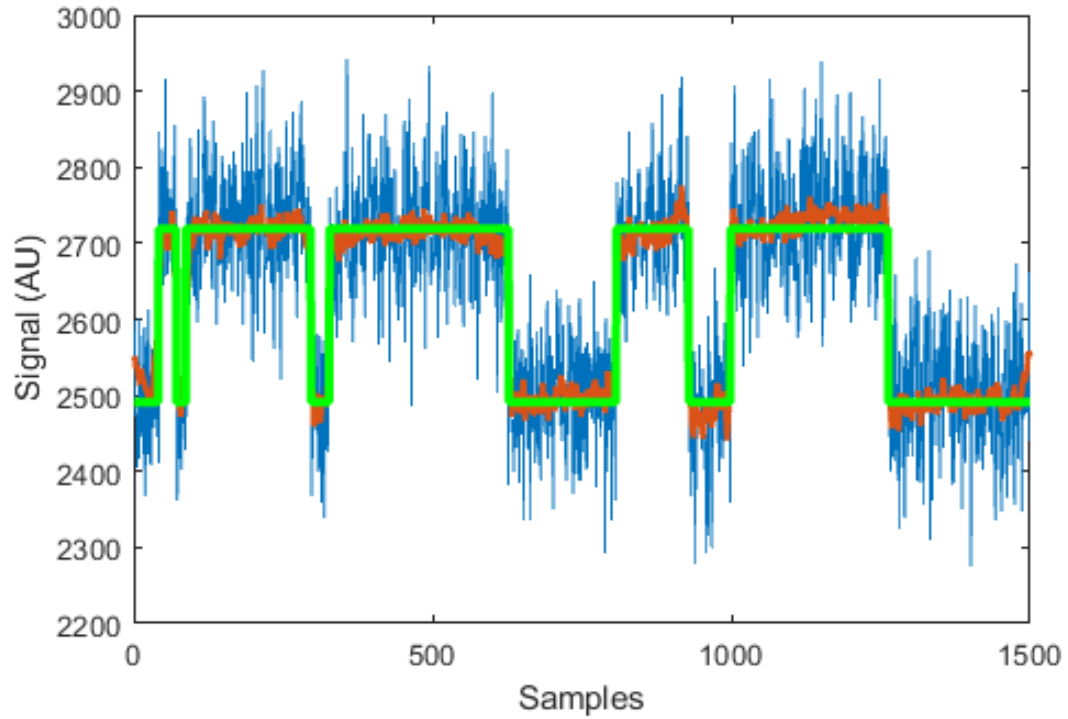
Figure 7: The final reconstruction of a stochastic bistable signal. There are a total of 2

values for the entire signal, with zero Gaussian noise

3.3. Results and discussion

3.3.1. *Simulated Dataset*

In order to measure the efficacy of the classification model, a validation test was carried

out on two additional sets of simulated signals. This test inputs a sample signal to the

model, and records the number of correct and incorrect inferences. Like the training sets,

each is composed of 90,000 signals. The set of bistable signals has state lifetimes that span

from 1 to 300 samples, and amplitudes such that the SNR_{BST} runs from $\frac{1}{75}$ to 6. All signals

are scaled as described above before running them through the algorithm.

The algorithm detected 83.5% of the bistable signals, and recorded zero false positives from the non-bistable test set. It works remarkably well on bistable signals that have a $SNR_{BST} > 1.5$ and lifetimes longer than about 20 samples as seen in figure 8.
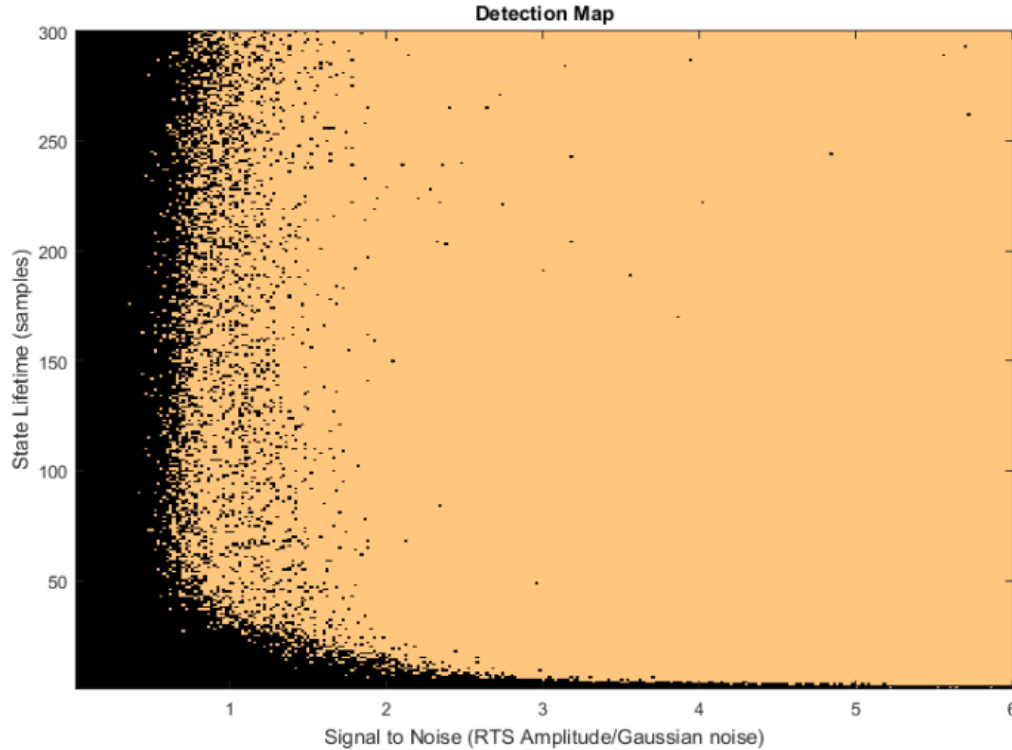
Figure 8: The bistable signal detection map. Black areas are where the detection model failed

Each signal that passed detection was then scored on the quality of reconstruction by means of the sample correlation coefficient. This is a great advantage of testing on a simulated data set since each reconstruction can be directly compared to the original clean signal. The sample correlation coefficient is calculated as

$$C_{xy} = \frac{\Sigma(x_i - \overline{x})(y_i - \overline{y})}{\sqrt{\Sigma(x_i - \overline{x})^2}\sqrt{\Sigma(y_i - \overline{y})^2}}$$

where C_{xy} is the correlation coefficient or score, x_i is the value of the ith element in the reconstructed signal, $\bar{x}$ is the mean of the reconstructed signal, y_i is the value of the ith element in the original clean signal, and $\bar{y}$ is the mean of the original clean signal. The coefficient lies between -1 and 1 where -1 is perfectly anticorrelated, 0 is uncorrelated and 1 is perfectly correlated. In practice negative scores are possible, but exceedingly rare. Nearly all bistable signal detections resulted in a highly accurate reconstruction as seen in figure 9 and punctuated by table 1. The mean correlation score for detected bistable signals is 0.978 [45].
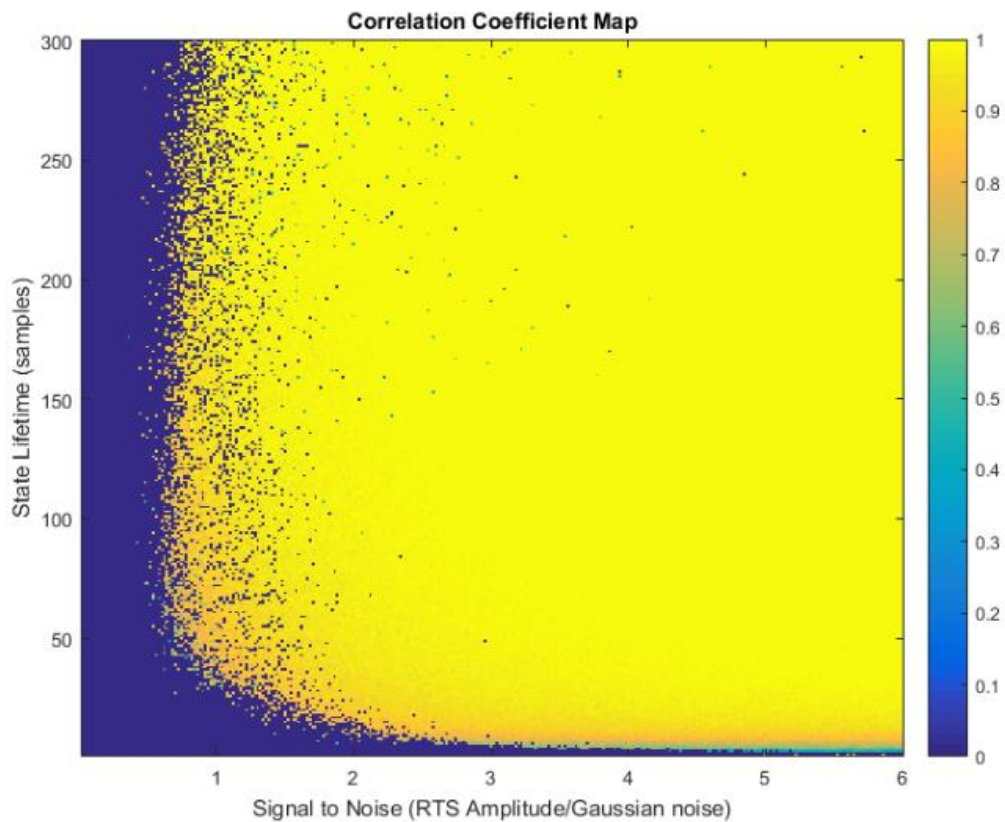
Figure 9: The sample correlation coefficient map. For the vast majority of signals that passed detection, reconstruction is near perfect

Correlation Range	Counts
$0 < C_{xy} < 0.4$	68
$0.4 \leq C_{xy} < 0.6$	257
$0.6 \leq C_{xy} < 0.7$	251
$0.7 \leq C_{xy} < 0.8$	730
$0.8 \leq C_{xy} < 0.9$	2,523
$0.9 \leq C_{xy} < 0.99$	21,613
$C_{xy} \geq 0.99$	49,659

Table 1: The correlation score counts highlight the quality of reconstruction for a great

majority of pixels
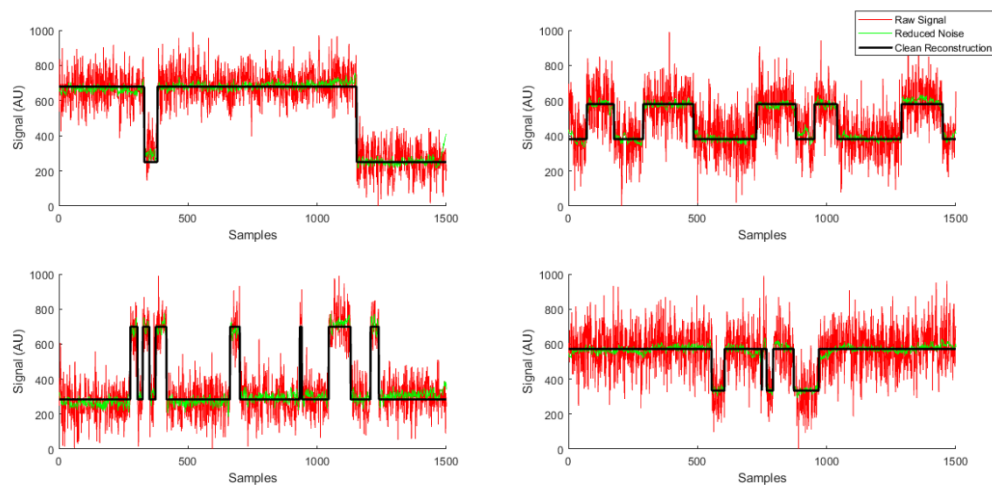
Figure 10: Reconstructions of four randomly selected RTS pixels.

3.3.2. RTS Image Sensor Data

A commonly observed bistable phenomenon is Random Telegraph Signal (RTS) noise in silicon devices, particularly image sensors. RTS noise in sensors is typically the consequence of exposure to radiation. The bistability is produced by discrete changes in the generation rate of leakage current, known in image sensors as dark current [46]. RTS noise in image sensors has been previously analyzed in a number of ways. Usually a lengthy time series is created for pixels of interest by collecting many (a few thousand) frames at regular intervals. This series is then analyzed to identify RTS behavior and extract characteristics of interest. RTS is one of the major noise sources that remains difficult to mitigate in both CMOS and CCD image sensors.

To provide an example of the results this detection and reconstruction algorithm may yield frames were collected from a charge-coupled device (CCD) and stacked together. Then the temporal response from individual pixels was analyzed and reconstructed as if each were an independent device (see figure 10). The sensor used is a SITe SI-033AF frontside illuminated 1 mega-pixel CCD ($1024x1024$) [47]. Frames were taken in dark conditions with 10 second integration time at 305 K.

As illustrated by the four random RTS pixels shown in figure 10, the collected CCD dark current data showed that the method described here is capable of creating quality noise free reconstructions of bistable stochastic signals. It was expected, perhaps naively, that the wide range of state lifetimes and amplitudes characteristic of RTS signals would cause some issues, but none have arisen yet. While this result is promising, additional validation is required by testing it on different sources of data.

3.4. Conclusion

A machine learning based algorithm is presented for the reconstruction and analysis of stochastic bistable signals. The algorithm uses a convolutional classifier for the identification of state transitions, and a convolutional denoising autoencoder to increase the bistable amplitude signal to noise level. A histogram of the decoded signal values is taken and fit to the sum of two Gaussians. Finally, the signal is reconstructed by snapping each value of the decoded signal to the nearest peak location.

Quantitatively, the algorithm was shown to be successful by running it on a set of simulated bistable and non-bistable signals. It detected over 83% of the bistable signals, and only consistently failed on signals with a $SNR_{BST} < 1$. Reconstruction for signals that passed detection is exceptional, reaching an almost perfect correlation coefficient of 0.99 or greater for nearly 66% of detected signals.

Qualitatively, the algorithm proved capable on a set of data collected by taking dark frames with a CCD image sensor. In the case of image sensors in particular, additional steps need to be taken to address issues stemming from cosmic rays and thermal fluctuations, but once mitigated near perfect reconstruction of an RTS signal is expected.

3.5 References

[1] E. Rhoades, E. Gussakovsky, G. Haran, Watching proteins fold one molecule at a time. Proc. Natl. Acad. Sci. USA. 100 (2003) 3197-3202.

[2] H.S. Chung, K. McHale, J. M. Louis, W. A. Eaton, Single-Molecule Fluorescence Experiments Determine Protein Folding Transition Path Times, Science. (2012) 981-984.

[3] L. Edman, Z. Földes-Papp, S. Wennmalm, R. Rigler, The fluctuating enzyme: a single molecule approach, Chem. Phys., Volume 247, Issue 1 (1999) 11-22.

[4] H.P. Lu, L. Xun, X.S. Xie, Single-Molecule Enzymatic Dynamics, Science. (1998) 1877-1882.

[5] X. Zhuang, H. Kim, M.J.B. Pereira, H.P. Babcock, N.G. Walter, S. Chu, Correlating Structural Dynamics and Function in Single Ribozyme Molecules, Science, (2002) 1473-1476.

[6] K. Velonia, O. Flomenbom, D. Loos, S. Masuo, M. Cotlet, Y. Engelborghs, J. Hofkens, A.E. Rowan, J. Klafter, R.J.M. Nolte, F.C. de Schryver, Single enzyme kinetics of CALB catalyzed hydrolysis, Angew. Chem. Int. Ed. Engl., 44 (2005) 560-564.

[7] R.C. Klipp, N. Li, Q. Wang, T.A. Word, M. Sibrian-Vazquez, R.M. Strongin, X.H.T. Wehrens, J.J. Abramson, EL20, a potent antiarrhythmic compound, selectively inhibits calmodulin-deficient ryanodine receptor type 2, Heart Rhythm, 15 (2018) 578-586.

[8] V. Krishnamurthy et al., Gramicidin Ion Channel-Based Biosensors: Construction, Stochastic Dynamical Models, and Statistical Detection Algorithms, IEEE Sensors Journal, 7 (2007) 1281-1288.

[9] S. Oiki, H. Shimizu, M. Iwamoto, and T. Konno, Single-Molecular Gating Dynamics for the KcsA Potassium Channel, Single-Molecule Biophysics, (2011) 147-193.

[10] D. R. Crick, S. Donnellan, D. M. Segal, and R. C. Thompson, Magnetically induced electron shelving in a trapped Ca+ ion, Phys. Rev. A, 81-052503 (2010) 1-4.

[11] S. Reick, K. Mølmer, W. Alt, M. Eckstein, T. Kampschulte, L. Kong R. Reimann, A. Thobe, A. Widera and D. Meschede, Analyzing quantum jumps of one and two atoms strongly coupled to an optical cavity, J. Opt. Soc. America B, 27 (2010) A152-A163.

[12] J. Jin, J. Guo, J. Luo, X. Li, and Y. Yan, Quantum trajectory analysis for electrical detection of single-electron spin resonance, Phys. Rev. B, 73 (2005) 125312.1-5.

[13] P.L. Leonard and S.V. Jaskolski, An investigation into the origin and nature of "Popcorn noise", Proceedings of the IEEE, 57 (1969) 1786-1788.

[14] J. Bogaerts, B. Dierickx and R. Mertens, Random telegraph signals in a radiation-hardened CMOS active pixel sensor, IEEE Trans. on Nucl. Sci., 49 (2002) 249-257.

[15] W.H. Chard and P.K. Chaudhari, Characteristics of burst noise, Proc. IEEE, 53 (1965) 652.

[16] E. Simoen, B. Dierickx, C. L. Claeys, and G. J. Declerck, Explaining the amplitude of RTS noise in submicrometer MOSFETs, IEEE Trans. Electron Devices, 39 (1992) 422.

[17] V. Goiffon, P. Magnan, P. Martin-Gonthier, C. Virmontois, and M. Gaillardin, New source of random telegraph signal in CMOS image sensors, International Image Sensor Workshop, Hokkaido, Japan, (2011)

[18] W.H. Press, Flicker noises in astronomy and elsewhere, Comments on Modern Physics, Part C - Comments on Astrophysics, 7 (1978) 103-119.

[19] Q. Wang, P. Du, J. Yang, G. Wang, J. Lei, C. Hou, Transferred deep learning based waveform recognition for cognitive passive radar, Signal Process., 155 (2019) 259-267.

[20] T. Ölmez, Z. Dokur, Classification of heart sounds using an artificial neural network, Pattern Recognition Letters, 24 (2003) 617-629.

[21] K. Basu, V. Debusschere, A. Douzal-Chouakria, S. Bacha, Time series distance-based methods for non-intrusive load monitoring in residential buildings, Energy and Buildings, 96 (2015) 109-117.

[22] Y. Chen, G. Zhang, M. Bai, S. Zu, Z. Guan, and M. Zhang, Automatic Waveform Classification and Arrival Picking Based on Convolutional Neural Network, Earth and Space Science, (2019) 1-77.

[23] Z. Xiong, M.K. Stiles, J. Zhao, Robust ECG Signal Classification for Detection of Atrial Fibrillation Using a Novel Neural Network, Computing in Cardiology, 44, 2017.

[24] T. Guo, J. Dong, H. Li and Y. Gao, Simple convolutional neural network on image classification, 2017 IEEE 2nd International Conference on Big Data Analysis (ICBDA), Beijing, (2017) 721-724.

[25] J. Li, Y. Si, L. Lang, L. Liu, T. Xu, A Spatial Pyramid Pooling-Based Deep Convolutional Neural Network for the Classification of Electrocardiogram Beats, Appl. Sciences, 8 (2018) 1590.

[26] Z. Hu, Y. Li and Z. Yang, Improving Convolutional Neural Network Using Pseudo Derivative ReLU, 2018 5th International Conference on Systems and Informatics (ICSAI), Nanjing, (2018) 283-287.

[27] M.D. Zeiler and R. Fergus, Visualizing and understanding convolutional networks, ECCV, volume 8689 of Lecture Notes in Computer Science, Springer (2014) 818–833.

[28] D. Ciresan, U. Meier, J. Masci, L. Gambardella, and J. Schmidhuber, Flexible, High Performance Convolutional Neural Networks for Image Classification, International Joint Conference on Artificial Intelligence (2011) 1237-1242.

[29] G.E. Hinton, N. Srivastava, A. Krizhevsky, I. Sutskever, and R. Salakhutdinov, Improving neural networks by preventing co-adaptation of feature detectors, ArXiv (2012)

[30] Y. Lecun, L. Bottou, Y. Bengio and P. Haffner, Gradient-based learning applied to document recognition, Proceedings of the IEEE, 86 (1998) 2278-2324.

[31] P. Sadowski, Notes on backpropagation, (2016). [Online]. Available: https://www.ics.uci.edu/

[32] C. Lu, Z. Wang, W. Qin, J. Ma, Fault diagnosis of rotary machinery components using a stacked denoising autoencoder-based health state identification, Signal Process., 130 (2017) 377-388.

[33] L. Gondara, Medical Image Denoising Using Convolutional Denoising Autoencoders, 2016 IEEE 16th International Conference on Data Mining Workshops (ICDMW), Barcelona, (2016) 241-246.

[34] P. Vincent, H. Larochelle, I. Lajoie, Y. Bengio, and P.-A. Manzagol. Stacked denoising autoencoders: Learning useful representations in a deep network with a local denoising criterion. In Proceedings of the 27th International Conference on Machine Learning, (2010) 3371–3408.

[35] G. Hinton *et al*., Deep Neural Networks for Acoustic Modeling in Speech Recognition: The Shared Views of Four Research Groups, IEEE Signal Process. Mag., 29 (2012) 82-97.

[36] X. Ye, L. Wang, H. Xing and L. Huang, Denoising hybrid noises in image with stacked autoencoder, 2015 IEEE International Conference on Information and Automation, Lijiang, (2015) 2720-2724.

[37] Chollet, François and others, Keras, (2015) [Online]. Available: www.keras.io

[38] M. Abadi, A. Agarwal, P. Barham, E. Brevdo, Z. Chen, C. Citro, G.S. Corrado, A. Davis, J. Dean, M. Devin, S. Ghemawat, I. Goodfellow, A. Harp, G. Irving, M. Isard, R. Jozefowicz, Y. Jia, L. Kaiser, M. Kudlur, J. Levenberg, D. Mané, M. Schuster, R. Monga, S. Moore, D. Murray, C. Olah, J. Shlens, B. Steiner, I. Sutskever, K. Talwar, P. Tucker, V. Vanhoucke, V. Vasudevan, F. Viégas, O. Vinyals, P. Warden, M. Wattenberg, M. Wicke, Y. Yu, and X. Zheng, TensorFlow: Large-scale machine learning on heterogeneous systems, (2015) [Online]. Available from www.tensorflow.org

[39] M. Carrillo et al, Time series analysis of gravitational wave signals using neural networks, J. Phys.: Conf. Ser. 654 012001, (2015).

[40] M. Takadoya, M. Notake, M. Kitahara, J.D. Achenbach, Q.C. Guo and M.L. Peterson, Crack-Depth Determination By A Neural Network With A Synthetic Training Data Set, Review of Progress in Quantitative Nondestructive Evaluation, 12, (1993) 803-810.

[41] N. J. Rodriguez-Fernandez, P. Richaume, Y. H. Kerr, F. Aires, C. Prigent and J. Wigneron, Global retrieval of soil moisture using neural networks trained with synthetic radiometric data, 2017 IEEE International Geoscience and Remote Sensing Symposium (IGARSS), Fort Worth, TX, (2017) 1581-1584.

[42] T. A. Le, A. G. Baydin, R. Zinkov and F. Wood, Using synthetic data to train neural networks is model-based reasoning, 2017 International Joint Conference on Neural Networks (IJCNN), Anchorage, AK, (2017) 3514-3521.

[43] A. Witmer and B. Bhanu, HESCNET: A Synthetically Pre-Trained Convolutional Neural Network for Human Embryonic Stem Cell Colony Classification, 2018 25th IEEE International Conference on Image Processing (ICIP), Athens, (2018) 2441-2445.

[44] T.C. O'Haver, Pragmatic Introduction to Signal Processing 2019: Applications in scientific measurement. Kindle Direct Publishing, (2019) p. 340.

[45] N. Bershad and A. Rockmore, On estimating signal-to-noise ratio using the sample correlation coefficient (Corresp.), IEEE Transactions on Information Theory, 20 (1974) 112-113.

[46] K. Ackerson et al., Characterization of "blinking pixels" in CMOS Image Sensors, 2008 IEEE/SEMI Advanced Semiconductor Manufacturing Conference, Cambridge, MA, (2008) 255-258.

[47] SITe SI03xA 24 µm Charge-Coupled Device Family, SITe, Tigard, OR, (2003) [Online]. Available:

http://www.not.iac.es/instruments/detectors/CCD1/S103xA_family.pdf

CHAPTER FOUR – A COMPARISON OF THREE METHODS FOR BISTABLE RANDOM TELEGRAPH SIGNAL DETECTION AND RECONSTRUCTION

Coauthored with Ralf Widenhorn and Erik Bodegom

Abstract—Random Telegraph Signal (RTS) noise is a common problem in image sensors that affects image and video quality. A consequence of radiation exposure, RTS noise causes discrete changes in dark current generation in pixels which degrades sensors and reduces the fidelity of scientific imagery. We present a comparison of three methods for the reconstruction of RTS signals which is useful for analyzing key characteristics and correcting for this discrete variation. The methods are tested both on simulated data to provide a controlled experiment that scores reconstructed signals against their noise-free counterparts and on data collected from a charge-coupled device to compare their effectiveness in real life application.

Keywords—Bistable signal, two-state system, random telegraph signal, convolutional filter, wavelet transform, denoising autoencoder, machine learning, CMOS and CCD image sensors

4.1. – Introduction

4.1.1. Random Telegraph Signal Noise

Random Telegraph Signal (RTS) noise is a variety of metastable stochastic noise that is commonly bistable, and known to degrade image and video quality [1]. RTS is recognized by discrete jumps in signal output, seen in figure 1, that occur on a wide variety of time scales, and with a wide variety of amplitudes [2]. Both total ionizing dose (TID) and displacement damage (DD) are known to produce RTS defects in image sensors. TID from x-rays and γ-rays has been shown to create RTS centers along the Si/SiO_2 interface where

amorphous structures dominate, while DD from accelerated protons and neutrons cause

RTS centers to form inside the bulk itself shown in figure 2 [3].
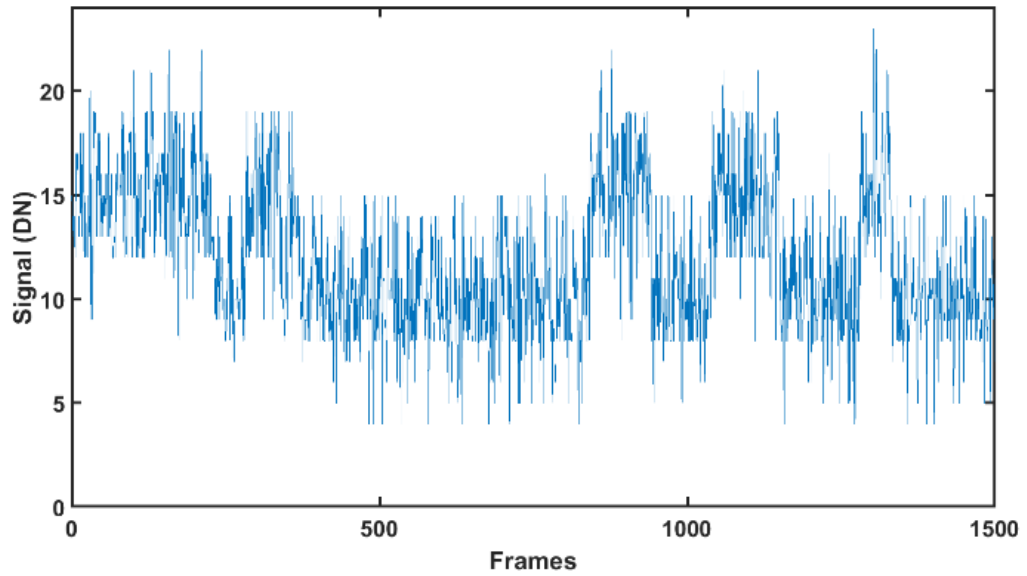
Figure 1: A prototypical bistable RTS-Noise Signal.
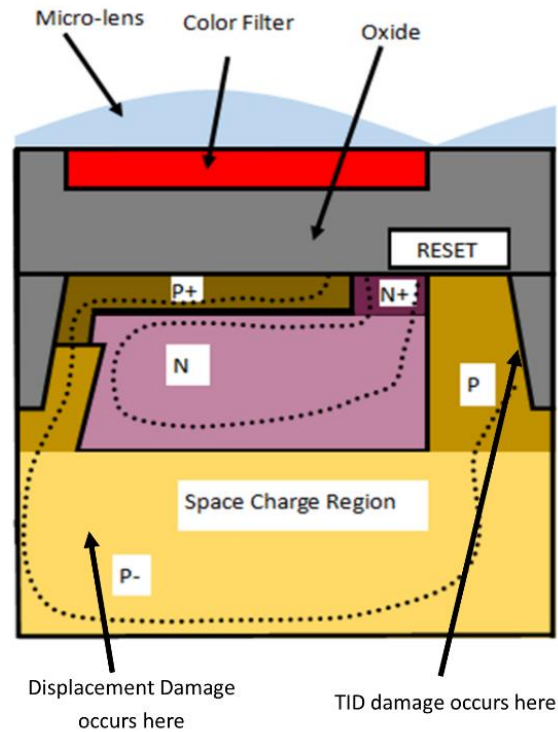
Figure 2: Pixel structure of a 3T CMOS image sensor and RTS defect locations.

There are two varieties of RTS noise pertinent to image sensors, source follower RTS (SF-RTS), and dark current RTS (DC-RTS). SF-RTS is caused by the trapping and emission of charges in the source follower amplifier found in CMOS pixel structures [4]. DC-RTS is thought to be caused by the turning on and off of metastable Shockley-Read-Hall (SRH) generation/recombination (G/R) [5] [6] centers somewhere in the space charge region of the photodiode [7]. This is supported by measurement of their activation energies near the mid-gap level ($\sim 0.56 eV$) [8]. The structure of these SHR centers and the mechanism of their metastability has yet to be confirmed, however, it is differentiated from SF-RTS by

its relatively long state lifetimes which can be hours long versus milliseconds, and its amplitude dependence on integration time.

Mathematically, bistable RTS is assumed to be an uncorrelated noise source from thermal Gaussian noise. The total noise of an RTS signal is then defined as:

$$\sigma_{sig}^2 = \sigma_{Gaussian}^2 + \sigma_{RTS}^2$$

where σ_{sig}^2 is the variance of the signal, $\sigma_{Gaussian}^2$ is the variance from the Gaussian noise, and σ_{RTS}^2 is the variance contribution from RTS transitions.

4.1.2. Signal Reconstruction Goals and Benchmarks

In order to satisfactorily reconstruct a noisy signal two central objectives must be achieved. The signal must be completely noise free and the shape and scale of the signal must be faithfully reproduced as seen in figure 3.
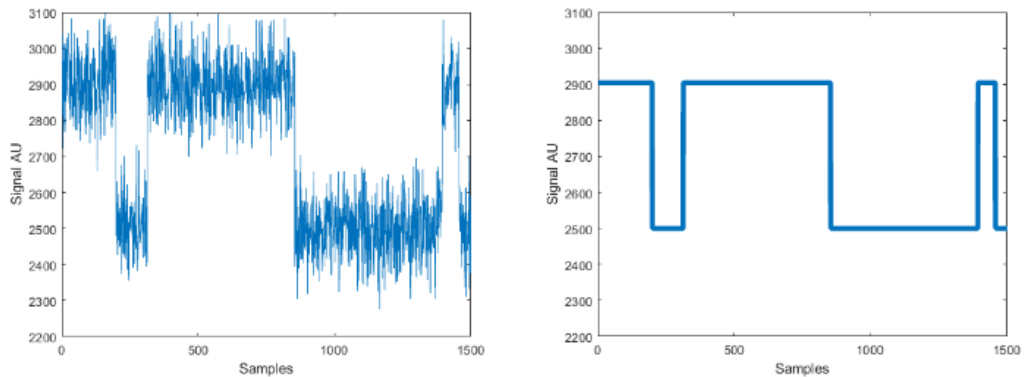
Figure 3: A perfect noise free reconstruction of an RTS signal.

74

In the case of RTS signals this means that there should be zero Gaussian noise, and the RTS transitions occur at the same time, with identical amplitudes. This can be a difficult task for any algorithm working on RTS signals, since neither the amplitude nor state lifetimes are rigidly defined and both are unbounded. The same sensor may have RTS pixels with easily spotted transitions and also ones buried in Gaussian noise. Lifetimes may last nearly the entire measurement period, or be as short as one or two samples making them difficult to distinguish from Gaussian noise. Therefore it is important that any algorithm built to reconstruct these kinds of signals be flexible enough to handle a wide spectrum of these characteristics.

We provide a description of the three methods that have been used: a convolutional method, a method based on the use of wavelets, and a machine learning method.

4.2. – Description of Three Reconstruction Methods

4.2.1. Convolutional Filtering

The first method discussed here, which is widely used in RTS signal analysis, is a method built on convolutional filtering. Developed and outlined by V. Goiffon et. al. in 2009 [9], the goal is to slide a step shaped filter across the signal of interest which suppresses Gaussian noise while preserving the RTS transitions. The filter is written as:

$$H(z) = \frac{2}{L}\left(-\sum_{i=0}^{\frac{L}{2}} z^{-i} + \sum_{i=\frac{L}{2}}^{L-1} z^{-i} \right)$$

L, the length of the filter, will be set to 50 in the following analysis.

Once the filter has been applied to a signal, it marks it as RTS if the amplitude of any of the resulting spikes are larger than the standard deviation of the signal, i.e., $A_{RTS} > \sigma_{sig}$. From there, the mean values of sections between the spikes are collected and the signal is reconstructed as seen in figure 4. If two sections share a similar mean (less than σ_{sig}), their values are averaged together and both are assigned that new value. It should be noted that this method is capable of reconstructing RTS signals with more than two levels, which occurs rarely unless a significant radiation dose is absorbed.
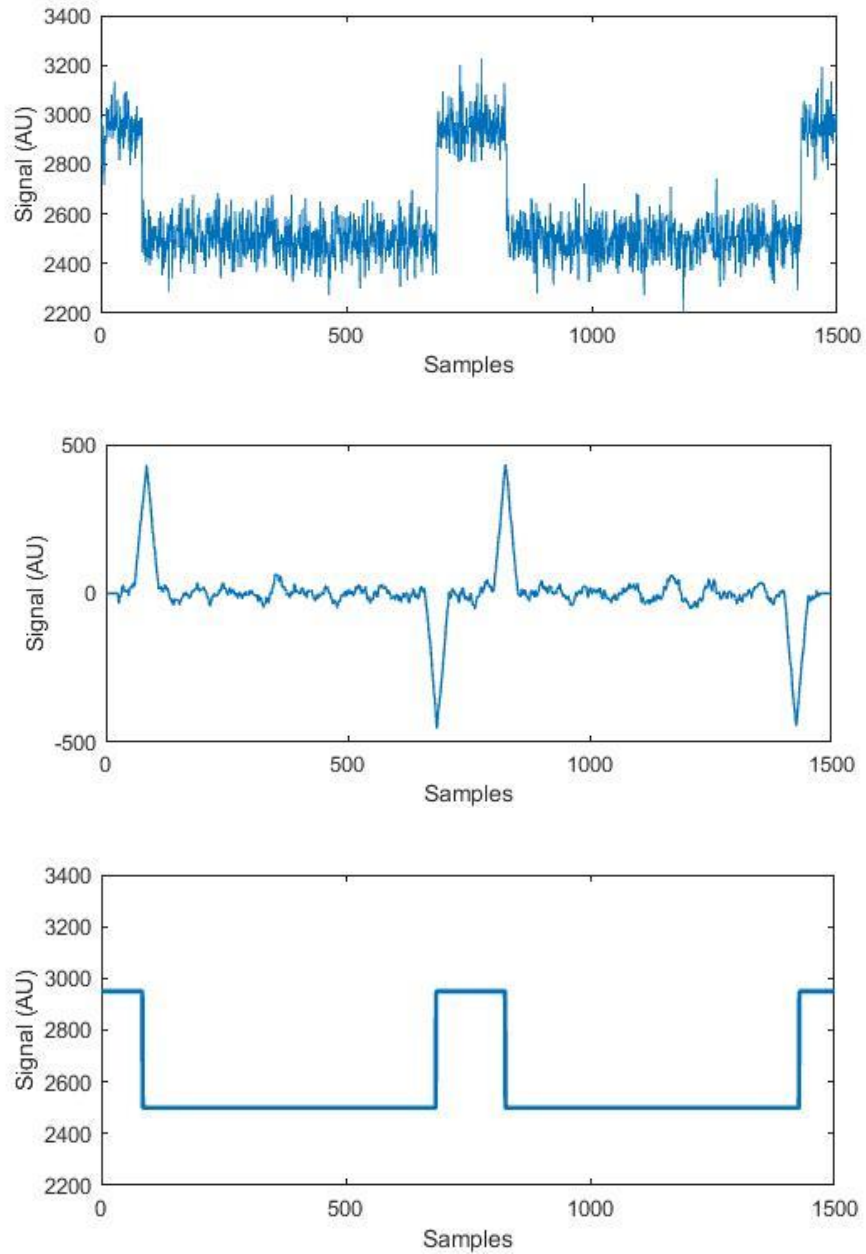
Figure 4: The central stages of the convolutional method. A signal of interest (top) is convolved with the step shaped filter to suppress Gaussian noise and preserve the location and magnitude of RTS transitions (middle). Finally, the signal is reconstructed (bottom) using information from the raw input, and filtered output.

4.2.2. Wavelet Denoising

Wavelet analysis is a popular technique in modern signal and image analysis [10] [11] [12] [13] [14]. The wavelet transform has proven to be an effective tool for compression and noise filtering alike, in no small part because there are a variety of wavelet kernels to pick from. Each has its own characteristics that may provide an advantage over another depending on the shape of signal being analyzed. The kernel used here is the Haar wavelet, since, like the convolutional filter, it is step shaped, so ideal for detecting RTS transitions.

The following method is similar to the one developed by B. Hendrickson et. al. [15] . It begins with the Haar wavelet transform, where a signal of interest, $\mathbf{f} = (f_1, f_2, f_3, ... f_N)$, is transformed to create two daughter vectors $\mathbf{a}$ and $\mathbf{d}$ as shown in figure 5 [16]. The vector $\mathbf{a}$ is known as the trends vector, and is created by taking a running average along the signal. Its coefficients are computed as follows:

$$a_m = \frac{f_{2m-1} + f_{2m}}{\sqrt{2}} \qquad 1 < m \le N/2$$

The vector $\mathbf{d}$ is known as the details vector, and is created by taking a running difference along the signal, similar in function to a running derivative. Its coefficients are computed as follows:

$$d_m = \frac{f_{2m-1} - f_{2m}}{\sqrt{2}} \qquad 1 < m \le N/2$$

78
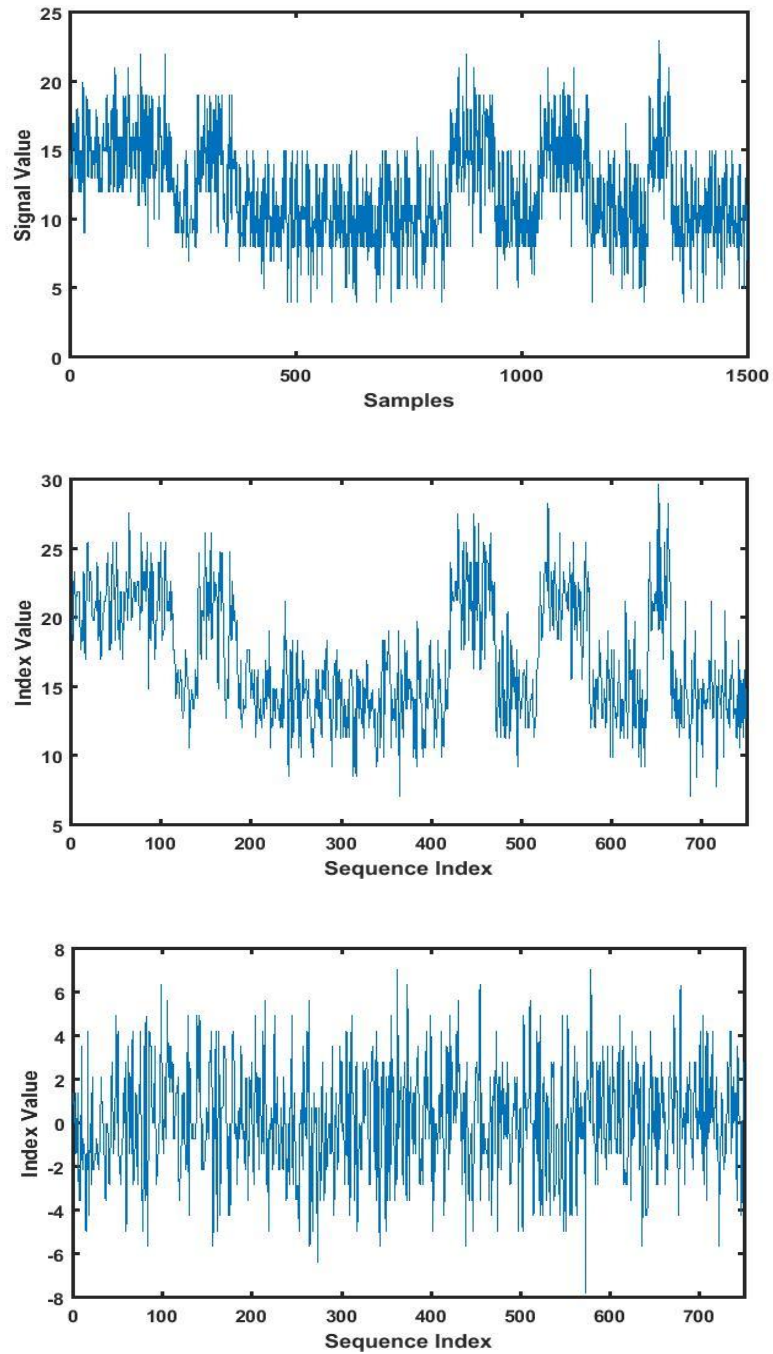
Figure 5: The input signal **f** (top), trends vector **a** (middle), and details vector **d**

(bottom).

The reverse transform is performed by combining the members of the trends and details vectors like so:

$$\mathbf{f} = (\frac{a_1 + d_1}{\sqrt{2}}, \frac{a_1 - d_1}{\sqrt{2}}, \ldots \frac{\frac{a_N + d_N}{2}}{\sqrt{2}}, \frac{\frac{a_N - d_N}{2}}{\sqrt{2}})$$

Notice that both the trends and details vectors are half the size of the input series. This dyadic characteristic of the wavelet transform allows one of its most important characteristics, multi-resolution analysis. By transforming subsequent iterations of the trends vector, the signal can by analyzed on a variety of resolutions.

Actually denoising the signal involves operating on the resultant details vector. A threshold is set, in this case the Universal Threshold as described by Donoho and Johnstone, defined as $T = \hat{\sigma}\sqrt{2\log(n)}$ [17] where $\hat{\sigma}$, an estimate of the noise, is the median magnitude of the details vector divided by the 0.75 quantile of a normal distribution, or $u_{0.75} = 0.6745$ [18]. n is the length of the vector.

Once the threshold is set, all values of the details vector whose magnitude falls below the threshold are set to zero as seen in figure 6. This is known as a hard thresholding.
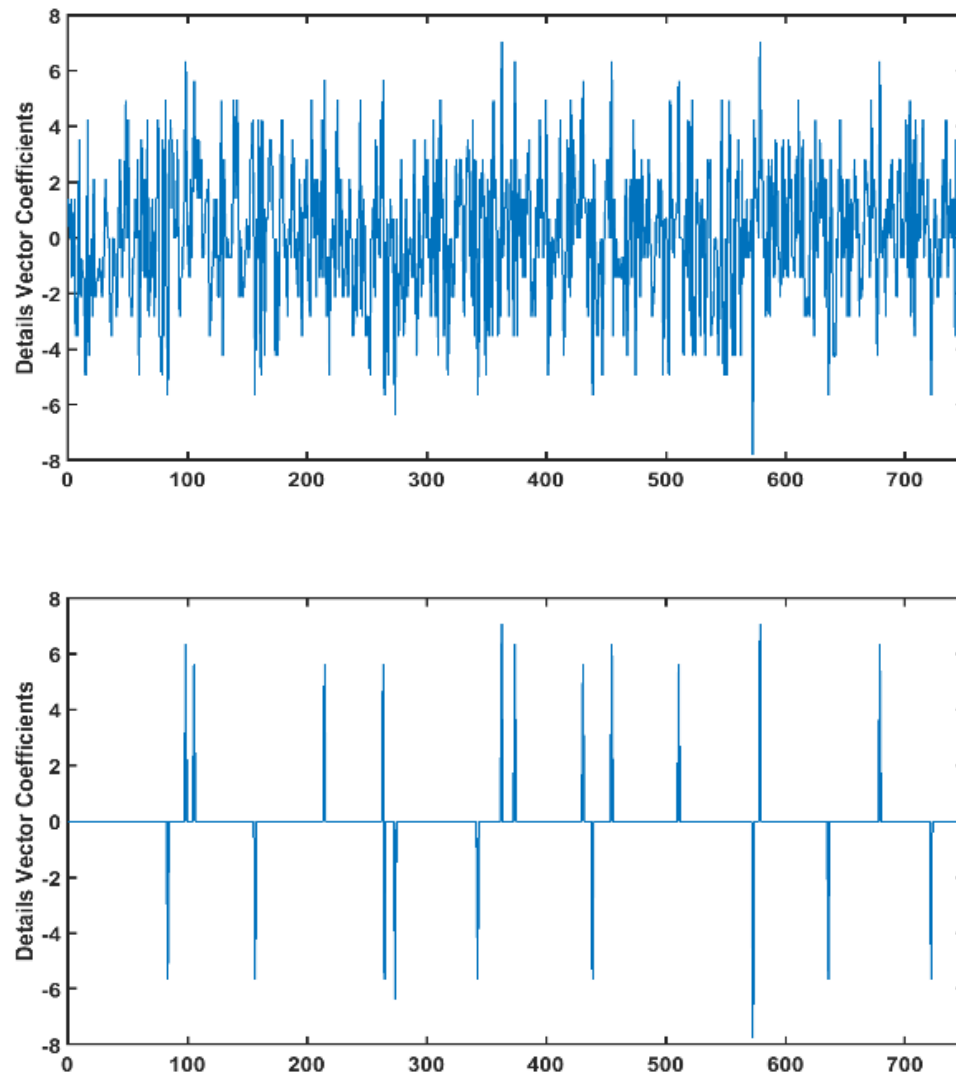
Figure 6: A details vector before and after hard thresholding.

Now that many of the members of the details vector are set to zero the inverse transform results in a much denoised version of the input signal. From here the mean levels are collected and sorted much in the same way as the convolutional method and a noise-free reconstruction is created, shown in figure 7.
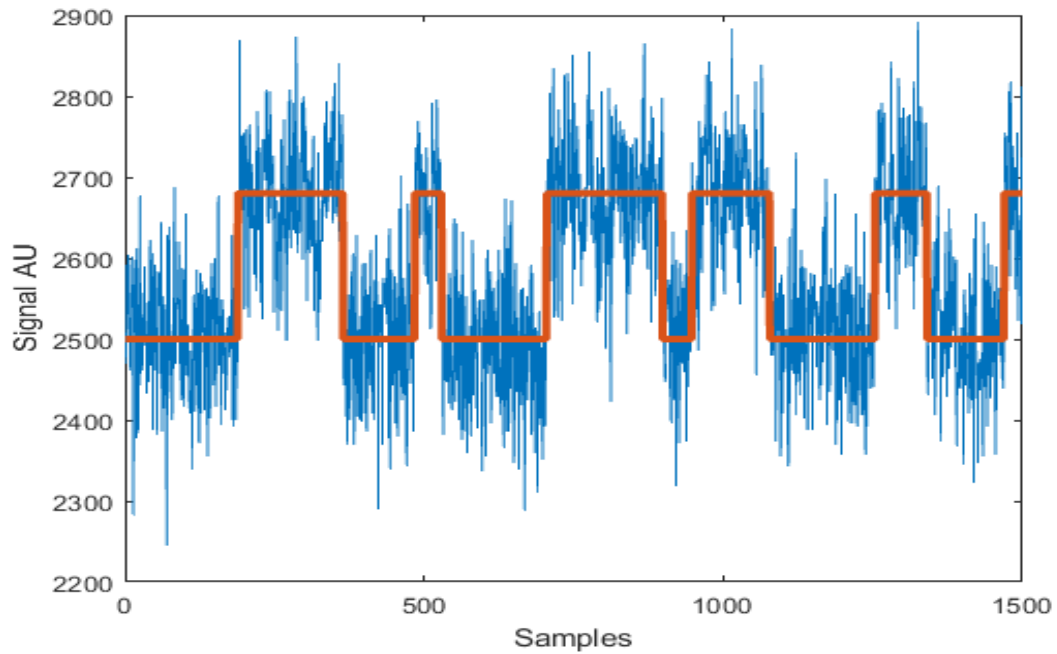
Figure 7: A raw input signal and corresponding reconstruction.

4.2.3. *Machine Learning Reconstruction*

Recent advancements in computing capability have led to an explosion of machine learning (ML) applications in pattern detection and signal denoising. In essence, these machine learning, or deep learning, techniques work by establishing a network of filters or nodes and passing data through them. The data, depending on its characteristics, will add more strongly with some nodes than others. The network 'learns' through trial and error, by means of a backpropagation algorithm [19] which seeks to minimize some loss function. The method employed here [20], uses convolutional filters to extract signal characteristics and reconstruct the signal.

The machine learning method is divided into two parts, classification and denoising. Each part has its own neural network that is trained using simulated data to ensure fidelity between the ground truth and the model's output. Detection of RTS noise is performed by the classification model, which uses three convolutional layers [21] with 32, 64, and 128 filters respectively, shown in figure 8. The resulting feature maps are pooled [22] after each convolution, and a dropout [23] rate of 0.5 was used to prevent the model from overfitting. The last pooled layer is fully connected to the final node, which holds a value between zero and one based on the model's confidence that the signal being classified is RTS (0) or non-RTS (1). Since the model is simply separating an input signal into one of two groups, RTS vs. non-RTS, binary cross-entropy [24] was chosen as the loss function.
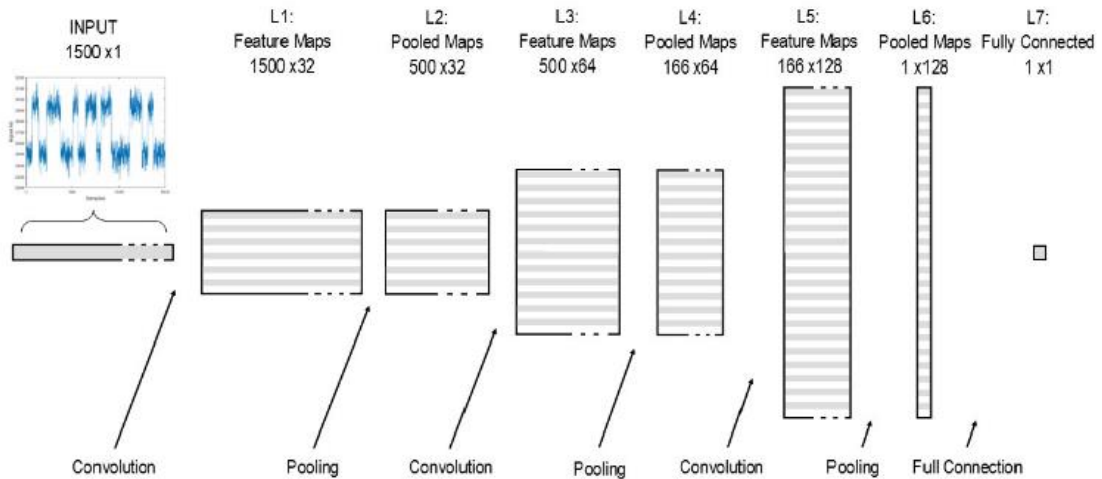
Figure 8: The structure of the classification model.

If the signal is indeed classified as RTS it is passed along to the denoising autoencoder (DAE) where the actual reconstruction occurs. The DAE has similar components to the

classifier, but outputs a vector of the same size as the input, shown in figure 9 [25]. DAEs work by convolving and pooling signals down, extracting prominent features, then expanding them out again. 'Holes' are left in the feature maps during the expansion by means of upsampling. The model 'learns' how to fill in these gaps by training not with a simple yes or no, but comparing its output against a noise-free version of the noisy input signal. A simple linear loss function was chosen for the denoising autoencoder. [26] [27]
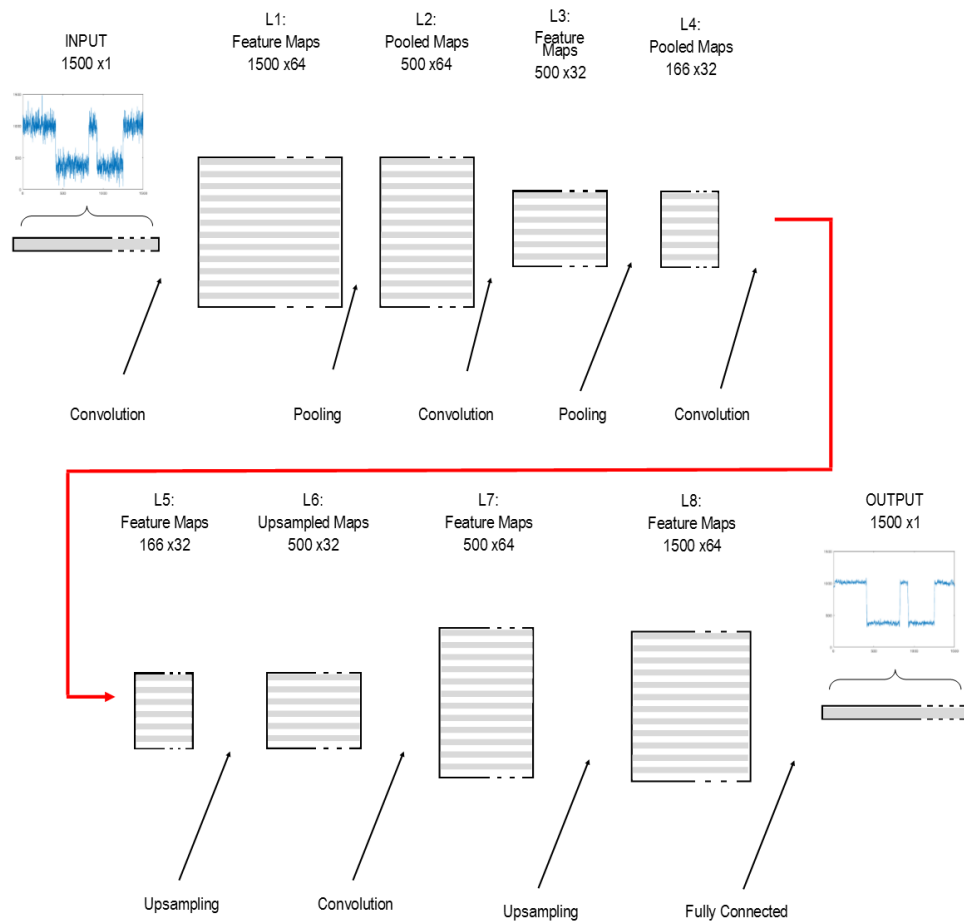
[28]

Figure 9: The structure of the denoising autoencoder.

From here it is evident that the signal to noise has been greatly improved (see figure 10) but the RTS levels still aren't clearly defined. In order to properly reconstruct the signal a histogram is taken from the output of the autoencoder and fit as the sum of two Gaussians [29] (recall that the two noises are assumed uncorrelated). The peaks of that fitted curve are then taken to be the correct levels of a noise free RTS reconstruction, as shown in figure 11.
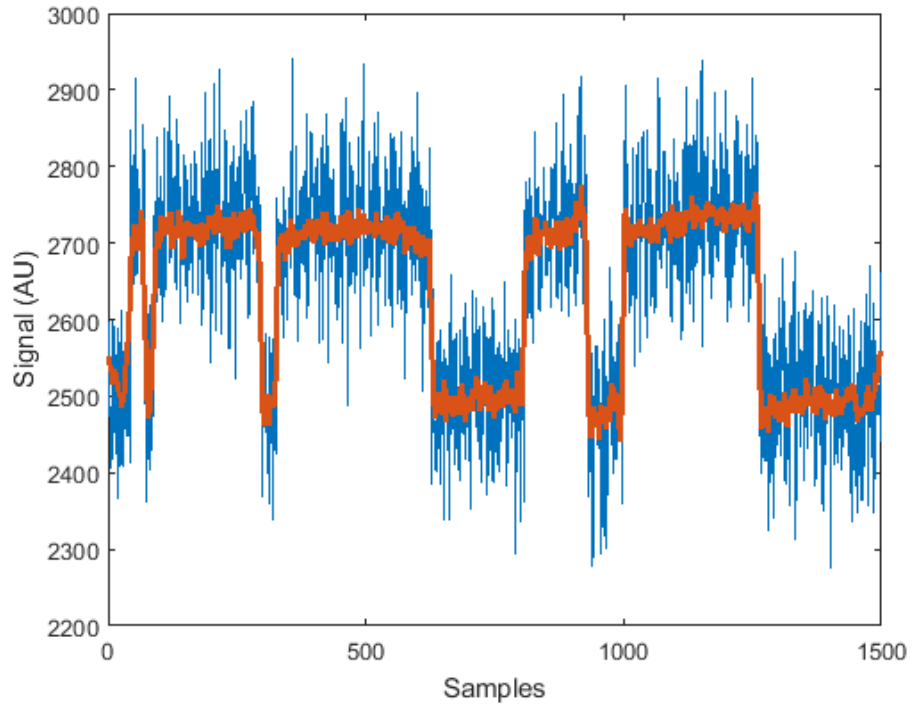
Figure 10: The result of the denoising autoencoder
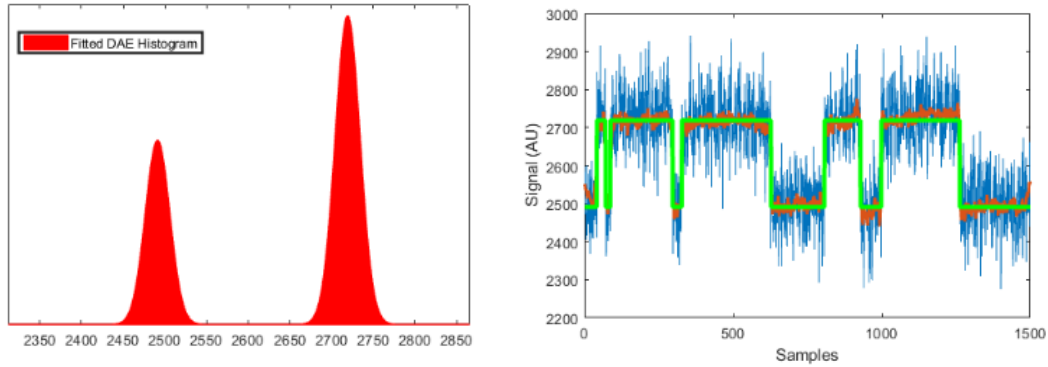
Figure 11: Left: The histogram of values from the autoencoder output fit as the sum of two Gaussians. Right: the final signal reconstruction.

4.3. – Controlled Testing Procedure and Results

4.3.1. Simulated Data Construction and Scoring

In order to offer a fair comparison of each method's efficacy a set of simulated RTS and non-RTS signals were prepared. Each set was comprised of 90,000 signals and each signal is 1,500 samples in length. The shape of the RTS data set can be seen in figure 12. The non-RTS set had a variety of mean signal levels and Gaussian noise distributions and was used exclusively for false positive detection, while the RTS set had a set Gaussian noise contribution, but a variety of RTS amplitudes and state lifetimes.

The state lifetimes span from 1 to 300 samples and were modeled using decaying exponentials such that the transitions remained truly stochastic, but averaged out to a single value for analytical purposes. Every new sample has smaller probability of staying in one state or the other until a flip occurs and the 'clock' starts over. For simplicity state lifetimes

of the 'up' and 'down' states were set equal to one another, which is roughly typical to observed RTS behavior.

The RTS amplitudes span from 1 to 300 arbitrary units (AU) and each has Gaussian noise with a standard deviation of 75 AU. Here a new quantity is defined, RTS signal-to-noise (SNR_{RTS}) as the RTS amplitude divided by the Gaussian noise standard deviation. The dataset then spans an SNR_{RTS} between 1/75 to 6. It was important to include such tiny amplitudes, even to the point of being indiscernible, because there are no defined limits on RTS amplitude. It is very likely that RTS signals are commonly undetected simply because their amplitudes are buried in the Gausssian noise.
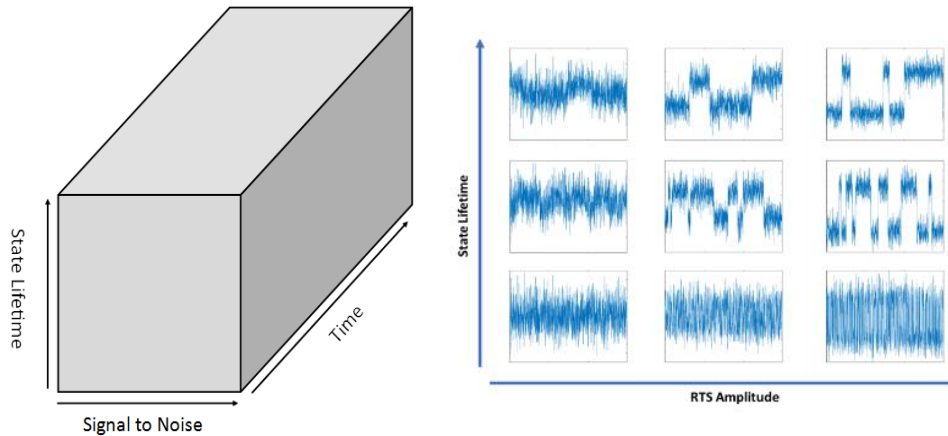
Figure 12: Left: The shape of the RTS data set with labeled axes. Right: An illustration of the distribution of RTS characteristics in the data set.

All RTS signals began as clean curves, then had Gaussian noise added over the top. This choice was made so that a comparison could be made between this clean signal and

the reconstruction. The quality of the reconstruction was scored by the sample correlation coefficient [30], written as:

$$C_{xy} = \frac{\Sigma (x_i - \overline{x})(y_i - \overline{y})}{\sqrt{\Sigma (x_i - \overline{x})^2}\sqrt{\Sigma (y_i - \overline{y})^2}}$$

where C_{xy} is the correlation score, x_i is the value of the ith component of the clean signal, $\overline{x}$ is the mean value of the clean signal, y_i is the value of the ith component of the reconstruction, and $\overline{y}$ is the mean value of the reconstruction. C_{xy} can range between -1 and 1 where a score of 1 is perfectly correlated (perfect reconstruction) and -1 is perfectly anti-correlated. A score of zero means no correlation. Negative scores were predictably rare and always small in magnitude, meaning simply that the reconstruction was poor.

4.3.2. Controlled Testing Results

The convolutional method very faithfully reconstructed RTS signals when it detected them. As seen in figure 13, it performed quite well on signals with $SNR_{RTS} > 2$ and state lifetimes > 50 samples. The high threshold is due to the long filter length (50 samples), but also leads to an impressive zero false detections on the non-RTS data set. The detection rate was 66% on the RTS set, and the mean correlation score for detected signals was $C_{xy} = 0.9474$.
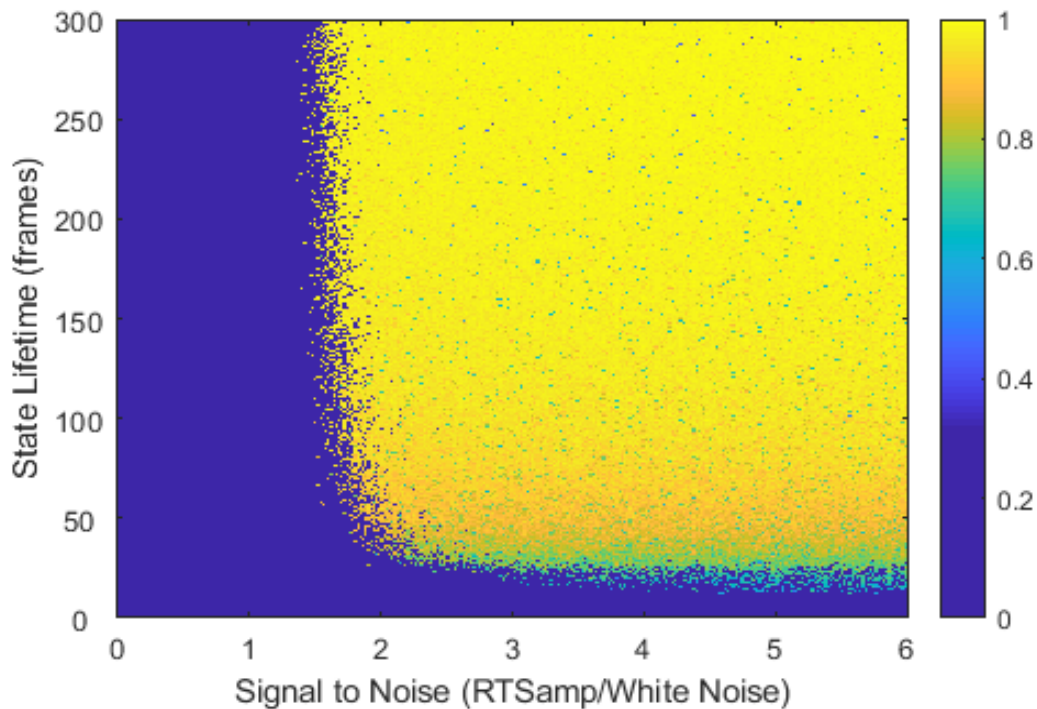
Figure 13: The correlation score map for the convolutional method. A score of 0 indicates that the signals passed undetected.

The wavelet method was able to detect and reconstruct RTS signals, but suffered from inconsistency in performance. As seen in figure 14, it works reliably on RTS signals with $SNR_{RTS} > 2$, and state lifetimes > 50 samples, and is able to detect RTS signals down to around $SNR_{RTS} = 1$ even if the reconstruction suffers. The problem with the wavelet method is the 21.7% false positive detection rate on the non-RTS data set. Perhaps a different threshold would be more appropriate for this kind of signal which would reduce this limitation. Regardless, the wavelet method detected 86.6% of the RTS pixels and scored a mean $C_{xy} = 0.8644$ on the sample correlation coefficient for detected pixels. This

number is pushed down from the number of small amplitude signals that were detected, but proved difficult to reconstruct accurately.
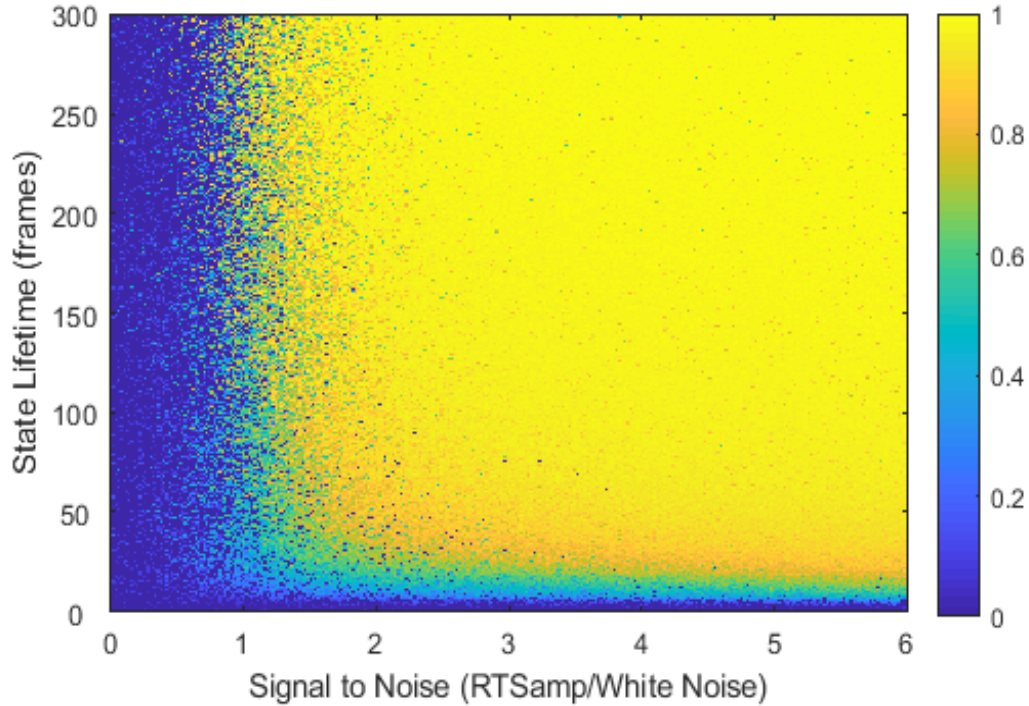
Figure 14: The correlation score map for the wavelet method. A score of 0 indicates that the signals passed undetected.

The machine learning method out-performed the other two. It produced the consistent reconstruction seen by the convolutional method, while detecting RTS signals with much smaller amplitudes and faster state lifetimes. As seen in figure 15, it works reliably in signals with $SNR_{RTS} > 1$ and state lifetimes > 25 samples. Like the convolutional method, the machine learning method reported zero false positive detections on the non-RTS data set. It boasted a 83.5% detection rate on the RTS set, and a mean correlation score of $C_{xy} =$

0.9780. The quality of reconstruction from the machine learning method is further illustrated in table 1, where the distribution of correlation scores show that the great majority of reconstructions are nearly perfect.
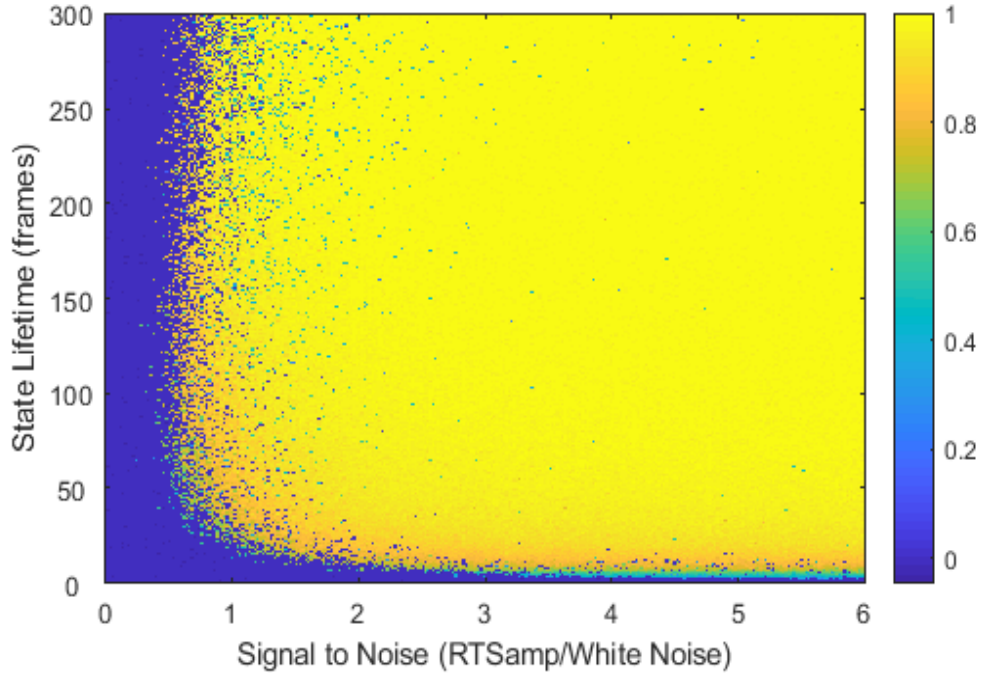
Figure 15: The correlation score map for the machine learning method. A score of 0 indicates that the signals passed undetected.

Correlation Range	Convolution Counts	Wavelet Counts	M.L. Counts
$0 < C_{xy} < 0.4$	6	5,342	68
$0.4 \leq C_{xy} < 0.6$	162	3,746	257
$0.6 \leq C_{xy} < 0.7$	674	2,772	251
$0.7 \leq C_{xy} < 0.8$	2,404	3,755	730
$0.8 \leq C_{xy} < 0.9$	5,271	6,460	2,523
$0.9 \leq C_{xy} < 0.99$	42,660	47,600	21,613
$C_{xy} \geq 0.99$	8,143	8,274	49,659

Table 1: The correlation score breakdown for the three methods

91

A curious feature of the machine learning map is that it seems to show more difficulty reconstructing signals with low amplitudes and long lifetimes than those with low amplitudes and short lifetimes. This may indicate that when the amplitude is small, the models benefit from having more transitions to detect and reconstruct. Regardless, it is the clear winner of the three, and yet another example of machine learning techniques outperforming classical methods.

4.4. Observations From Collected Data

4.4.1. Data Collection Conditions

RTS and non-RTS signals were collected in the form of stacked pixel outputs from a charge-coupled device (CCD) image sensor. 1,500 frames were collected under dark conditions at $305K \pm 0.1$. The integration time was ten seconds and the readout time was six seconds for a frame rate of $\sim 0.06/s$. The sensor itself is a SITe SI-033AF frontside illuminated CCD with 4 amplifier outputs and a $1024x1024$ pixel array [31]. This particular sensor hasn't undergone irradiation, but still has a significant number of RTS pixels ($\sim 1\%$) likely due to long term exposure to cosmic rays. For this experiment a region of interest ($400x400$ pixels) was chosen. This region shares the same amplifier, and is located centrally inside one of the sensor's four quadrants.

4.4.2. Strengths and Weaknesses of Each Method

Detection of RTS signals by each of the three methods fulfilled the expectations provided laid out by the controlled experiment. The following section provides a broad description of each method's performance on the collected data, and takes a closer look at how each method performed on a variety of RTS signals with different attributes.

92

1) The Convolutional Method

The convolutional method detected 598 RTS signals out of a possible 160,000. The only false detections observed are from cosmic ray interactions, shown in figure 17, according to visual inspection. How did W and Ml perform on this pixel?
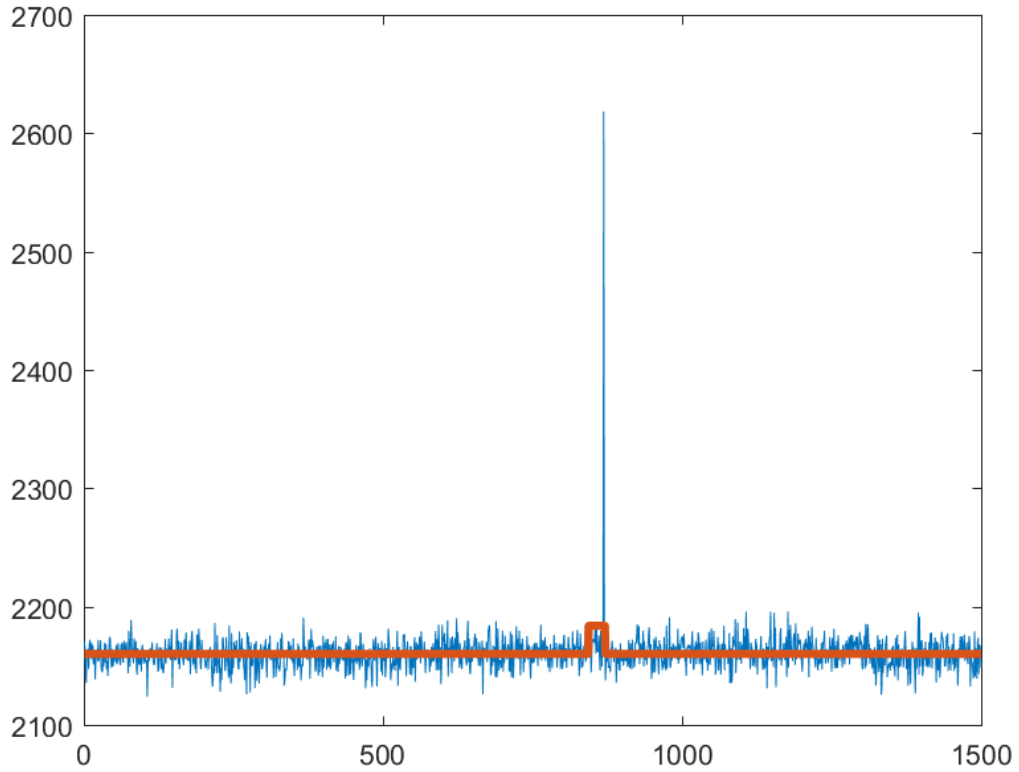
Figure 16: A false positive detection and reconstruction of signal showing a cosmic ray interaction.

Well behaved 2-level RTS signals, that is those with larger amplitudes and longer state lifetimes, were reconstructed quite well (figure 18). In these cases RTS parameters can be reliably extracted.
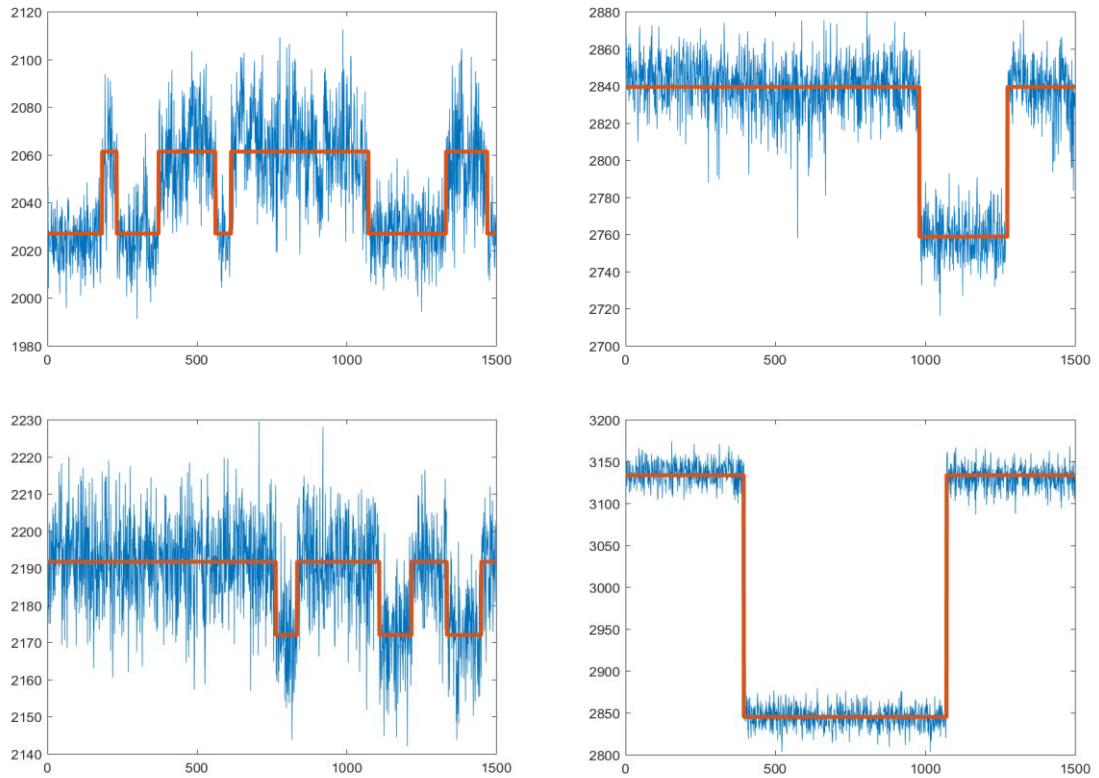
Figure 17: Four quality reconstructions provided by the convolutional method. All units are arbitrary.

The only cases where the convolutional method struggled were highly erratic pixels

(figure 19), and multi-level RTS signals with shorter state lifetimes (figure 20).
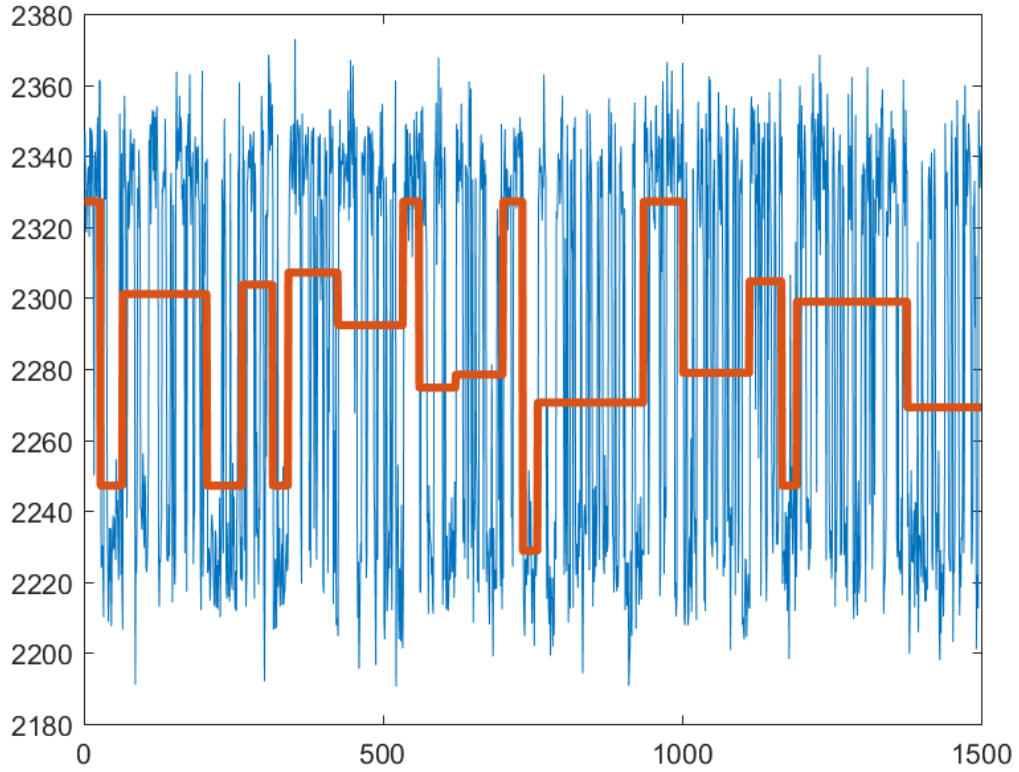
Figure 18: A highly erratic 2-level RTS signal.
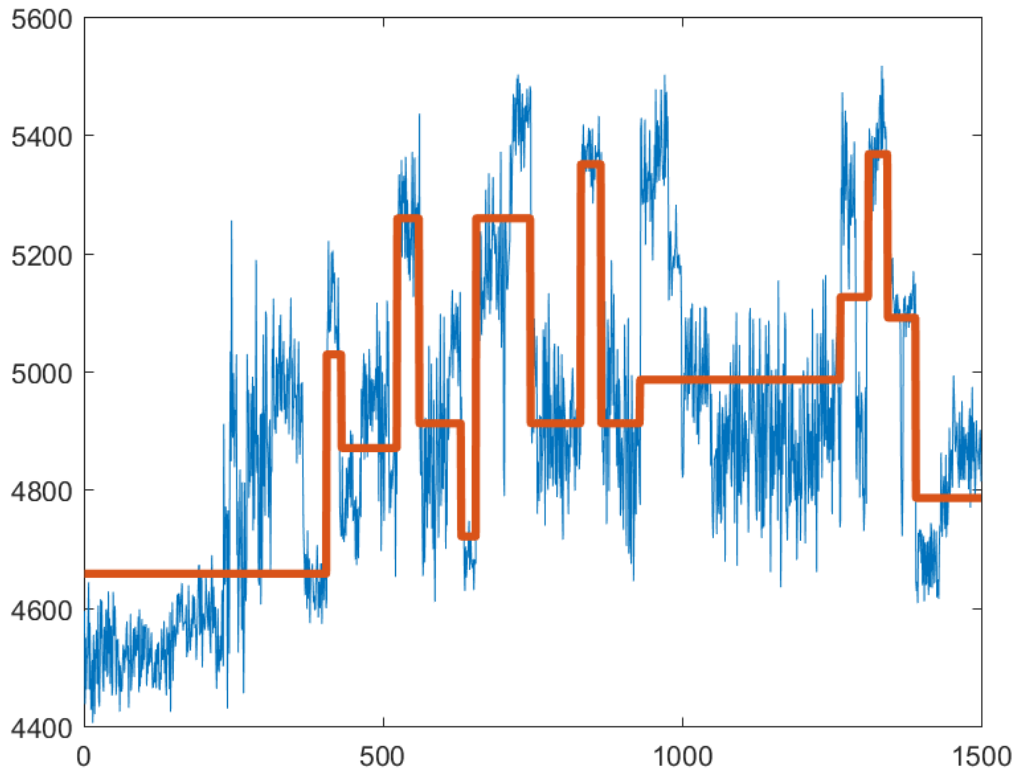
Figure 19: A poorly reconstructed multi-level RTS signal.

It should be noted that while both the convolutional and wavelet methods detected and reconstructed multi-level RTS signals, seen in figure 21, the ML method, because of the double Gaussian peak fitting, cannot. Multi-level RTS signals accounted for $< 1\%$ of all RTS detections. Generally the convolutional method provided more accurate reconstructions of multi-level RTS signals than the wavelet method.
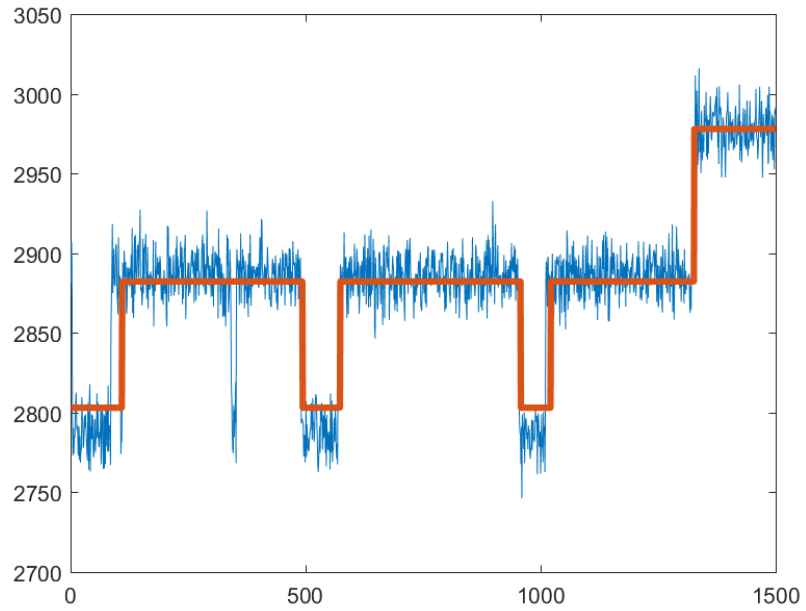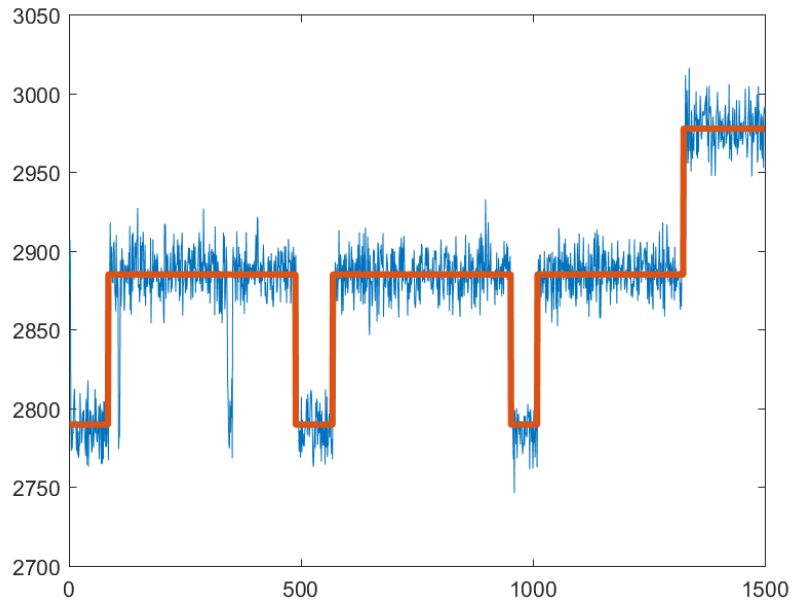
Figure 20: Reconstruction of the same 3-level RTS signal by the convolutional method (top), and wavelet method (bottom). The convolutional method is a truer representation of the noisy signal, but both miss the brief transition around frame 400.

2) The Wavelet Method

The wavelet method detected 6,678 RTS signals, roughly 10 times the number detected by the other two, many of which were false positives (roughly 55% by visual inspection). Just as with the simulated data, the wavelet method displayed an ability to detect and reconstruct RTS signals with much smaller amplitudes (figure 22) than the convolution or ML methods, of course at the cost of the many false positives (figure 23). When the signals were relatively well behaved, the wavelet method was able to reconstruct them with similar accuracy as the convolutional method.
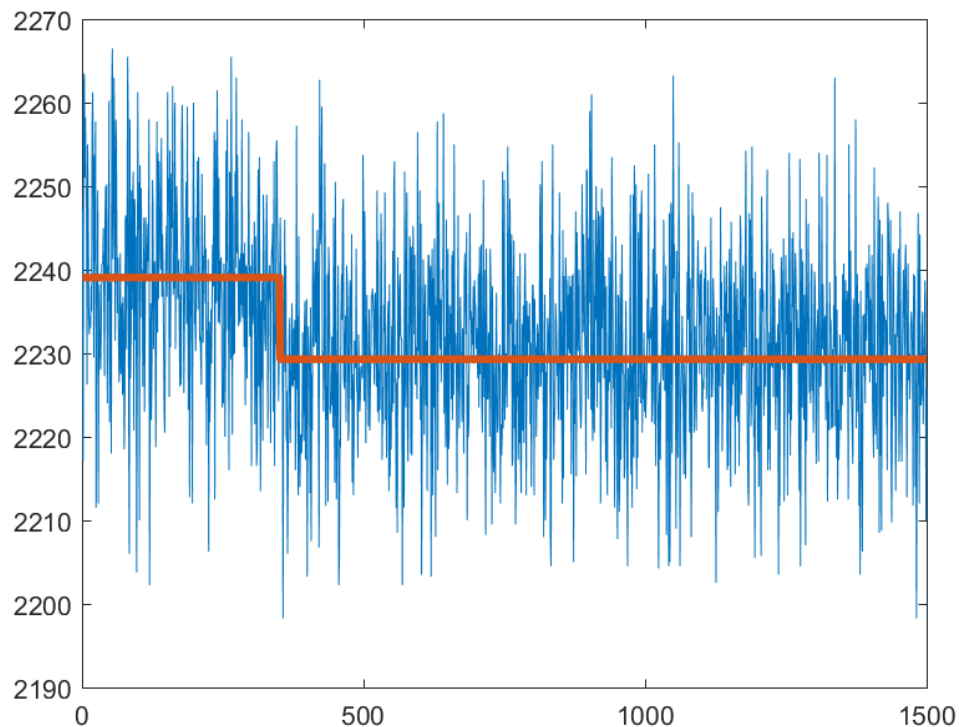
Figure 21: A small amplitude ($\sim 0.8\ SNR_{RTS}$) reconstruction provided by the wavelet method. Neither the convolutional nor ML method detected this signal.
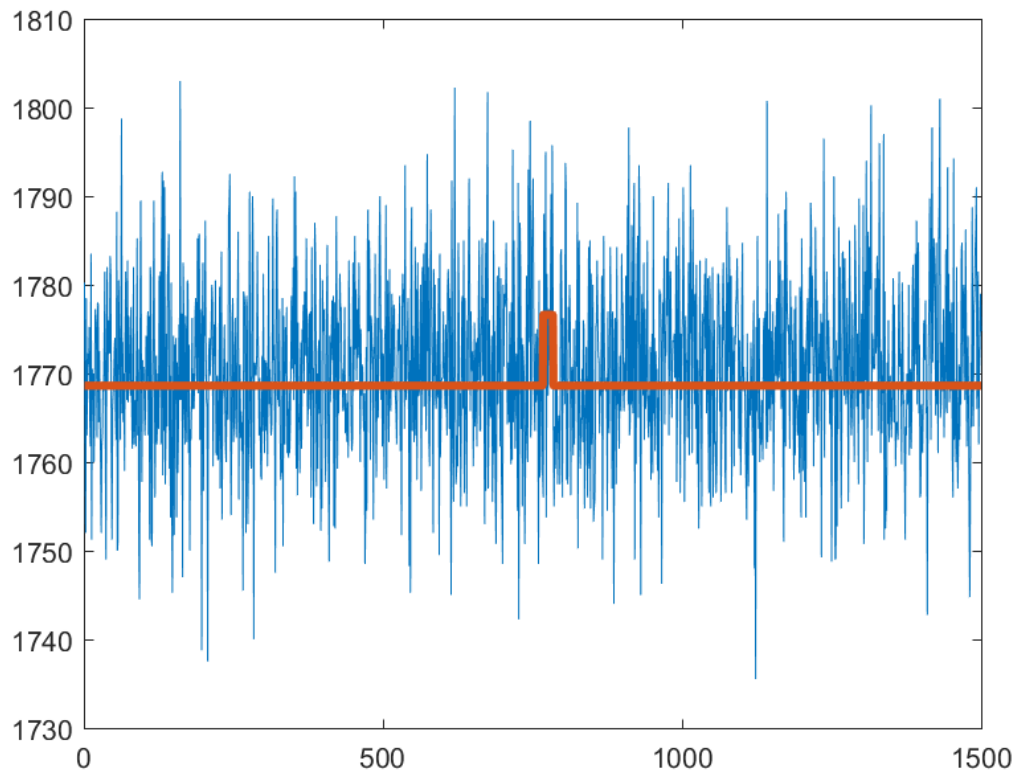
Figure 22: A false detection reconstruction provided by the wavelet method.

3) The Machine Learning Method

The ML method detected more RTS signals than the convolutional method, but fewer than the wavelet method. Just as with the convolutional method, it reported very few false detections, but was occasionally fooled by cosmic ray interactions. The ML method detected 697 RTS signals. While it fails to reconstruct multi-level RTS signals, the ML excels at two-state signals with small amplitudes (figure 24) and very short state lifetimes (figure 24).
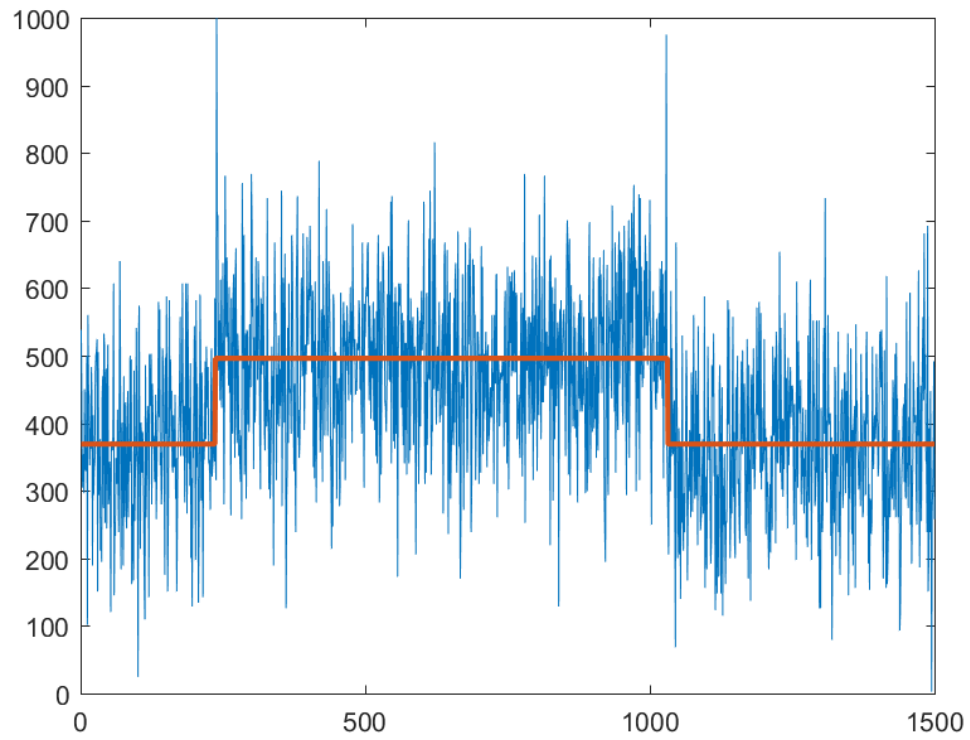
Figure 23: A small amplitude signal successfully detected and reconstructed by the ML method. The wavelet method produced a similar reconstruction, but the convolutional method failed to detect it.
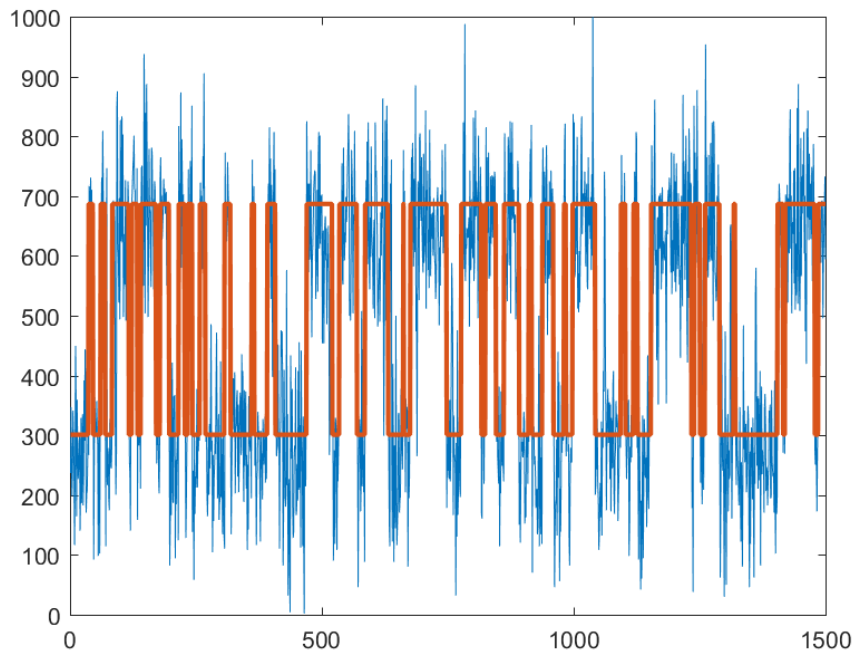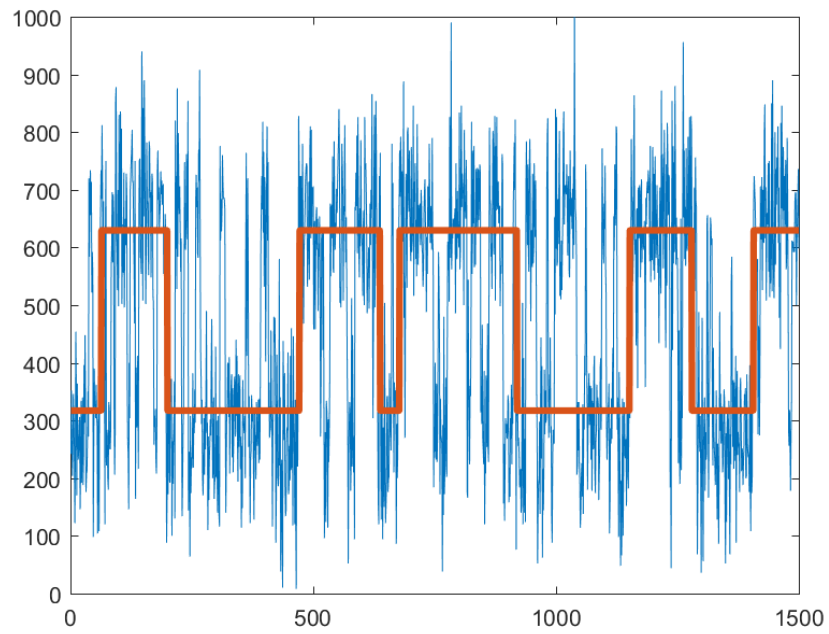
Figure 24: A reconstruction of a short lifetime signal by the wavelet method (top), and
ML method (bottom). This signal went undetected by the convolutional method.

4.5. – Conclusion

Three methods for the detection and reconstruction of bistable RTS signals are presented and compared. The three methods are built on three distinct mathematical toolsets: convolutional filtering, the wavelet transform, and machine learning. A controlled experiment was carried out to test each method's ability to accurately reconstruct a clean RTS signal from a corresponding noisy signal. It was found that while the wavelet method detected the most RTS signals, 86.6% of the test set, the ML method had the highest performance of the three, by detecting 83.5% of the RTS signals, returning zero false positives and a mean sample correlation coefficient score of $C_{xy} = 0.9780$. Furthermore, the three methods were used on a set of data collected by taking dark frames with a CCD image sensor. The results of this experiment, mostly qualitative, roughly mirrored those from the controlled experiment. Again, for bistable RTS signals, the ML method outperformed the other two by being more responsive to fast state transitions and small amplitudes, leading to accurate noise-free reconstructions of the detected RTS signals.

4.6. - References

[1] D. Zhang, J. Ryu and T. Nishimura, "A Novel Modeling and Evaluating for RTS Noise on CMOS Image Sensor in Motion Picture," *IEICE Transactions on Information and Systems,* vol. E93, no. 2, pp. 350-358, 2010.

[2] C. Virmontois, V. Goiffon, P. Magnan, O. Saint Pé, S. Girard, S. Petit, G. Rolland and A. Bardoux, "Total Ionizing Dose Versus Displacement Damage Dose Induced Dark Current Random Telegraph Signals in CMOS Image Sensors," *IEEE Trans. on Nucl. Sci.,* vol. 58, no. 6, pp. 3085-3094, 2011.

[3] V. Goiffon, P. Magnan, P. Martin-Gontier and C. Virmontois, "New source of random telegraph signal in CMOS image sensors," in *International Image Sensor Workshop*, Hokkaido, Japan, 2011.

[4] M. Uren, D. Day and M. Kirton, "1/f and random telegraph noise in silicon metal-oxide-semiconductor field-effect transistors," *Applied Physics Letters,* vol. 47, p. 1195, 1985.

[5] W. Shockley and W. Read, "Statistics of the Recombination of Holes and Electrons," *Phys. Rev,* vol. 87, no. 835, 1952.

[6] R. Hall, "Electron-Hole Recombination in Germanium," *Phys. Rev. ,* vol. 87, no. 387, 1952.

[7] V. Goiffon, "Radiation Effects on CMOS Active Pixel Image Sensors," in *Ionizing Radiation Effects in Electronics: From Memories to Imagers*, Boca Raton, CRC Press, 2015, pp. 295-332.

[8] J. Bogaerts, B. Dierickx and R. Mertens, "Random telegraph signals in a radiation-hardened CMOS active pixel sensor," *IEEE Trans. on Nucl. Sci.,* vol. 49, no. 1, pp. 249-257, 2002.

[9] V. Goiffon, G. Hopkinson, P. Magnan, F. Bernard, G. Rolland and O. Saint Pé, "Multilevel RTS in Proton Irradiated CMOS Image Sensors Manufactured in a Deep Submicron Technology," *IEEE Trans. Nucl. Sci,* vol. 56, pp. 2132-2141, 2009.

[10] G. Chen, W. Xie and Y. Zhao, "Wavelet-based denoising: A brief review," in *2013 Fourth International Conference on Intelligent Control and Information Processing (ICICIP)*, Beijing, 2013.

[11] Ç. P. Dautov and M. Özerdem, "Wavelet transform and signal denoising using Wavelet method," in *2018 26th Signal Processing and Communications Applications Conference* , Izmir, 2018.

[12] P. Addison, J. Walker and R. Guido, "Time--frequency analysis of biosignals," *IEEE Engineering in Medicine and Biology Magazine,* vol. 28, no. 5, pp. 14-29, 2009.

[13] Y.-F. Li, "Image denoising based on undecimated discrete wavelet transform," in *2007 International Conference on Wavelet Analysis and Pattern Recognition*, Beijing, 2007.

[14] A. Ouahabi, "A review of wavelet denoising in medical imaging," in *2013 8th International Workshop on Systems, Signal Processing and their Applications (WoSSPA)*, Algiers, 2013.

[15] B. Hendrickson, R. Widenhorn, M. Blouke and E. Bodegom, "Wavelet Analysis of RTS Noise in CMOS Image Sensors," *IEEE Trans. on Nucl. Sci.,* Submitted for Publication.

[16] J. Walker, A Primer on Wavelets and their Scientific Applications. 2nd ed., Boca Raton: Chapman & Hall/CRC, 2008.

[17] G. Nason, "Wavelets and Statistics. Lecture Notes in Statistics," in *Choice of the Threshold Parameter in Wavelet Function Estimation*, New York, Springer, 1995.

[18] J. Groß, Linear Regression, Berlin: Springer, 2003.

[19] Y. Lecun, L. Bottou, Y. Bengio and P. Haffner, "Gadient-based learning applied to document recognition," *Proceeding of the IEEE,* vol. 86, pp. 2278-2324, 1998.

[20] B. Hendrickson, R. Widenhorn, P. DeStefano and E. Bodegom, "Detection and Reconstruction of Noisy Bistable Stochastic Time Domain Signals with Machine Learning," *Signal Process.,* Submitted For Publication.

[21] J. Li, Y. Si, L. Lang, L. Liu and T. Xu, "A Spatial Pyramid Pooling-Based Deep Convolutional Neural Network for the Classification of Electrocardiogram Beats," *Appl. Sciences,* vol. 8, p. 1590, 2018.

[22] D. Ciresan, U. Meier, J. Masci, L. Gambardella and J. Schmidhuber, "Flexible, High Performance Convolutional Neural Networks for Image Classification," in *International Joint Conference on Artificial Intelligence* , Barcelona, 2011.

[23] G. Hinton, N. Srivastava, A. Krizhevsky, I. Sutskever and R. Salakhutdinov, "Improving neural networks by preventing co-adaptation of feature detectors," *ArXiv,* 2012.

[24] P. Sadowski, "Notes on backpropagation," 2016. [Online]. Available: https://www.ics.uci.edu/.

[25] P. Vincent, H. Larachelle, I. Lajoie, Y. Bengio and P. Manzagol, "Stacked denoising autoencoders: Learning useful representation in a deep network with a local denoising criterion," in *Proceedings of the 27th International Conference on Maching Learning*, 2010.

[26] L. Gondara, "Medical Image Denoising Using Convolutional Denoising Autoencoders," in *IEEE 16th International Conference on data Mining Workshops (ICDMW)*, Barcelona, 2016.

[27] G. Hinton, L. Deng, D. Yu, G. Dahl, A. Mohamed, N. Jaitly, A. Senior, V. Vanhoucke, P. Nguyen, T. Sainath and B. Kingsbury, "Deep Neural Networks for

Acoustic Modeling in Speech Recognition: The Shared Views of Four Research Groups," *IEEE Signal Process. Mag.,* vol. 29, pp. 82-97, 2012.

[28] X. Ye, L. Wang, H. Xing and L. Huang, "Denoising hybrid noises in image with stacked autoencoder," in *IEEE International Conference on Information and Automation*, Lijiang, 2015.

[29] T. O'Haver, Pragmatic Introduction to Signal Processing 2019: Applications in scientific measurement, Kindle Direct Publishing, 2019.

[30] N. Bershad and A. Rockmore, "On estimating signal-to-noise ratio using the sample correlation coefficient," *IEEE Trans. on Info. Theory,* vol. 20, pp. 112-113, 1974.

[31] SITe, "SI03xA 24 µm Charge-Coupled Device Family," 2003. [Online]. Available: http://www.not.iac.es/instruments/detectors/CCD1/S103xA_family.pdf.

CHAPTER FIVE – DISCUSSION AND CONCLUSION

Bistable phenomena have been observed in a variety of scientific domains. Measurements of ion transport through biological membranes, single molecule chemical reactions, and electron spin resonance all produce signals with the non-linear transitions outlined in the previous chapters. RTS noise, a kind of bistable process that affects semiconductor devices, has caused increasing concern for image sensor manufacturers in recent years due to the successful mitigation of previously dominant noise sources. The successful detection and reconstruction of these random transitions in video signals can lead to the removal of this noise source, which appears similar to television 'snow'.

From a scientific perspective RTS noise is a fascinating subject of study. Collecting temporal data from an image sensor allows a researcher to study bistable semiconductor defects from a statistical perspective; a twelve-megapixel sensor contains twelve million roughly identical discrete devices. Though the type (or types) of defects responsible for generating RTS transitions has yet to be confirmed, this statistical approach has yielded interesting results such as the unbounded nature of state lifetimes.

The production rate of RTS defects was one of the more surprising results from this course of study. It was shown that high energy photons created RTS defects at a nearly quadratic rate indicating their formation is a two-stage process. The intermediary stage was never detected and should be pursued in the future.

In order to carry out this study, a signal reconstruction technique was developed built on the wavelet transform. Wavelet denoising involves breaking the signal into two daughter signals, the trends and details vectors, then thresholding the members of the

details vector. Thus, when the reverse transform is performed the Gaussian noise is greatly reduced allowing for simple noise-free reconstruction.

The tools for detecting and reconstructing RTS transitions are imperfect, the wavelet technique included, but recent advancements in computational techniques (introduced in chapter 3) were shown to provide an improvement over the current state-of-the-art. A new technique for RTS analysis built on convolutional networks was developed to classify RTS signals from non-RTS signals and then reduce the Gaussian noise on signals that passed detection. Both the detection and noise suppression was carried out using so called supervised learning techniques.

The classification model was built using a deep learning architecture similar to networks used for image classification. The model is fed a series of signals and produces an identification score for each signal based on its confidence. That score is then checked against the label provided so that an error can be calculated. That error function is then used to tweak the parameters in the network to improve its accuracy over time.

The noise suppression model is called a denoising autoencoder, like the classification model, it is fed a series of signals and tweaks the network parameters based on an error function. Here though, rather than output a confidence score, the autoencoder produces a signal similar to the input, but with less Gaussian noise. This is achieved in the network by squeezing the input signal, then stretching it back out with regularly spaced gaps. The model attempts to fill in the gaps. The quality of the noise suppression is measured by comparing the output of the autoencoder against a noiseless version of the input signal.

It was necessary for both the classifier and autoencoder to have full control over the training data. As such, data collected from an image sensor would be unsuitable. It is impossible for even a human to always know with perfect certainty whether or not a signal has RTS transitions, and if so, how to perfectly reconstruct it without any Gaussian noise contribution. Therefore, sets of contrived signals were created. RTS and non-RTS signals were produced and Gaussian noise was added over the top. These sets of signals were created such that they represented a wide variety of state lifetime and amplitude characteristics. The set of non-RTS signals was maintained to test for false positive RTS detection.

After training the classification and denoising autoencoder models, new RTS and non-RTS data sets were created in order to compare the detection and reconstruction abilities of three techniques useful in RTS analysis. This comparison is discussed in chapter 4. The three techniques included the method based on convolutional filtering, the method based on the wavelet transform, and finally the method based on deep learning neural networks. It was shown that the machine learning method detected more RTS signals than the convolutional method, without any false positive detections that plagued the wavelet method. Additionally, signals detected by the machine learning method were commonly reconstructed with a very high degree is similarity. Nearly two thirds of the detected RTS signals were reconstructed with a sample correlation coefficient of .99 or higher when compared against the clean versions of the input.

In addition to this controlled experiment, the three methods were also applied to data collected from an image sensor. Since this experiment was not controlled like the one

before it the results were more qualitative than quantitative. The wavelet method detected the most RTS signals from this dataset, though as with the controlled experiment, many of them were likely false positives. Again, the convolutional method and machine learning method proved to be far-more discriminatory, though the latter did detect 99 more RTS signals than the former, an increase of roughly 16%. The quality of the reconstruction was based on human judgement, since no noise-free version of the signals exists. The results seem to reflect the results of the controlled experiment, with the machine learning method outperforming the other two, particularly on signals with very short state lifetimes.

The documents presented as chapters 2, 3, and 4 of this manuscript represent a body of work that explores a two state phenomenon that exhibits bistable behavior. RTS noise is a fascinating topic because of its metastability, and is an increasingly important one as a limiting noise source in image sensors. In the course of searching for a more effective means of analyzing RTS noise it was discovered that the underlying dynamic of bistability is found in a wide variety of scientific fields. Thus, the analytical tools presented here may be of interest to a large academic audience.

Deep learning has opened the door to many new applications. One reason these techniques have been so successful is they are built using nonlinear functions. It's no surprise that these nonlinear techniques would perform so well on nonlinear signals. Bistability is only one kind of nonlinearity. The work presented here shows that these techniques are capable of out performing more traditional approaches.